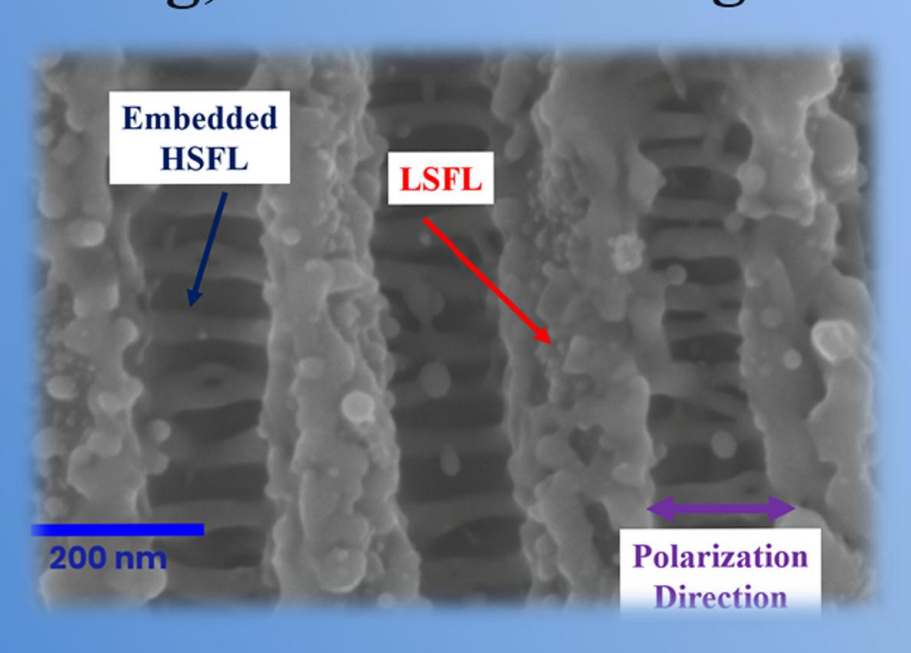
# Ph.D. Thesis

Ultrafast laser surface processing and its applications in the fabrication of dual-scaled grating structures, perfect absorbing, and non-wetting surfaces



**MD ABU TAHER** 



School of Physics University of Hyderabad Hyderabad-500046, India.

**December 2021** 

# Ultrafast laser surface processing and its applications in the fabrication of dual-scaled grating structures, perfect absorbing, and non-wetting surfaces

A thesis submitted for the award of the degree of Doctor of Philosophy in Physics

by

**Md Abu Taher** 

Registration ID: 15PHPH18
Under the guidance of

Dr. N. Sri Ram Gopal



School of Physics University of Hyderabad Hyderabad-500046, India.

December 2021

# To My parents Md Samsul Hoque and Rijia Bibi

**Declaration** 

I, Md Abu Taher, hereby declare that this Ph.D. thesis entitled "Ultrafast laser surface

processing and its applications in the fabrication of dual-scaled grating structures,

perfect absorbing, and non-wetting surfaces" has been carried out by me under the

supervision of Dr. N Sri Ram Gopal, School of Physics, University of Hyderabad, as per

the Ph.D. ordinances of the University. I declare to the best of my knowledge that this is

a bonafide work, and no part of this thesis has been submitted for the award of a research

degree to any other institution.

A report on plagiarism statistics from the University Librarian is enclosed.

Md Abu Taher

Registration ID: 15PHPH18

Date: 15/12/2021

Place: Hyderabad



### Certificate

This is to certify that the thesis entitled "Ultrafast laser surface processing and its applications in the fabrication of dual-scaled grating structures, perfect absorbing, and non-wetting surfaces" submitted by Md Abu Taher bearing Registration ID: 15PHPH18 in fulfilment of the requirements for the award of Doctor of Philosophy in Physics is a bonafide work carried out by him under my supervision and guidance. This thesis is free from plagiarism and has not been submitted previously in part or in full to this or any other university or institution for the award of any degree or diploma. Further, the student has the following publications before the submission of the thesis for adjudication.

- 1. "Controlled periodicities of ladder-like surface structures via femtosecond laser irradiation of wavelengths from 400 nm to 2200 nm", Md Abu Taher, Nitin Choudhary, Thirunaukkarasu K, Vinod K Rajput, and Sri Ram Gopal Naraharisetty, Surfaces and Interfaces, 28(2022) 101622. (Chapter 3).
- **2.** "The validity of Triple Contact Line theory from hydrophilic to superhydrophobic surfaces," Md Abu Taher, Vinod Kumar Rajput, Navanith Krishnan P K, and Sri Ram Gopal Naraharisetty. **J. Phys. D: Appl. Phys.** 55(2022) 055305. (Chapter 6).
- **3.** "Broadband absorption of nanostructured stainless steel surfaces fabricated by nanosecond laser irradiation", Md Abu Taher, Sajin Ponnan, Hitheswar Prasad, Desai Narayana Rao, and Sri Ram G Naraharisetty, **Nanotechnology**, 31(2020) 175301. (Chapter 5).
- **4.** "Ellipsoidal droplet formation on anisotropic superhydrophobic copper surface", Md Abu Taher, Hitheswar Prasad, PK Navanith Krishnan, Narayana Rao Desai, and Sri Ram

Gopal G Naraharisetty, **Surface Topography: Metrology and Properties**, 7 (2019) 0355001. (Chapter 6).

- 5. "Wavelength dependent cubic nanoparticles formation on copper surfaces by femtosecond laser irradiation", Md Abu Taher, D Narayana Rao, and Sri Ram Gopal Naraharisetty, Asian Journal of Physics (under review). (Chapter 4).
- 6. "Mechanically and thermally stable thin sheets of broadband antireflection surfaces fabricated by femtosecond lasers", Thirunaukkarasu K, Md Abu Taher, Nitin Choudhary, Vinod K Rajput, Chavan Akash Naik, Jai Prakash Gautam, and Sri Ram Gopal Naraharisetty. Optics and Laser Technology Under review (Manuscript Id: JOLT-D-21-02479)
- 7. "Material dependent upper limit of spatial periodicity of laser induced periodic surface structures", Md Abu Taher, Sri Ram G Naraharisetty. (Manuscript under preparation).

Further, the student has passed the following courses towards the fulfilment of coursework required for Ph.D.

S. No	Course Code	Name of the course	Credits	Pass/Fail
1	PY801	Advanced Quantum Mechanics	4	Pass
2	PY803	Advanced Statistical Mechanics	4	Pass
3	PY804	Advanced Electromagnetic Theory	4	Pass
4	PY821	Research Methodology	4	Pass

Dr. N Sri Ram Gopal

Thesis supervisor

School of Physics Dr. N. SRI RAM GOPAL

University of Hyderabadistant Professor,

School of Physics, University of Hyderabad Hyderabad-500 046.

Soulongapl

Date: 15/12/2021

Place: Hyderabad

Prof. K. C. James Raju

Dean

School of Physics

University of Hyderabad.

DEAN

School of Physics University of Hyderabad HYDERABAD - 500 046

#### Acknowledgments

Alhamdulillah, I praise and thank Allah SWT for His greatness and giving me the strength and courage to complete my thesis. First and foremost, I want to express my gratitude and most profound respect to **Dr. N Sri Ram Gopal Sir**, who has guided me throughout thesis with his patience and knowledge. Prof. D Narayana Rao Sir, please accept my heartfelt gratitude for the stimulating and informative talk during my research.

I want to thank my doctoral committee members, Prof. Ananthalakshmi Ma'am, Prof. Nirmal K Viswanathan Sir, for their valuable recommendations and assistance during doctoral committee meetings and on several occasions. I want to express my gratitude to Ashoka Sir and Prof. Sunil Sing Sir for their numerous contributions.

I want to acknowledge the present Dean, Prof. K. C. James Raju Sir, for his support and encouragement. My sincere gratitude to former Deans Subhash Chaturvedi Sir, Prof. R. Singh Sir, Prof. Bindu A. Bamba Ma'am, Prof. V. Seshu Bai Ma'am, Prof. Ashok Chatterjee Sir.

I want to express my most profound respect to professors during my M.Sc courses especially, Hari Kumar Sir, Subhasish Dutta Gupta Sir, Nageswara Rao Sir, Soma Sanyal Ma'am, Syamal Sir, Srinath Sir.

I want to thank everyone in the office, especially Sudarshanam Sir, Narasimha Rao Sir, Deepika Ma'am, Abraham Sir, and others, for their help and guidance.

The financial support from UGC-MANF is greatly appreciated.

Professors at Aligarh Muslim University have always taught me the fundamentals of science and shown me how to be a conscientious student. I am thankful for that. I am grateful to the Al-Ameen Mission family for assisting me with my studies in the 12th grade. All of my school teachers, particularly Mainul Hoque Sir, S. N. Pal Sir, Abdul Bari Sir, and Harun Al-Rashid Sir, have always encouraged and guided me in shaping my destiny.

Dr. L Jyoti, Dr. Sai Kiran, Dr. Kuladeep, Dr. Mudasir Dar, Dr. E Ramya, Dr. Nabil, and Dr. Shihab N K deserve special gratitude for their encouragement and support. Vinod, Sajin, Navanith, Thirunaukkarusu, Hiteswar, Nitin, Prasenjit, and Shilpa, my labmates, deserve my heartfelt gratitude for maintaining a healthy and cheerful atmosphere in the lab.

Rashmi Ranjan Suna, Sujai, Avisek, Zahid, Manasa, Leela, Nilanjan, Bappaditya, Naresh, Vinod, Muhammed Rasi, Rajesh, Hemant, Praneetha, Subrata Mondal, John., Rizwan,

Hafizur, Alim, Saddam, and all my juniors from the school of physics and other departments supported me accomplish my journey.

My parents have given me opportunities and experiences that have shaped who I am now, and I shall be eternally thankful to them. My wife, Sirin Sultana, deserves credit for her patience and support during my Ph.D. studies. My son, Mohammed Afif, offered me much joy and comfort whenever I needed it the most. I relieved my mental exhaustion after seeing your adorable and smiling face. Her encouragement means a lot to me, and I appreciate her belief in me. I also want to express my gratitude to my father and mother-in-law. I am genuinely thankful to my brothers, sisters, and other family members, for their love and care.

# **Contents**

Declaration	iii	
Certificate	v-vii	
Acknowledgments	ix-xi	
Chapter 1: Introduction		
1.1. Introduction	2-5	
1.2. Dual-scaled gratings fabrication	5	
1.3. Cubic-shaped copper nanoparticles processing	5-6	
1.4. Broadband superblack surface	6	
1.5. Anisotropic superhydrophobicity	6-7	
1.6. Organization of the thesis	7-9	
References	9-18	
Chapter 2: Experimental procedure and methodology	19-28	
2.1. Laser micromachining setup	20	
2.2. Femtosecond Ti: Sapphire laser	20-21	
2.3. Optical parametric amplifier	21-23	
2.4. Femtosecond fiber laser	23-24	
2.5. Nanosecond laser system	24	
2.6. Field emission-scanning electron microscopy	24-25	
2.7. X-Ray Diffraction Analysis	25-26	
2.8. Atomic Force Microscopy	26-27	
2.9. Reflectance measurement system	27	
References	28	
Chapter 3: The formation of simultaneous dual-scaled gratings		
by femtosecond laser irradiation	29-53	
3.1 Introduction		
3.2. Experimental procedure		
3.3. Results and Discussions		
3.3.1. Effect of incident laser fluence on LIPSS		
3.3.2. The optimal laser fluence for formation threshold,		
ladder structures, and destruction of LIPSS	38-39	

3.3.3. Systematic modulation of the LIPSS	
with the incident wavelengths	39-41
3.3.4. Effect of periodicity with wavelength for	
The best ladder-like structures	41-43
3.3.5. Behavior of HSFL periodicities with incident	
wavelengths for optimal ladder structures	43-44
3.3.5. Upper limit of LSFL periodicity	44-45
3.4. Conclusion	45-46
References	46-53
Chapter 4: Wavelengths dependent cubic-shaped	
copper nanoparticles formation	55-69
4.1. Introduction	56-57
4.2 Experimental procedure	57-58
4.3 Results and discussions	58-65
4.3.1. Surface morphology	59-63
4.3.1.1. Laser direct writing at 800 nm	59
4.3.1.2. Laser direct writing at the central	
wavelength of 860 nm	59-61
4.3.1.3. Laser direct writing at 900 nm	61-62
4.3.1.4. Laser direct writing at 960 nm	62-63
4.3.2. Elemental Analysis on different surface structures	63-65
4.4. Conclusions	65-66
References	66-69
Chapter 5: Broadband super black stainless-steel surface	
fabricated by nanosecond laser irradiation	71-94
5.1. Introduction	72-74
5.2. Experimental procedure	74-75
5.3. Results and discussions	75-89
5.3.1. Surface morphology	76-78
5.3.2. Reflectivity	78-83
5.3.2.1. Effect of pulse fluence	80
5.3.2.2. Effect of incidence angle	80-81
5.3.2.3. Effect of Incidence beam polarization	81-83
5. 3. 3. Elemental distribution	83-85
5.3.4. X-ray diffraction analysis	85-86
•	

5. 3.5. Evolution of surface morphology over time	86-89	
5. 4. Conclusions References	89 90-94	
Chapter 6: Anisotropic non-wetting metallic surfaces:		
triple contact line theory approach	95-126	
6.1. Introduction	96-98	
6.2. Experimental Procedure	98-100	
6.3. Results and discussions	100-121	
6. 3.1. TCL theory on superhydrophobic substrates	100-110	
6.3.2. Validity of TCL theory from hydrophilic		
to superhydrophobic surfaces	110-121	
6.3.2.1. Spreading dynamics of the droplet		
immediately after fabrication	113-114	
6.3.2.2. Surface evolution from Petal effect		
to lotus leaf behavior	115	
6.3.2.3. The effect of line spacing and multiple scans		
on the anisotropic CAs	115-117	
6.3.2.4. Triple contact line theory and its approach		
to the hydrophilic surfaces	117-120	
6.3.2.5. TCL analysis for droplets on the		
patterned Cu and SS surfaces	120-121	
6.4. Conclusion	121	
References	122-126	
Chapter 7: Summary and future work	127-129	
List of publications	131-133	
Journal publications		
Conference proceedings		
Conference and Workshops		

#### Chapter 1

#### Introduction

#### Abstract

The last few decades have seen growing interest in studying novel micro-nanotexturing towards the various applications and fundamental investigations. Among the many sophisticated techniques, ultrafast laser direct writing emerged as a promising tool due to its capability in single-step, a precise micromachine, pollution-free and easy control. This chapter covers the advent of lasers, the historical background of the pulsed laser materials processing and development, the breakthrough in the generation in subwavelength gratings. It enlightens the various theoretical models regarding the origin of laser-induced periodic surface structures (LIPSS) formation. It also deals with recent progress in forming exotic shapes of LIPSS in different experimental conditions. This chapter also details the potential applications of surface nanostructuring in different experimental conditions such as fabricating copper nanoparticles (CuNP), engineering non-wetting surfaces, and broadband absorption surfaces.

#### 1.1. Introduction

The development of an enormous intensity light source, Light Amplification by Stimulated Emission of Radiation (LASER), is perhaps one of the best inventions in science. It was Albert Einstein who laid the foundation in 1917 for the development of laser by introducing the concepts of stimulated emission, where a photon interacts with an excited molecule or atom and generates the emission of a photon having the same frequency, phase, polarization state, and direction [1]. Some properties such as monochromaticity, high directionality, low divergence, high beam intensity, and coherence make the laser unique. The first laser was invented on May 16, 1960, by T. H. Maiman, inspired by the theoretical concept developed by C.H. Townes and A. L. [2,3]. The invention of commercial lasers accelerated the development of science and technology so that the laser was considered 'a solution seeking for a problem!'. With time the technological developments of lasers are continued across the world for the increasing demands in various applications. The real breakthrough came after developing the concepts of chirped pulse amplification (CPA), which allows a laser to achieve amplification up to the petawatt power [4]. Donna Strickland and Geraud Mourou carried out this pioneering work in the mid-1980s at the University of Rochester, and they were awarded the Nobel prize in 2018 for achieving this extraordinary feat. The invention of ultrashort pulses opens a new horizon in basic sciences and industrial applications.

The ultrashort laser interacts with matter by exciting the surface electron of solid into the higher-lying unoccupied states by absorption of photons either by the interband transition or via the transition of free carriers within the conduction band (intraband transition) through free-carrier excitations [5–7]. Single-photon absorption is possible if the photon frequency is larger than the bandgap frequency of the materials, such as most of the conducting material (Ag, Cu, Al). The electron cannot excite by single-photon absorption for larger bandgap materials, and it might be excited through multi-photon, nonlinear

absorption. Multiphoton and avalanche ionization play a significant role in nonlinear absorption under the influence of high-intense pulse by electron excitation through simultaneous absorption of a few photons. The conduction band electron can absorb multi-photon sequentially and excite to higher states. After absorbing a sufficient number of photons (say n photons) and exceeding the bandgap energy (nhv > Eg), the electron ionizes another electron in the valence band by multiple collisions among the electrons. The number of free carriers in the conduction band increases substantially due to the collisional ionization, leading to the avalanche ionization. The leading and trailing edges of the femtosecond pulse triggered the photo and avalanche ionization during the lasermatter interaction [8]. With the presence of high intense laser pulse, multi-photon absorption and impact ionization enable to a condition of optical breakdown leading to a plasma state [9,10]. The interaction mechanisms between ultrashort pulses with matter are significantly different from those with continuous or long pulse lasers.

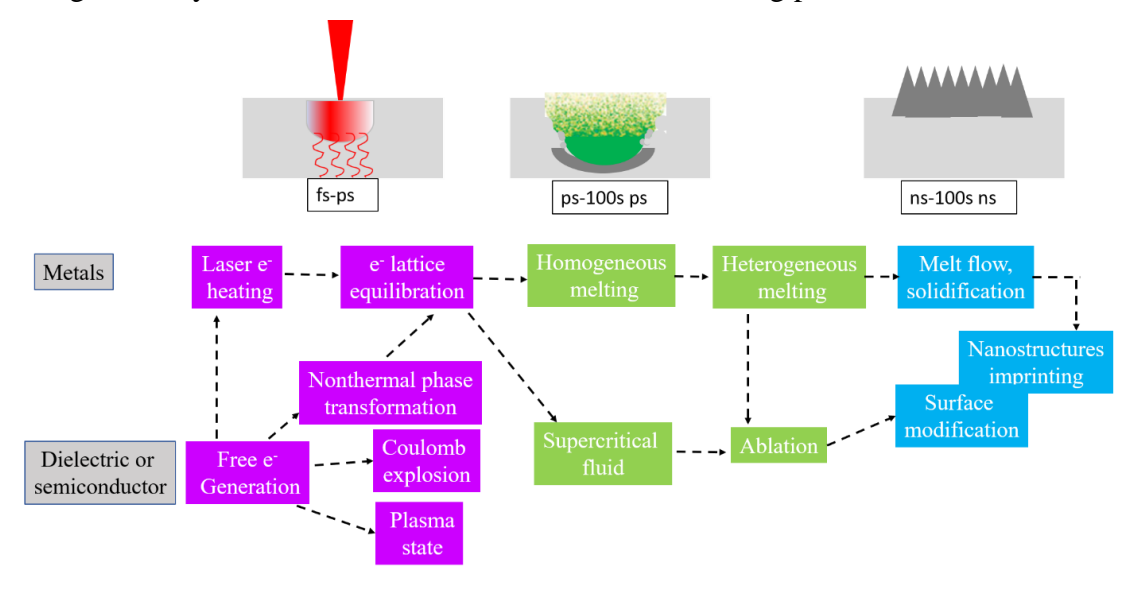


Fig. 1: Laser-matter interaction mechanism

The deposition of energy into the materials has a shorter timescale than the relaxation process. The electrons absorb the photon energy almost instantaneously, and ions remain undisturbed; the thermalization takes place after the laser pulse is turned off. A flowchart of intertwined mechanisms triggered by the ultrashort pulses in metal, semiconductors, and dielectrics is presented in **Fig. 1**. The process is discussed in three classes (shown in

colors); namely, the initial process involves the excitation of electrons in response to the laser irradiation (pink), fast non-equilibrium phase transformations by the energy exchange from excited electrons to the lattice vibrations (green), and the rapid cooling and re-solidifications near the heat-affected zone (HAZ) which leads to the surface modification or ripples formation (indigo). In dielectric or semiconductors, many free electrons are excited across the bandgap by laser irradiation leading to the non-thermal phase transformation influenced by transient modification of interatomic bonding [11,12]. Within ps timescale, excited electrons in the conduction band, both in dielectrics and metals, can absorb photons seeded with laser pulses, causing plasma states or a Coulomb explosion [13]. The electrons transport energy to the lattice, causing rapid heating of 10<sup>14</sup> K/s and the generation of supercritical fluid or homogeneous melting[14– 16]. The excessive-high temperature and pressure generate the metastable state as complex surface morphology during the photomechanical spallation [17–23]. Following that, once temperatures are below the melting point, re-solidification occurs. Due to strong laser energy localization and high heat conductivity, the cooling rate in metals can exceed 10<sup>12</sup> K/s, allowing the material to undergo intense undercooling, resulting in the development of crater formations/deformations nanocrystalline and amorphous solid nanostructures [24–28].

In recent years, ultrashort laser micro/nano surface texturing has emerged as one of the frontiers and the cutting edge of surface science in the development of manufacturing technology due to its capability of high precision and controlled micromachining. It has attracted significant interest due to great potential applications in generating laser-induced nanogratings far beyond the diffraction limit [29–31], anti-reflectivity[32–34], non-wettability [35–37], wicking property [38], tribology [39], drag reduction technology [40], etc. This thesis employed three different lasers to design functional surfaces in pulsed laser surface nanostructuring. Femtosecond Ti: Sapphire laser of pulse duration 75 fs (at full width at half maxima) and fundamental wavelength of 800 nm coupled with commercial optical parametric amplifier (OPA) is to engineered dual-scaled gratings on stainless steel (SS304) and cubic-shaped copper nanoparticles (CuNPs) on copper foil. Femtosecond diode-pumped fiber laser of pulse duration 350 fs and fundamental

wavelength of 1030 nm is utilized to fabricate anisotropic superhydrophobic surface on copper and stainless-steel surfaces. Nd: YAG nanosecond laser of pulse duration 6 ns and second harmonic wavelength of 532 nm (fundamental 1064 nm) is used to develop broadband super black surfaces on stainless steel.

#### 1.2. Dual-scaled gratings fabrication

M. Birnbaum observed the first laser-induced surface ripples in single-crystal germanium using a ruby laser in 1965 [41]. LIPSS research has attracted considerable attention from the research community since then, including over 1300 research publications so far. The formation of the subwavelength gratings under the influence of the laser pulses is universally observed on several materials [36–40]. Low spatial frequency LIPSS (LSFL) and high spatial frequency LIPSS (HSFL) are the two primary classes of LIPSS generated by ultrashort linearly polarised light pulses incident on a material [42–44]. A pioneering and comprehensive electromagnetic theory is established by Sipe et al. on LIPSS formation based on the effect of surface roughness on the electromagnetic field distribution, which is popularly known as efficacy theory [45]. It stipulates that LSFL formed due to inhomogeneous deposition of energy by interfering the incident laser with surface scattered electromagnetic wave, which is widely accepted today [46,47]. The gratings are significantly smaller than the laser wavelength, forming either orthogonal or parallel to the laser polarization; lower periodic structures are generally referred to as high spatial frequency LIPSS (HSFL); these are parallel or orthogonal to the incident polarization and the formation HSFL is not entirely understood [46]. Recently, several reports of some LIPSS features that can be considered dual-scaled ripples where HSFL gratings are embedded between the LSFL gratings [17,48]. This thesis investigates the simultaneous formation of dual-scaled gratings structure and explores the spatial periodicity variation for the incident laser wavelength over a broad range from 400-2200 nm.

#### 1.3. Cubic-shaped copper nanoparticles processing

The fabrication of metallic nanoparticles (NPs) gained tremendous attention from the research communities due to their diverse applications in industry and academia [49–51]. These various needs have been justified by rapid synthesis and preparation of NPs with

different shapes, sizes, and morphology using various methods such as solution-based preparation, e-beam lithography, extraction from the natural biological plants, and laser-induced NPs synthesis [52–56], etc. Fabrication of NPs using ultrafast laser irradiation provides a way for an easy, one-step, and green synthesis of nanoparticles. It is a reliable technique because of its repeatability, controlled, precise fabrication, and pollution-free method [53,57–59]. Among the class of nanoparticles, the copper NPs got special attention due to their excellent performance in heat and electrical conductivity, catalytic activity, and cost-effectiveness compared to the other plasmonic metal NPs such as gold and silver [51,60].

#### 1.4. Broadband superblack surface

Recently, surface structuring at the nanoscale has been extensively used where there is a need for low reflective surfaces, such as display devices [61,62], solar cell panels [63], light-emitting diodes [64], optoelectronics [65], etc. The laser surface patterning is very effective for fabricating anti-reflective (AR) surfaces. It is a single-step process that can be scaled to the industry with precise, controllable parameters. In our work in this thesis, we demonstrated near 99.5% absorbance over the range of 250 nm to 1800 nm using the inexpensive nanosecond laser on the stainless steel (SS). These nanoseconds laser-irradiated SS surfaces are efficient in light trapping due to the fascinating micro-nano hierarchal structures.

#### 1.5. Anisotropic superhydrophobicity

A liquid droplet forms a spherical shape on an isotropic superhydrophobic surface, with contact angles (CAs) varied depending on the surface properties. The "lotus leaf action" depicts how droplets roll off the natural surfaces with slight perturbation [66]. The mimicking of the natural surface is engineered artificially on a variety of surfaces, including ZnO nanorods[67], metallic surfaces[68,69], polymers [40], etc. Wenzel [70] and Cassie-Baxter [71,72] models extensively discuss liquid wetting on two-dimensional symmetric surfaces. According to the Wenzel model, a liquid droplet penetrates the surface's micro-cavities. These models suggest that CAs are influenced by surface roughness. D. C. Pease demonstrated that contact angle formation is a one-dimensional problem[73] and suggested that the droplet pinning boundary at the triple contact line

determined the contact angle. But the idea of Pease is ignored by contemporary surface scientists, and Wenzel and Cassie-Baxter models got the most attention of the surface science investigation. The CA behavior (advancing, receding, and hysteresis), according to Gao, is determined exclusively by interactions between the liquid and the solid at the three-phase contact line and the interfacial area within the contact perimeter is irrelevant[74]. H. Y. Erbil examines the dependency of CAs on a three-phase contact line in detail[75,76]. Liu et al. examined Gao's work extensively to explain the wetting mechanism of symmetrical droplets [77]. The formation of spherical sessile droplets on a smooth surface is far from realistic; instead, droplets with ellipsoidal shapes are formed under gravity's action. The study of anisotropicity in CAs of a droplet on micro-grooved surfaces has gained immense attention to researchers due to its potential applications[78,79]. Surface topography has two orthogonal geometric directions: along the laser writing line (along the grooves) and orthogonal to the laser writing line (perpendicular to the grooves). The CAs in the orthogonal direction of laser grooves were higher than the CAs along the groove. Droplets on these surfaces are not spherical; they get stretched in the groove direction because there is no barrier to liquid flow but squeezed in the perpendicular direction due to the presence of groove barriers [78,80]. Our new analysis used TCL theory to define a relationship between the effective volume of ellipsoidal droplets and CAs, and successfully proved a remarkable correlation between theory and experiment. This study used mathematical formalism to analyze this idea from hydrophilic to superhydrophobic surfaces.

#### 1.6. Organization of the thesis

Chapter 1 (Introduction) focuses on the introduction and historical foundations of ultrafast nanostructuring and contemporary breakthroughs in the field. It covers the most important breakthroughs and ground-breaking elements of ultrafast surface nanostructuring to date. This chapter discusses how surface nanostructuring might lead to prospective and industrial applications in the present and recent technological advancements.

Chapter 2 (Experimental methods) deals with ultrashort laser direct writing techniques using different laser sources such femtosecond Ti: Sapphire, femtosecond diode pump fiber laser, and nanosecond Nd: YAG laser system. A brief remark on the commercial Optical Parametric Amplifier (OPA) is addressed, used to tune the fundamental laser wavelength to required wavelengths. We discussed structural and spectroscopic characterization techniques employed in this dissertation, including UV-Visible absorption spectroscopy, Field emission scanning electron microscopy (FESEM), Atomic Force Microscopy (AFM), and X-ray Diffraction Microscopy (XRD).

Chapter 3 (Controlled dual-scaled gratings) presents the nanoscale management of unusual ladder-type ripples on stainless steel surfaces over a broad incident range of wavelengths of 400-2200 nm is presented in. It explains the detailed account of the origin of combined structures of LSFL and HSFL. The HSFL features are extraordinary because they formed between the two LSFL gratings structures and deep inside the groves. The HSFL lies inside the LSFL in quasi-spaced intervals, and combined structures resemble a ladder structure. In addition to that, this chapter discusses the variation of spatial periodicity of LSFL and HSFL with incident wavelength. This research establishes an upper limit on spatial periodicity by demonstrating that the LIPSS periodicity cannot rise with increasing incidence wavelength.

Chapter 4 (wavelength-dependent cubic-shaped copper nanoparticles) deals with the wavelength-dependent cubic nanoparticles formation on copper surfaces by femtosecond laser irradiation. In this chapter, the fabrication of cubic shaped nanoparticles is discussed incident various combinations of laser parameters. The size of the nanoparticles is analyzed for different incident fluences for the fixed incident wavelength of 860 nm. The attractive and exciting fact is that among the four incident wavelengths used in this investigation, the cubic nanoparticles formed only at the incident wavelength of 860 nm. Apart from the LSFL, we observe the formation of cubic-shaped copper nanoparticles of variable sizes.

Chapter 5 (Broadband perfect black surfaces) discusses the broadband absorption of nanostructured stainless-steel surfaces fabricated by nanosecond laser irradiation. The stainless-steel surfaces are irradiated with a various fluence of ns pulsed laser in

overlapping conditions via raster scanning mode to fabricate highly broadband absorption surfaces. The measured specular anti-reflection properties over a broad spectral region (250-1800 nm) are extremely low, less than 0.5%, over an extensive range of incident angles and for both orthogonal polarizations.

Chapter 6 (Anisotropic superhydrophobicity) discusses the fabrication of anisotropic superhydrophobic copper and stainless-steel surfaces by irradiating the femtosecond high repetition rate IR laser and the formation of ellipsoidal droplets on these surfaces. By varying the laser writing line spacing, we optimized the best conditions for the Cu surface to behave as superhydrophobic with CA as much as  $172^{\circ}$ . Droplets formed ellipsoidal shapes due to the anisotropic surface morphology of the surfaces. We measured the dimensions of these ellipsoidal droplets from hydrophilic (CA as low as  $37^{\circ}$ ) to superhydrophobic cases (as high as  $172^{\circ}$ ). Expressions for the ellipsoidal droplet volume estimations were presented for the entire range of CAs. A dimensionless volume function,  $f(\theta x, \theta y)$ , uniquely depends on the droplet's dimensions is presented.

Chapter 7 (summary and future prospective works) summarizes the thesis by focusing on the important findings achieved as a part of the research activity described in the previous chapters. Then we conclude the chapter with possible ways to further investigate the underlying mechanism of laser LIPSS.

#### References

- [1] N. Straumann, Einstein in 1916: "On the Quantum Theory of Radiation," 18 (2017) 1–5. http://arxiv.org/abs/1703.08176.
- [2] © 1960 Nature Publishing Group, (1960).
- [3] A.L. Schawlow, C.H. Townes, Infrared and optical masers, Phys. Rev. 112 (1958) 1940–1949. https://doi.org/10.1103/PhysRev.112.1940.
- [4] D. Strickland, G. Mourou, Compression of amplified chirped optical pulses, Opt. Commun. 56 (1985) 219–221. https://doi.org/10.1016/0030-4018(85)90120-8.
- [5] N. Bloembergen, Fundamentals of Laser-Solid Interactions., Highw. Eng. 1 (1979)

- 1–11. https://doi.org/10.1063/1.31659.
- [6] R. Domański, M. Jaworski, M. Rebow, Laser radiation interaction with solids, J. Power Technol. 79 (1995) 4–18.
- [7] M. V. Shugaev, C. Wu, O. Armbruster, A. Naghilou, N. Brouwer, D.S. Ivanov, T.J.Y. Derrien, N.M. Bulgakova, W. Kautek, B. Rethfeld, L. V. Zhigilei, Fundamentals of ultrafast laser-material interaction, MRS Bull. 41 (2016) 960–968. https://doi.org/10.1557/mrs.2016.274.
- [8] B. Stuart, M. Feit, S. Herman, A. Rubenchik, B. Shore, M. Perry, Nanosecond-to-femtosecond laser-induced breakdown in dielectrics, Phys. Rev. B Condens. Matter Mater. Phys. 53 (1996) 1749–1761. https://doi.org/10.1103/PhysRevB.53.1749.
- [9] E. Yablonovitch, N. Bloembergen, Avalanche ionization and the limiting diameter of filaments induced by light pulses in transparent media, Phys. Rev. Lett. 29 (1972) 907–910. https://doi.org/10.1103/PhysRevLett.29.907.
- [10] A.C. Tien, S. Backus, H. Kapteyn, M. Murnane, G. Mourou, Short-pulse laser damage in transparent materials as a function of pulse duration, Phys. Rev. Lett. 82 (1999) 3883–3886. https://doi.org/10.1103/PhysRevLett.82.3883.
- [11] A. Rousse, C. Rischel, S. Fourmaux, I. Uschmann, S. Sebban, G. Grillon, P. Balcou, E. Förster, J.P. Geindre, P. Audebert, J.C. Gauthier, D. Hulin, Non-thermal melting in semiconductors measured at femtosecond resolution, Nature. 410 (2001) 65–67. https://doi.org/10.1038/35065045.
- [12] M. Hase, P. Fons, K. Mitrofanov, A. V. Kolobov, J. Tominaga, Femtosecond structural transformation of phase-change materials far from equilibrium monitored by coherent phonons, Nat. Commun. 6 (2015) 1–6. https://doi.org/10.1038/ncomms9367.
- [13] N.M. Bulgakova, R. Stoian, A. Rosenfeld, I. V. Hertel, E.E.B. Campbell,

- Electronic transport and consequences for material removal in ultrafast pulsed laser ablation of materials, Phys. Rev. B Condens. Matter Mater. Phys. 69 (2004) 1–12. https://doi.org/10.1103/PhysRevB.69.054102.
- [14] B. Rethfeld, K. Sokolowski-Tinten, D. von der Linde, S.I. Anisimov, Ultrafast thermal melting of laser-excited solids by homogeneous nucleation, Phys. Rev. B
   -Condens. Matter Mater. Phys. 65 (2002) 1–4. https://doi.org/10.1103/PhysRevB.65.092103.
- [15] D.S. Ivanov, L. V. Zhigilei, Effect of Pressure Relaxation on the Mechanisms of Short-Pulse Laser Melting, Phys. Rev. Lett. 91 (2003) 1–4. https://doi.org/10.1103/PhysRevLett.91.105701.
- [16] K. Sokolowski-Tinten, J. Bialkowski, A. Cavalleri, D. Von der Linde, A. Oparin, J. Meyer-Ter-Vehn, S.I. Anisimov, Transient states of matter during short pulse laser ablation, Phys. Rev. Lett. 81 (1998) 224–227. https://doi.org/10.1103/PhysRevLett.81.224.
- [17] A.Y. Vorobyev, C. Guo, Direct femtosecond laser surface nano/microstructuring and its applications, Laser Photonics Rev. 7 (2013) 385–407. https://doi.org/10.1002/lpor.201200017.
- [18] A. Vailionis, E.G. Gamaly, V. Mizeikis, W. Yang, A. V Rode, Evidence of superdense aluminium synthesized by ultrafast microexplosion, Nat. Commun. (2011) 1–6. https://doi.org/10.1038/ncomms1449.
- [19] L. Rapp, B. Haberl, C.J. Pickard, J.E. Bradby, E.G. Gamaly, J.S. Williams, A. V Rode, Experimental evidence of new tetragonal polymorphs of silicon formed through ultrafast laser-induced confined microexplosion, Nat. Commun. (2015). https://doi.org/10.1038/ncomms8555.
- [20] A.Y. Vorobyev, C. Guo, Enhanced absorptance of gold following multipulse femtosecond laser ablation, (2005) 1–5. https://doi.org/10.1103/PhysRevB.72.195422.

- [21] Y. Dai, M. He, H. Bian, B. Lu, X. Yan, Femtosecond laser nanostructuring of silver film, (2012) 567–574. https://doi.org/10.1007/s00339-011-6705-5.
- [22] V. Ocelík, J.C. Rao, J.Z.P. Skolski, G.R.B.E. Römer, J.V. Obo, A.J. Huis, J.T.M. De Hosson, Applied Surface Science Modification of Cu surface with picosecond laser pulses, 303 (2014) 118–124. https://doi.org/10.1016/j.apsusc.2014.02.104.
- [23] P.E. Dyer, Photomechanical Processes and Effects in Ablation, (2003).
- [24] C. Lin, F. Spaepen, D. Turnbull, No Title, 62 (1984) 767–772.
- [25] C. Wu, M.S. Christensen, J. Savolainen, P. Balling, L. V Zhigilei, Generation of subsurface voids and a nanocrystalline surface layer in femtosecond laser irradiation of a single-crystal Ag target, 035413 (2015) 1–14. https://doi.org/10.1103/PhysRevB.91.035413.
- [26] X. Sedao, M. V Shugaev, C. Wu, T. Douillard, C. Esnouf, C. Maurice, F. Pigeon, F. Garrelie, L. V Zhigilei, J. Colombier, Growth Twinning and Generation of High-Frequency Surface Nanostructures in Ultrafast Laser-Induced Transient Melting and Resolidi fi cation, (2016). https://doi.org/10.1021/acsnano.6b02970.
- [27] J.A. Alonso, BY ION BEAM MIXING AND BY LASER QUENCHING, 4 (1986) 5–8.
- [28] C. Wu, L. V Zhigilei, Nanocrystalline and Polyicosahedral Structure of a Nanospike Generated on Metal Surface Irradiated by a Single Femtosecond Laser Pulse, (2016). https://doi.org/10.1021/acs.jpcc.6b00013.
- [29] M.T. Li, M. Liu, H.B. Sun, Surface nanostructuring: Via femtosecond lasers, Phys. Chem. Chem. Phys. 21 (2019) 24262–24268. https://doi.org/10.1039/c9cp05351d.
- [30] H. Zhang, J.P. Colombier, S. Witte, Laser-induced periodic surface structures: Arbitrary angles of incidence and polarization states, Phys. Rev. B. 101 (2020) 1–15. https://doi.org/10.1103/PhysRevB.101.245430.
- [31] I. Gnilitskyi, T.J.Y. Derrien, Y. Levy, N.M. Bulgakova, T. Mocek, L. Orazi, High-

- speed manufacturing of highly regular femtosecond laser-induced periodic surface structures: Physical origin of regularity, Sci. Rep. 7 (2017) 1–11. https://doi.org/10.1038/s41598-017-08788-z.
- [32] M.A. Taher, S. Ponnan, H. Prasad, D.N. Rao, S.R.G. Naraharisetty, Broadband absorption of nanostructured stainless steel surface fabricated by nanosecond laser irradiation, Nanotechnology. 31 (2020) 175301. https://doi.org/10.1088/1361-6528/ab674e.
- [33] M.A. Taher, S.R.G. Naraharisetty, D. Narayana Rao, Super black stainless steel surface fabricated by nanosecond laser irradiation, Opt. InfoBase Conf. Pap. Part F181- (2020). https://doi.org/10.1364/CLEO\_AT.2020.JW2B.21.
- [34] G. Tang, A.C. Hourd, A. Abdolvand, Nanosecond pulsed laser blackening of copper, Appl. Phys. Lett. 101 (2012). https://doi.org/10.1063/1.4769215.
- [35] M.A. Taher, V.K. Rajput, N. Krishnan P K, S.R.G. Naraharisetty, The validity of triple contact line theory from hydrophilic to superhydrophobic surfaces, J. Phys. D. Appl. Phys. 55 (2022) 055305. https://doi.org/10.1088/1361-6463/ac30b8.
- [36] M.A. Taher, H. Prasad, P.K. Navanith Krishnan, N.R. Desai, S.R.G. Naraharisetty, Ellipsoidal droplet formation on anisotropic superhydrophobic copper surface, Surf. Topogr. Metrol. Prop. 7 (2019). https://doi.org/10.1088/2051-672X/ab2d80.
- [37] J. Long, M. Zhong, H. Zhang, P. Fan, Superhydrophilicity to superhydrophobicity transition of picosecond laser microstructured aluminum in ambient air, J. Colloid Interface Sci. 441 (2015) 1–9. https://doi.org/10.1016/j.jcis.2014.11.015.
- [38] A.Y. Vorobyev, C. Guo, Superwicking Surfaces Produced by Femtosecond Laser, (n.d.) 101–115. https://doi.org/10.1007/978-94-017-9481-7.
- [39] J. Bonse, R. Koter, M. Hartelt, D. Spaltmann, S. Pentzien, S. Höhm, A. Rosenfeld, J. Krüger, Tribological performance of femtosecond laser-induced periodic surface structures on titanium and a high toughness bearing steel, Appl. Surf. Sci. 336

- (2015) 21–27. https://doi.org/10.1016/j.apsusc.2014.08.111.
- [40] R. Di Mundo, F. Bottiglione, M. Notarnicola, F. Palumbo, G. Pascazio, Plasma-Textured Teflon: Repulsion in Air of Water Droplets and Drag Reduction Underwater, (2017) 1–13. https://doi.org/10.3390/biomimetics2010001.
- [41] M. Birnbaum, Semiconductor surface damage produced by Ruby lasers, J. Appl. Phys. 36 (1965) 3688–3689. https://doi.org/10.1063/1.1703071.
- [42] J. Bonse, Quo vadis LIPSS?—recent and future trends on laser-induced periodic surface structures, Nanomaterials. 10 (2020) 1–19. https://doi.org/10.3390/nano10101950.
- [43] R. Le Harzic, D. Dörr, D. Sauer, M. Neumeier, M. Epple, H. Zimmermann, F. Stracke, Large-area, uniform, high-spatial-frequency ripples generated on silicon using a nanojoule-femtosecond laser at high repetition rate, Opt. Lett. 36 (2011) 229. https://doi.org/10.1364/ol.36.000229.
- [44] M.H. Dar, R. Kuladeep, V. Saikiran, N.D. Rao, Femtosecond laser nanostructuring of titanium metal towards fabrication of low-reflective surfaces over broad wavelength range, Appl. Surf. Sci. 371 (2016) 479–487. https://doi.org/10.1016/j.apsusc.2016.03.008.
- [45] J.E. Sipe, J.F. Young, J.S. Preston, H.M. van Driel, Laser-induced periodic surface structure. I. Theory, Phys. Rev. B. 27 (1983) 1141–1154. https://doi.org/10.1103/PhysRevB.27.1141.
- [46] J. Bonse, S. Gräf, Maxwell Meets Marangoni—A Review of Theories on Laser-Induced Periodic Surface Structures, Laser Photonics Rev. 14 (2020) 1–25. https://doi.org/10.1002/lpor.202000215.
- [47] H. Zhang, J.P. Colombier, C. Li, N. Faure, G. Cheng, R. Stoian, Coherence in ultrafast laser-induced periodic surface structures, Phys. Rev. B Condens. Matter Mater. Phys. 92 (2015) 1–14. https://doi.org/10.1103/PhysRevB.92.174109.

- [48] C. Albu, A. Dinescu, M. Filipescu, M. Ulmeanu, M. Zamfirescu, Periodical structures induced by femtosecond laser on metals in air and liquid environments, Appl. Surf. Sci. 278 (2013) 347–351. https://doi.org/10.1016/j.apsusc.2012.11.075.
- [49] G.H. Chan, J. Zhao, E.M. Hicks, G.C. Schatz, R.P. Van Duyne, Plasmonic properties of copper nanoparticles fabricated by nanosphere lithography, Nano Lett. 7 (2007) 1947–1952. https://doi.org/10.1021/nl070648a.
- [50] A. Radi, D. Pradhan, Y. Sohn, K.T. Leung, Nanoscale Shape and Size Control of, ACS Nano. 4 (2010) 1553–1560.
- [51] M.B. Gawande, A. Goswami, F.X. Felpin, T. Asefa, X. Huang, R. Silva, X. Zou, R. Zboril, R.S. Varma, Cu and Cu-Based Nanoparticles: Synthesis and Applications in Catalysis, Chem. Rev. 116 (2016) 3722–3811. https://doi.org/10.1021/acs.chemrev.5b00482.
- [52] P. Liu, H. Wang, X. Li, M. Rui, H. Zeng, Localized surface plasmon resonance of Cu nanoparticles by laser ablation in liquid media, RSC Adv. 5 (2015) 79738–79745. https://doi.org/10.1039/c5ra14933a.
- [53] C. Wei, Q. Liu, Shape-, size-, and density-tunable synthesis and optical properties of copper nanoparticles, CrystEngComm. 19 (2017) 3254–3262. https://doi.org/10.1039/c7ce00750g.
- [54] A.R. Sadrolhosseini, A.S.B.M. Noor, K. Shameli, G. Mamdoohi, M.M. Moksin, M. Adzir Mahdi, Laser ablation synthesis and optical properties of copper nanoparticles, J. Mater. Res. 28 (2013) 2629–2636. https://doi.org/10.1557/jmr.2013.244.
- [55] M.I. Din, R. Rehan, Synthesis, Characterization, and Applications of Copper Nanoparticles, Anal. Lett. 50 (2017) 50–62. https://doi.org/10.1080/00032719.2016.1172081.

- [56] J. Zizzo, Toxicity effects of Cubic Cu2O nanoparticles on defecation rate and length in C. Elegans, Biomed. Res. Ther. 7 (2020) 4045–4051. https://doi.org/10.15419/bmrat.v7i10.639.
- [57] M. Muniz-Miranda, C. Gellini, E. Giorgetti, Surface-enhanced Raman scattering from copper nanoparticles obtained by laser ablation, J. Phys. Chem. C. 115 (2011) 5021–5027. https://doi.org/10.1021/jp1086027.
- [58] P.K. Baruah, A. Singh, L. Rangan, A.K. Sharma, A. Khare, Optimization of copper nanoparticles synthesized by pulsed laser ablation in distilled water as a viable SERS substrate for karanjin, Mater. Chem. Phys. 220 (2018) 111–117. https://doi.org/10.1016/j.matchemphys.2018.08.064.
- [59] M.I.S.M.H. Tan, A.F. Omar, M. Rashid, U. Hashim, VIS-NIR spectral and particles distribution of Au, Ag, Cu, Al and Ni nanoparticles synthesized in distilled water using laser ablation, Results Phys. 14 (2019) 102497. https://doi.org/10.1016/j.rinp.2019.102497.
- [60] A. Tamilvanan, K. Balamurugan, K. Ponappa, B.M. Kumar, Copper nanoparticles: Synthetic strategies, properties and multifunctional application, Int. J. Nanosci. 13 (2014). https://doi.org/10.1142/S0219581X14300016.
- [61] N. Liu, M. Mesch, T. Weiss, M. Hentschel, H. Giessen, Infrared perfect absorber and its application as plasmonic sensor, Nano Lett. 10 (2010) 2342–2348. https://doi.org/10.1021/nl9041033.
- [62] H.K. Raut, V.A. Ganesh, A.S. Nair, S. Ramakrishna, Anti-reflective coatings: A critical, in-depth review, Energy Environ. Sci. 4 (2011) 3779–3804. https://doi.org/10.1039/c1ee01297e.
- [63] J.W. Leem, Y.M. Song, J.S. Yu, Broadband anti-reflective germanium surfaces based on subwavelength structures for photovoltaic cell applications, Opt. Express. 19 (2011) 26308. https://doi.org/10.1364/oe.19.026308.

- [64] P.I.P. Ichon, A.D.B. Arbet, J.E.A.N.H.B. Lanchot, F.R.D. Ruon, F.R.B. Alembois, P.A.G. Eorges, Light-emitting diodes: a new paradigm for Ti: sapphire pumping, 5 (2018).
- [65] F.F. Mahani, A. Mokhtari, TiO 2 Circular Nano-Gratings as Anti-Reflective Coatings and Potential Color Filters for Efficient Organic Solar Cells , J. Nanoelectron. Optoelectron. 13 (2018) 1624–1629. https://doi.org/10.1166/jno.2018.2412.
- [66] Z. Guo, W. Liu, B.L. Su, Superhydrophobic surfaces: From natural to biomimetic to functional, J. Colloid Interface Sci. 353 (2011) 335–355. https://doi.org/10.1016/j.jcis.2010.08.047.
- [67] M.T.Z. Myint, G.L. Hornyak, J. Dutta, One pot synthesis of opposing "rose petal" and "lotus leaf" superhydrophobic materials with zinc oxide nanorods, J. Colloid Interface Sci. 415 (2014) 32–38. https://doi.org/10.1016/j.jcis.2013.10.015.
- [68] A. He, W. Liu, W. Xue, H. Yang, Y. Cao, Nanosecond laser ablated copper superhydrophobic surface with tunable ultrahigh adhesion and its renewability with low temperature annealing, Appl. Surf. Sci. 434 (2018) 120–125. https://doi.org/10.1016/j.apsusc.2017.10.143.
- [69] A.M. Kietzig, S.G. Hatzikiriakos, P. Englezos, Patterned superhydrophobic metallic surfaces, Langmuir. 25 (2009) 4821–4827. https://doi.org/10.1021/la8037582.
- [70] R.N. Wenzel, Resistance of solid surfaces to wetting by water, Ind. Eng. Chem. 28 (1936) 988–994. https://doi.org/10.1021/ie50320a024.
- [71] A.B.D. Cassie, Contact angles, Discuss. Faraday Soc. 3 (1948) 11–16. https://doi.org/10.1039/DF9480300011.
- [72] A.B.D. Cassie, S. Baxter, Of porous surfaces, Trans. Faraday Soc. 40 (1944) 546–551. https://doi.org/10.1103/PhysRevE.64.021514.

- [73] D.C. Pease, THE SIGNIFICANCE OF THE CONTACT ANGLE IN RELATION TO THE SOLID SURFACE, (1944) 107–110.
- [74] L. Gao, T.J. McCarthy, How Wenzel and Cassie Were Wrong, Langmuir. 23 (2007) 3762–3765. https://doi.org/10.1021/la062634a.
- [75] H. Yildirim Erbil, Dependency of contact angles on three-phase contact line: A review, Colloids and Interfaces. 5 (2021). https://doi.org/10.3390/colloids5010008.
- [76] H.Y. Erbil, The debate on the dependence of apparent contact angles on drop contact area or three-phase contact line: A review, Surf. Sci. Rep. 69 (2014) 325–365. https://doi.org/10.1016/j.surfrep.2014.09.001.
- [77] J. Liu, Y. Mei, R. Xia, A new wetting mechanism based upon triple contact line pinning, Langmuir. 27 (2011) 196–200. https://doi.org/10.1021/la103652s.
- [78] Z.L. Wang, E.H. Chen, Y.P. Zhao, The effect of surface anisotropy on contact angles and the characterization of elliptical cap droplets, Sci. China Technol. Sci. 61 (2018) 309–316. https://doi.org/10.1007/s11431-017-9149-1.
- [79] Y. Chen, B. He, J. Lee, N.A. Patankar, Anisotropy in the wetting of rough surfaces, J. Colloid Interface Sci. 281 (2005) 458–464. https://doi.org/10.1016/j.jcis.2004.07.038.
- [80] P. Li, J. Xie, J. Cheng, K.K. Wu, Anisotropic wetting properties on a precision-ground micro-V-grooved Si surface related to their micro-characterized variables, J. Micromechanics Microengineering. 24 (2014). https://doi.org/10.1088/0960-1317/24/7/075004.

# Chapter 2

# **Experimental procedure and methodology**

#### **Abstract**

Ultrashort laser direct writing technique is presented using different laser sources such femtosecond Ti: Saphire, diode pump femtosecond fiber laser, and Nd: YAG nanosecond laser system. A brief remark on the commercial Optical Parametric Amplifier (OPA) is addressed, used to tune the fundamental laser wavelength to required wavelengths. We discussed structural and spectroscopic characterization techniques employed in this dissertation, including UV-Visible absorption spectroscopy, Field emission scanning electron microscopy (FESEM), Atomic Force Microscopy (AFM), and X-ray Diffraction Microscopy (XRD).

#### 2.1. Laser micromachining setup

A laser direct writing set mainly consists of three major units: pulsed laser source, focusing optical component (lens or microscopic objectives), and a three-dimensional nanopositioner stage [1]. The general schematic of the laser direct writing setup is shown in **Fig. 1**. Three different lasers are employed to carry out my research works in this thesis. The laser beam is focused either with a convex lens or microscopic objective lens perpendicularly on the substrate's surface, as shown in **Fig. 1**. The substrates are kept on a three-dimensional nanopositioner s stage (Newport), and the substrate is translated across the laser beam propagation in raster scanning. The motion of the stage is controlled using an ESP motion controller with appropriate scanning speed and line spacing between two successive scans [2].

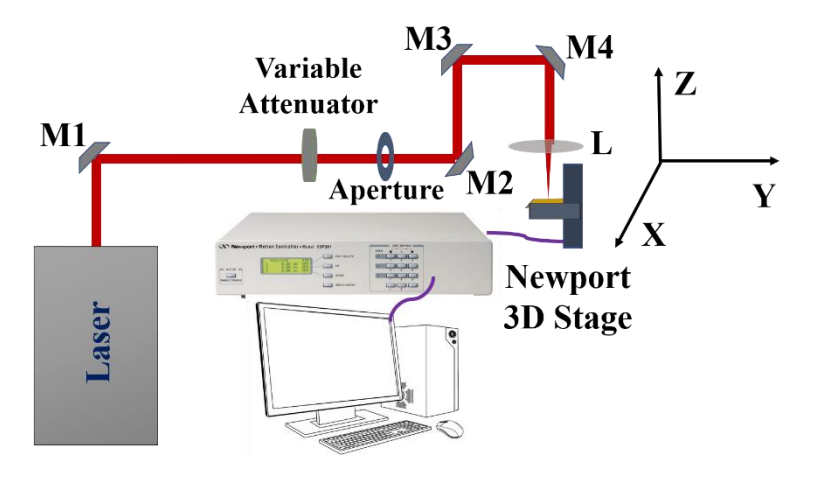


Fig. 1: The schematic of the experimental setup. M: mirrors, L: lens.

#### 2.2. Femtosecond Ti: Sapphire laser

Mode-locked Ti: Sapphire oscillator (Maitai) generates femtosecond seed pulses of nanojoule energy with a high repetition rate (80 MHz and wavelength of 800 nm) [3]. The seed pulse is pumped with a diode laser (Ascend) of a nanosecond pulse of the wavelength of 532 nm. The amplifier (Spitfire Ace, Spectraphysics) amplifies femtosecond pulses emitted by mode-locked Ti: Sapphire lasers at near-infrared wavelengths shown schematically in **Fig. 2**, such as those produced by the Spectra-Physics Mai Tai to produce an output power ~6 Watt and pulsed width of 75 fs at a

repetition rate of 1 kHz. Users can adjust the amplifier to lower repetition rates (with the same energy per pules). A Spitfire Ace system comprises four units: the Spitfire Ace amplifier, the Timing and Delay Generator (TDG) control unit, the Temperature Control Unit (TCU), and a laptop computer operating the Spitfire Ace control software [4]. The core components of the Spitfire Ace amplifier assembly include a pulse stretcher, a Ti: Sapphire regenerative amplifier, and a pulse compressor. The stretcher and compressor are explicitly designed for the pulse width of the input and output pulses for each Spitfire Ace model. The optics, including the pulse stretcher and compressor, are optimized for the specified wavelength range, pulse width, and repetition rate [5].

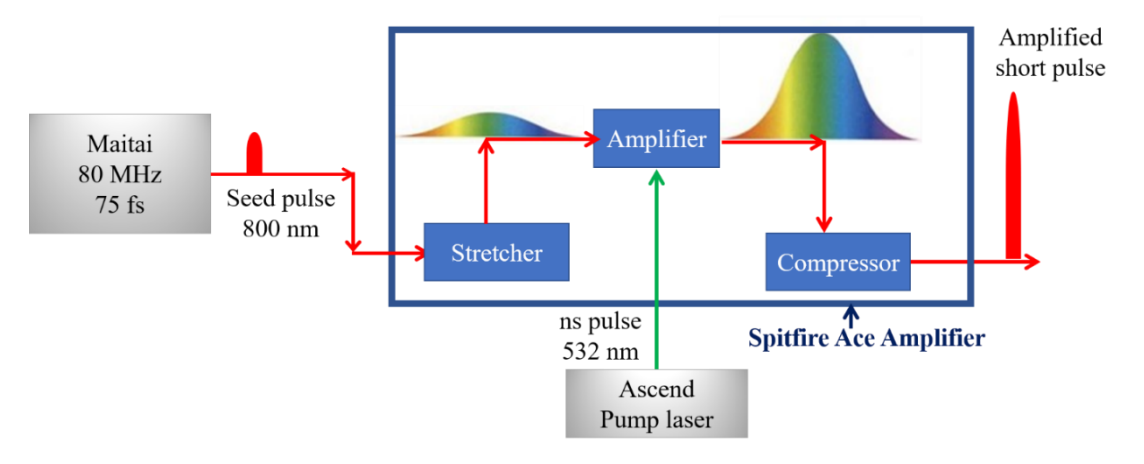


Fig. 2: The schematic of femtosecond laser unit comprises of Maitai oscillator (source of seed pulse), Spitfire Ace (Amplifier), and diode pump nanosecond laser. It shows the flow chart of chirped pulse amplification (CPA).

#### 2.3. Optical parametric amplifier

The TOPAS-Prime (WinTOPAS, TP8F6C1FP), a commercial optical parametric amplifier, is used to tune the wavelength of a fundamental laser beam to the desired and required wavelength. It emits coherent electromagnetic radiation visible and invisible to human eyes (infrared and ultraviolet region) [6]. Good performance of TOPAS-prime requires high pump quality in terms of both temporal and spatial coherence. In other words, an ideal pump has a diffraction-limited and transform-limited, high contrast pulse. TOPAS-Prime is a dual-stage parametric amplifier of a white light continuum. It includes several subunits: pump beam delivery and splitting optics (PO), white-light generator

(WLG), a pre-amplifier of first amplification stage (PA1), and optical fresh pump stage for sum-frequency (FP).

The device uses motorized translation and rotation stages to optimize the positions of specific optics to generate the required wavelength of TOPAS-Prime. The detailed optical layout of the TOPAS-Prime is presented in **Fig. 3**. A small fraction of pump (generally 1-3 µJ) at wavelength 800 nm is needed to generate a white-light continuum (WLC) in a sapphire plate. The WLC beam and another fraction (30-50 µJ) of the pump beam are focused on the pre-amplifier crystal. The pulses are limited and overlapped non-collinearly inside the nonlinear crystal, where parametric amplification occurs. A non-collinear beam path is utilized for hassle-free separation of the amplified signal beam. A beam blocker blocks the residual pump and idler beams after the crystal. The signal beam is expanded and collimated by a lens telescope and transported into the second amplification stage. The power amplifier is usually pumped by the bulk of the input pump beam. A lens-mirror telescope is employed to generate sufficient intensity by reducing pump-beam diameter.

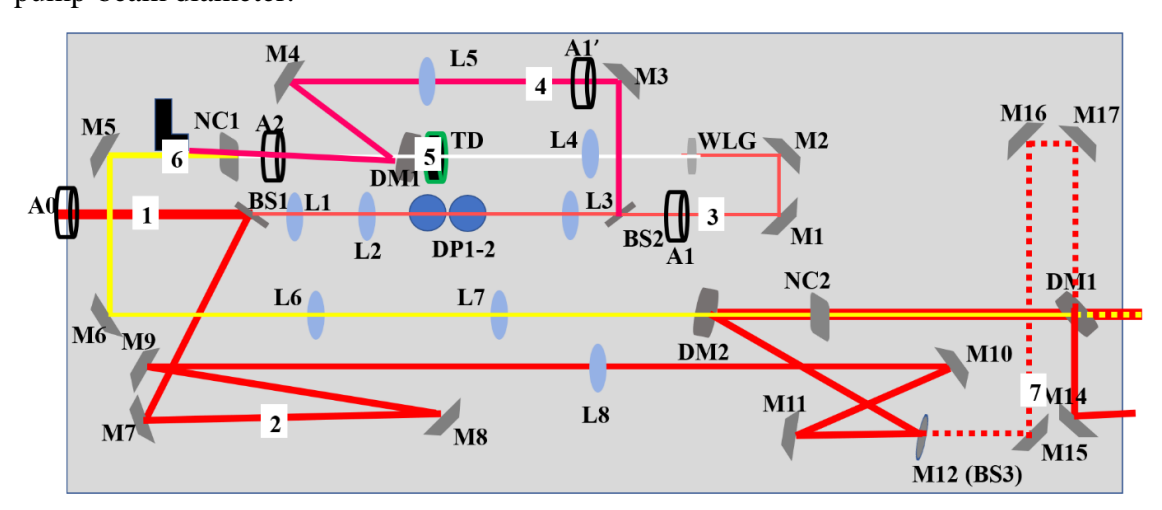


Fig. 3: The schematic layout of the TOPAS-Prime (WinTOPAS, TP8F6C1FP), a commercial optical parametric amplifier. 1: Input pump laser beam, 2: second amplification stage (PA2) pump laser beam, 3: White light generation (WLG) beam, 4: Pre-amplifier (PA1) pump laser beam, 5: White-light. 6: Signal, 7: Optical fresh pump stage for sum-frequency generation.

The pump and signal beams are made collinear in the second nonlinear crystal leading to the generation of collinear and well-collimated signal and idler beams. Optical frequency mixers can be used at TOPAS-Prime output to extend the tuning range into visible, ultraviolet, or infrared. The pre-amplifier stage's wavelength tuning is done by delaying the white-light pulse to the first pump pulse and satisfying the phase matching condition. In the power amplifier, the wavelength tuning is carried out by first adjusting the pre-amplifier wavelength and then optimizing the second crystal angle and signal delay to the second pump beam.

#### 2.4. Femtosecond fiber laser

We also used a femtosecond fiber laser system (Satsuma HP2, Amplitude system) aircooled, a compact, diode-pumped, ultrafast fiber amplifier system delivering  $\mu J$  pulse energies in sub-500 fs pulses at high repetition rates (200 kHz to 40 MHz). Satsuma uses state-of-the-art Ytterbium-doped photonic crystal fibres as amplifying medium[7]. This type of fiber can be directly diode-pumped and offer many attractive properties providing the capability of amplifying pulses up to the multi-micro-Joule level while maintaining an excellent pulse quality. Moreover, the fiber geometry minimizes detrimental thermal effects allowing for high average power operation from rugged and simple amplifier architecture. Furthermore, the guiding properties of the truly single-mode fibers provide an excellent output beam quality. **Fig. 4** shows the optical layout of the fiber laser system (Satsuma HP2) consisting of the front end and laser head.

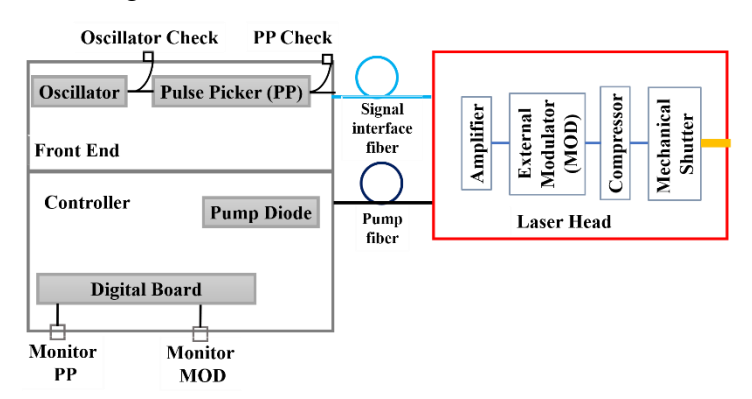


Fig. 4: The optical layout of the diode pump fiber laser system.

The front end consists of an oscillator and pulse picker (PP), and this unit is connected with the controller (shown in **Fig. 5**). The signal interface fiber optically communicates between the front end and laser head with the help of a fiber channel (FC)/ Angle polished connector. The controller consists of a pump diode and motherboard, these units are

connected with a laser head with an SMA connector. The laser head consists of an amplifier, an external modulator, and a mechanical shutter.



Fig. 5: The pictorial of diode pump fiber laser system comprised of laser head and controller.

#### 2.5. Nanosecond laser system

We also Nd:YAG (neodymium-doped used pulsed yttrium aluminum garnet; Nd:Y<sub>3</sub>Al<sub>5</sub>O<sub>12</sub>) laser for direct laser writing. The active medium is trivalent neodymium, which is optically pumped by a flash lamp whose output corresponds to principal absorption bands in the red and near-infrared [8]. Since the two ions are of comparable size, the dopant, trivalent neodymium Nd(III), typically replaces a small fraction (1%) of the yttrium ions in the host crystal structure of the yttrium aluminum garnet (YAG). The neodymium ion, just like the red chromium ion in ruby laser, offers the lasing activity in the crystal. A set of neutral density filters controls the power of the beam. Also, round, variable metallic neutral density filters precisely control the laser power. A combination of half-waveplate and polarizer controls the polarization and optical power.

#### 2.6. Field emission-scanning electron microscopy (FESEM)

At low magnifications of 10X to exceptionally high magnifications of 300 kX, FESEM gives topographical and elemental information with nearly infinite depth of field. A

scanning electron microscope's electron gun uses a field-emission cathode to produce narrower probing beams at low and high electron energy, resulting in better spatial resolution and less sample charging and damage. FESEM delivers sharper, less electrostatically distorted images with spatial resolution down to a few nanometers, almost three to six times better than conventional scanning electron microscopy (SEM) [9,10]. Energy dispersive spectroscopy (EDS) can analyze smaller-area contamination regions at electron accelerating voltages. It can produce high-quality, low-voltage images with an almost negligible electrical charging effect on the samples over accelerating voltage from 0.5 to 30 kilovolts. If needed, one can use in-lens FESEM inbuilt for taking ultrahigh-magnified images.

#### 2.7. X-Ray Diffraction Analysis

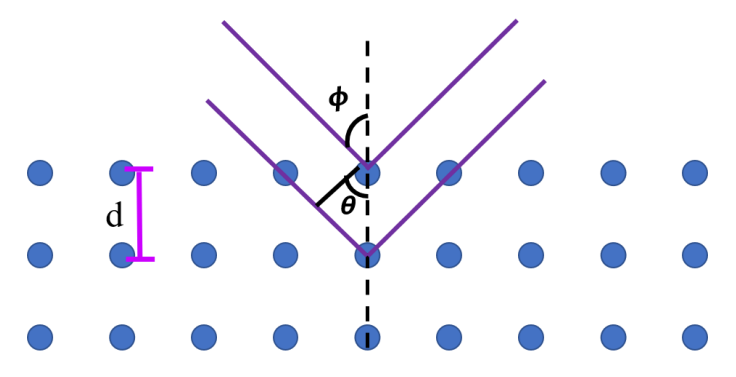


Fig. 6: Schematics of an x-ray diffractometer.

The crystallographic character of any material is investigated using X-ray diffraction. The x-ray diffraction occurs for radiation whose wavelength is close to the interplanar spacings between the atomic layer of the materials. In 1913, W. H. Brag first developed the condition of x-ray diffraction off in crystal planes [11]. The condition for x-ray diffraction to occur at the crystallographic plane is

$$2dsin\theta = n\lambda$$

where  $\theta$  is the glancing angle, d is the interplanar spacing, and  $\lambda$  is the wavelength of x-ray, and n (integer) represents the order diffraction. The schematics of Bragg diffraction conditions in crystal planes and an X-ray diffractometer are shown in **Fig. 6**. The x-ray diffractometer comprises an x-ray source, a detector, and a sample stage. A cathode-ray

tube generates the x-rays, which are made monochromatic using the slits. The detector detects the diffracted X-ray from the sample. The penetration depth of the X-ray is 50-200  $\mu$ m [12], which can be minimized by decreasing the glancing angle. The angle of incidence is decreased to a minimum value (such as  $0.5^{\circ}$ ), allowing the majority of the X-ray photons to be diffracted by the first few layers of sample.

# 2.8. Atomic Force Microscopy

Atomic force microscopy (AFM) is one of the scanning probe microscopies capable of providing surface information (surface roughness, surface profile, etc.) up to the resolution of a few nanometres. This is an excellent tool due to the employment of piezoelectric elements that facilitates tiny movement but with high precision and accuracy. The Lennard-Jonne's potential developed between two particles near the vicinity is expressed by

$$V = K\{\left(\frac{r_m}{r}\right)^{12} - 2\left(\frac{r_m}{r}\right)^6\}$$

where r is the distance between the two particles, K be the constant signifying the depth of the potential, and  $r_m$  is the distance for the least potential. This is the working principle of AFM, where interaction potential is between the tip and material surface in the vicinity. Fig. 7 shows the schematic diagram of an AFM comprises a tip (diameter~10-20 nm) mounted with

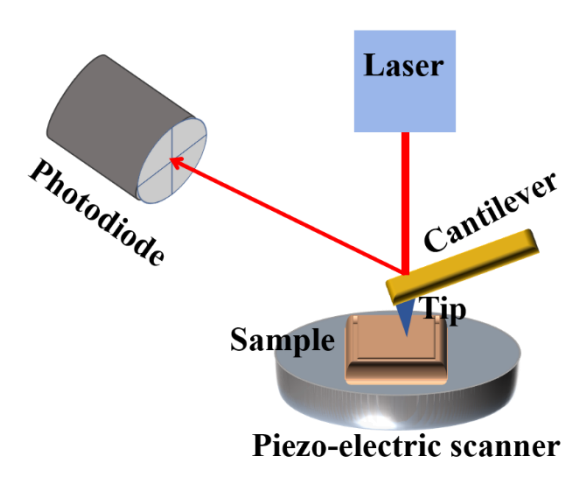


Fig. 7: Schematic of an AFM.

a cantilever [13]. A laser beam is made incident on the cantilever, and after the reflection, it is collected by the photodiode. The cantilever is scanning the material surface in a raster fashion and getting deflected depending on the surface topography of materials due to the piezoelectric movement, which reflects the laser beam collected by arrays of the photodiode. The light collected by the photodiode arrays is analyzed with computed, and a 3D image of the material surface is processed.

#### 2.9. Reflectance measurements

We have carried out the spectral reflectance measurements using a UV-vis-NIR spectrophotometer (JASCO V-670) with an absolute reflectance measurement accessory (ARN-731) [14]. The photograph and optical layout of the accessory are presented in **Fig. 8(A&B)**. This unit consists of a detector with a 60 mm diameter integrating spheres and PbS photoconductive cells. The incidence and collection angles are maintained at the same 'synchronous' angle, rotating the sample holder simultaneously and integrating the sphere. The absolute reflectance of the sample can be measured because the optical path from the center of rotation to the detector is the same as that from the sample to the detector. The ARN-731 is used to measure the absolute reflectance of a specular sample or relative reflectance of a diffusely reflecting sample's surface. The angle dependence absolute reflectance can be measured by moving the integrating sphere from 3.3° to 90° (angle of incidence).

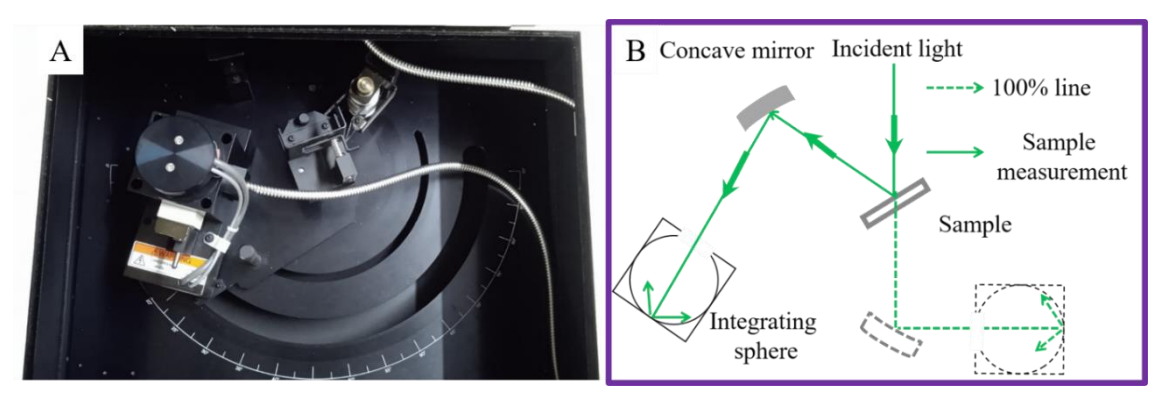


Fig. 8: (A) Photograph and (B) optical layout for the accessory (ARN-731) of UV-visible-NIR spectrophotometer (JASCO, V-670).

#### References

- [1] A. Taher, N. Chaudhary, K. Thirunaukkarasu, V.K. Rajput, S.R.G. Naraharisetty, Controlled periodicities of ladder-like structures via femtosecond laser of wavelength from 400 nm to 2200 nm, Surfaces and Interfaces. 28 (2022) 101622. https://doi.org/10.1016/j.surfin.2021.101622.
- [2] Newport, ESP300 Motion Controller / Driver User 's Manual, (2002).
- [3] Newport, Mai Tai HP User Manual, Terra. (1999).
- [4] S. Physics, Spitfire Ace Manual, (2011).
- [5] D. Strickland, G. Mourou, Compression of amplified chirped optical pulses, Opt. Commun. 56 (1985) 219–221. https://doi.org/10.1016/0030-4018(85)90120-8.
- [6] U.A.B. Mgf, K. Address, L. Rev, WinTOPAS version 3 . x External interfaces, (n.d.) 1–28.
- [7] S. Hp, Satsuma HP, 33 (n.d.) 2–3.
- [8] M. View, Quanta-Ray Lab-Series, (2003).
- [9] Zeiss, Zeiss Field Emission Scanning Electron Microscope Users Guide, (2005) all.
- $[10] \quad \text{Carl Zeiss NTS, } \Sigma \text{IGMA}^{\text{TM}} \quad \text{Field Emission Scanning Electron Microscope} \\ \quad \text{Instruction} \qquad \qquad \text{Manual,} \qquad \qquad 2011. \\ \quad \text{http://www.iitk.ac.in/meesa/SEM/tutorial/SEM\_MS.pdf.}$
- [11] P.W.H. Bragg, W.L. Bragg, Downloaded from https://royalsocietypublishing.org/ on 12 October 2021 Downloaded from https://royalsocietypublishing.org/ on 12 October 2021, 17 (1903) 428–438.
- [12] H. Yamada, R. Suryanarayanan, Calculation of the penetration depth of X-rays in intact pharmaceutical film-coated tablets by microdiffractometory, Pharm. Res. 23 (2006) 2149–2157. https://doi.org/10.1007/s11095-006-9070-x.
- [13] N. Marturi, nanocharacterization in scanning electron microscope. Thèse de Doctorat Vision and Visual Servoing for Nanomanipulation and Nanocharacterization using Scanning Electron Microscope, (2014).
- [14] Ishikawa, Spectrophotometer Hardware / Function Manual, (2006).

# Chapter 3

# The formation of simultaneous dual-scaled gratings by femtosecond laser irradiation

#### Abstract

Ladder-like laser-induced periodic surface structures (LIPSS) are engineered with femtosecond laser irradiation of wavelength from 400-2200 nm on stainless steel surfaces. These gratings comprise low spatial frequency LIPSS (LSFL) and high spatial frequency LIPSS (HSFL) simultaneously, which are orthogonally oriented to each other and resemble ladders. The periodicity of these structures is systematically controlled by varying the wavelength covering a broad range from 400 nm to 2200 nm with appropriate laser fluences. The spatial periodicity LSFL are varied from 240 nm ( $\lambda$ 1.7) to 780( $\lambda$ 4.7), whereas HSFL periodicities are tuned anywhere from 44 nm to 95 nm ( $\lambda$ 8 to  $\lambda$ 30) with the variation of incident laser wavelength. Our results show that the LSFL periodicities increase linearly with wavelengths up to 1500 nm. However, the LSFL periodicities cannot increase beyond a maximum limit at higher wavelengths, suggesting some possible constraints in forming surface plasmon mode frequencies. With wavelength variation, similar behavior is found in HSFL periodicities, indicating that the primary LSFL developments influence the embedded HSFL periodicities.

#### 3.1. Introduction

Controlled manufacturing of nanostructures having various length scales and surface topography morphologies is significant in all fields of science and industry [1–3]. This can be accomplished with various high-precision lithography techniques, but these systems are complex, expensive, and inflexible. Fabricating subwavelength surface structures with high-power pulsed lasers is attractive to scientists because it enables single-step processing, resolutions beyond the diffraction limit and is reliable and scalable to industry standards. The formation of the subwavelength laser-induced periodic surface structures (LIPSS) under the influence of the laser pulses is universally observed on several materials[4–8]. The recent emergence of this field is observed from several applications exploiting the generation of LIPSS[9]. To name a few of the applications using LIPSS are fabricating optical sensors[10], controlling wetting properties[3,11,12], the colouring of surfaces[13–15], tribology[16,17], printable nanogratings[6,18,19], polarizing optical elements[20], anti-reflectivity properties[7,21,22], medical and biological applications[1,9], etc.

Several researchers did detailed and systemic studies on the formation and morphology of LIPSS on metals[7,23], dielectrics[24–26], polymers[27], and semiconductors[28,29]. These LIPSSs are ripple-like structures formed as parallel periodic lines on the material's surface subjected to laser ablation. The periodic structures are spontaneously formed on the surfaces, and their periodicity is observed from a few hundred nanometres to micron size in different experimental conditions[3]. The LIPSS formation is influenced by the surface's material properties and incident electromagnetic radiation properties. On a given substrate, the formation of LIPSS can be changed typically by fluence or size of the beam, scanning rate or repetition rate, state of polarization, irradiation wavelength, and surrounding environment.

The ultrashort plane-polarized laser generates primarily two classes of LIPSS upon interaction with the materials: low spatial frequency LIPSS (LSFL) and high spatial frequency LIPSS (HSFL) [30–33]. LSFL has a larger spatial periodicity, and its periodicity can vary between incident laser wavelength and half of the wavelength

depending on the type of material[34]. In almost every material, LSFL formed orthogonal to incident beam polarization, and their periodicity can be controlled with fluence variation [35,36]. Based on their spatial periodicity and orientation to the incident beam polarisation, the LSFL are further subdivided into LSFL-I and LSFL-II. The LSFL-I spatial periodicity is closed the incident beam wavelength ( $\Lambda \sim \lambda$ ), oriented orthogonal to the beam polarization, and primarily formed in metallic and semiconductor materials. The LSFL-II is generally formed on large bandgap materials, oriented parallel to the laser beam polarization, and periodicity is an order of  $\Lambda \sim \lambda / n$ , where n is the refractive index of the material used. Also, these LSFL are further classified as Type-s, Type-d and Type-2s. In the current work, the LSFL formed on the SS surface may be categorized as Type-2s. HSFL can be two types depending upon the depth to period aspect ratio (A), HSFL-II if A>1 and HSFL-II if A<1 [37].

The generation of the LSFL is explained by the well-established idea of interference between the coherent incident laser light and the surface scattered wave. The surface transformation in multi-pulse irradiation is driven by scattered electric field superposition with the incoming next pulse, yielding a feedback mechanism, which is crucial for fabricating LIPSS over a large area[38]. Other ideas, such as surface plasmon polaritons, re-organization matter, can explain the origin of LIPSS [37]. According to a generally accepted concept, the surface plasmon polariton (SPP) is considered to play a crucial role in the formation of LSFL. Incoming electromagnetic fields can be associated with the oscillations of the electron-plasma at the dielectric and conductor interface, resulting in highly confined surface electromagnetic waves known as surface plasmons. These surface waves could be critical for the initial polarization dependence of the LIPSS and further enhanced by the feedback mechanism. The formation mechanism of these HSFL is unclear; some concepts suggest that HSFL forms from electromagnetic theory will be mostly parallel to the polarisation [37]. Few mechanisms are based on self-organization and surface instabilities[3,39]. A complete review of all the theories for the formation of LIPSS is presented by Jorn Bonse and Stephan Gräf [37]. There are two alternative views for the origin of LIPSS: electromagnetic impacts or material reorganizations. More experimental exploration is needed in this regard to gain more insight. There were no solid experimental works devoted to unraveling the LIPSS formation over a broad wavelength range of 400 nm to 2200 nm that we could find. The influence of laser wavelength on any given material can provide more understanding of the underlying mechanisms. We fabricated a special type of LIPSS called ladder-like structures for each wavelength on stainless steel surfaces. These LIPSS are reported earlier in the literature as dual-scale structures, double frequency LSFL where the HSFL are embedded inside the larger periodicity LSFL [40–42]. We could manipulate these LSFL structures over a large area of SS surface for several industrial applications. Our interesting results suggest LSFL are indeed dependent on the incident wavelength, and HSFL formed in-between the LSFL structures show the dependency on the primary LSFL formations.

# 3.2. Experimental procedure

A commercial Ti: Sapphire femtosecond laser (Spectra-Physics) generates laser pulses with a central wavelength of 800 nm, a pulse width of 75 fs, energy of 6mJ per pulse and repetition rate of 1000 Hz. Amplifier output of 3 mJ pulse is used to pump optical parametric amplifier (TOPAS Prime, Light Conversion) to tune the fundamental wavelength (800 nm) of laser beam anywhere in the spectrum from 400nm-2200 nm.

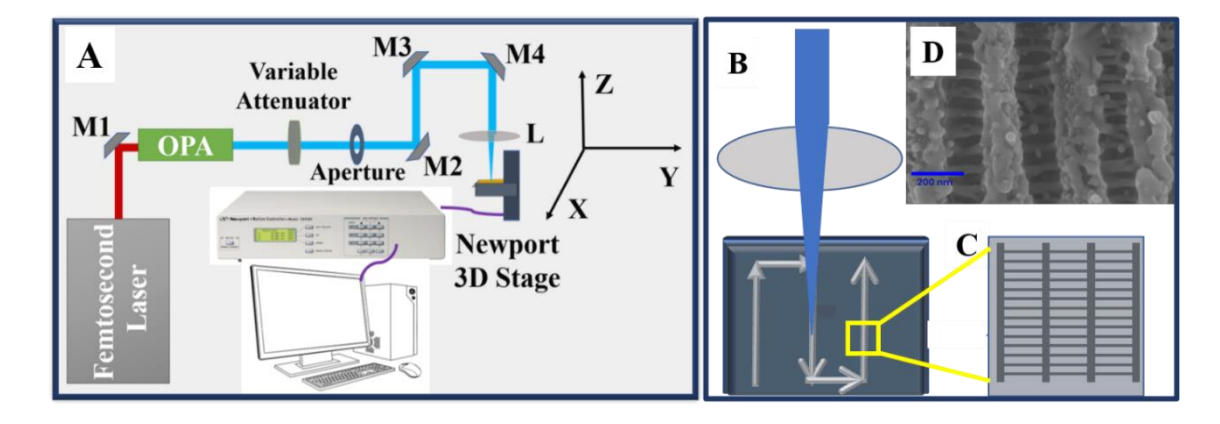


Fig. 1. The schematic of (A) experimental set-up and (B-D) flowchart of formation of LIPSS. OPA: optical parametric amplifier; M: mirrors; L: Convex lens, 3D stages: three-axis stages. (B): focused beam irradiated the surface in raster scanning and imprinted the combined ladder structures containing HSFL and LSFL. (C) Represents the scheme of structures formed inside the laser written line. These lines are

separated, and there is no overlap between the adjacent laser lines. (D) Dual-scaled gratings formation on SS.

A high extinction ratio polarizer is utilized to remove unwanted wavelengths and select the wavelength what the experiment requires. The spectral purity for each wavelength is ensured over the entire range by using appropriate spectrometers. The laser beam was focused with a convex lens of 5 cm focal length (calcium fluoride) for precise nanostructuring. For each specified central wavelength, laser irradiation is done for nanostructuring the surfaces from below ablation threshold fluence to maximum available fluence. The substrates were mounted on the three-dimensional stages (Newport, ESP motion controller, 1µm resolution) controlled by a LabVIEW program. For optimization, substrates were translated with four different scanning speeds 1mm/s, 0.5 mm/s, 0.2 mm/s, and 0.05 mm/s for each incident wavelength. Fig. 1(A) shows the schematic of laser direct writing set-up and fabrication scheme of the laser-induced surface structures on the stainless-steel surfaces. Fig. 1(B) shows the laser scanning mechanism. Fig. 1(C) & D) shows the fabrication of ladder-type structures schematic and experimental result. These structures are very similar to the original butterfly scales in the black region [43]. The surface morphologies are characterized with Field Emission Scanning Electron Microscope (FESEM), and spatial periodicities of LSFL and HSFL are obtained from these images. We analyzed the spatial periodicity of laser-irradiated surfaces on FESEM images using image-J software.

#### 3.3. Results and discussions

#### 3.3.1. Effect of incident laser fluence on LIPSS

The spatial periodicity of LIPSS is regulated by employing several experimental conditions such as laser fluence[44], the number of pulses per spot[45], scanning speed[7], incident wavelength[6], angle of incidence[46], the shape of the beam[47–49], repetition rate[50], etc. This section outlines how laser fluence influences the microstructures and spatial periodicities of LSFL and HSFL. For simplicity, only three wavelengths of 600, 1200, and 1700 nm at a constant scanning speed of 0.2 mm/s are shown for variation in spatial periodicity with fluence.

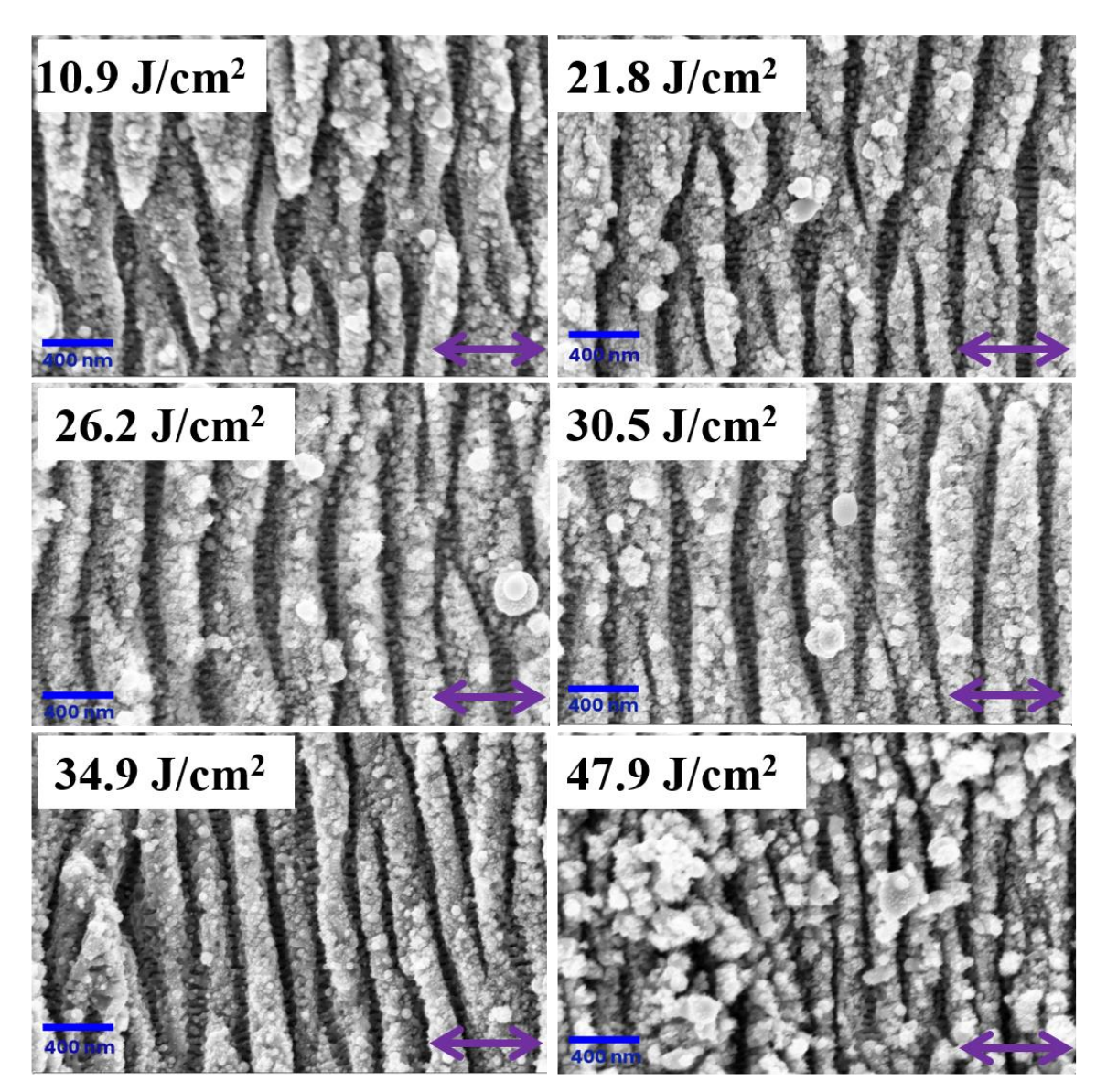


Fig. 2. Variation in LIPSS formation with the incident laser fluence for the incident wavelength of 600 nm, number of pulses of 38, at a scanning speed of 0.2 mm/s, and a repetition rate of 1 kHz. Fluence for each FESEM picture is indicated on the top corner of the pictures. At lower wavelengths, the HSFL are not visible in these FESEM pictures. However, when we go to higher wavelengths, the HSFL appears in the FESEM pictures with the same resolution (100 kX).

**Fig. 2** shows the variation of LIPSS formation with the laser incident wavelength of 600 nm for different incident fluences. The spatial periodicity of LSFL is slightly varying with the laser fluence. Upon further investigation at high resolution, one can observe the formation of the well-distinguished HSFL embedded inside the LSFL only for particular energies; these structures are distorted or destroyed at either higher or lower energies.

These HSFL are orthogonally oriented to the primary LSFL structures, parallel to the incident polarization. An example of these structures is shown in **Fig. 1(D)** with its schematic representation in **Fig. 1(C)**, as these structures appear like a series of ladders, referred to as ladder structures (LS).

The spatial periodicity of HSFL almost remained constant for the energies where they are forming as well distinguished structures, as shown in **Fig. 2**. With the increase in fluence from 34.9 J/cm<sup>2</sup> to 47.9 J/cm<sup>2</sup>, HSFL get distorted, and they are not forming uniformly everywhere. As the incident fluence increases, the LIPSS structures and spatial periodicity become more and more regular and smooth up to 26.2 J/cm<sup>2</sup>, and with a further increase, they degrade. Very clear and prominent LSFL and embedded HSFL are forming at a small range of fluences. At a laser fluence of 26.2 J/cm<sup>2</sup>, clear ladder structures are formed with LSFL and HSFL periodicity of 374±14 nm and 52±4.5 nm, respectively.

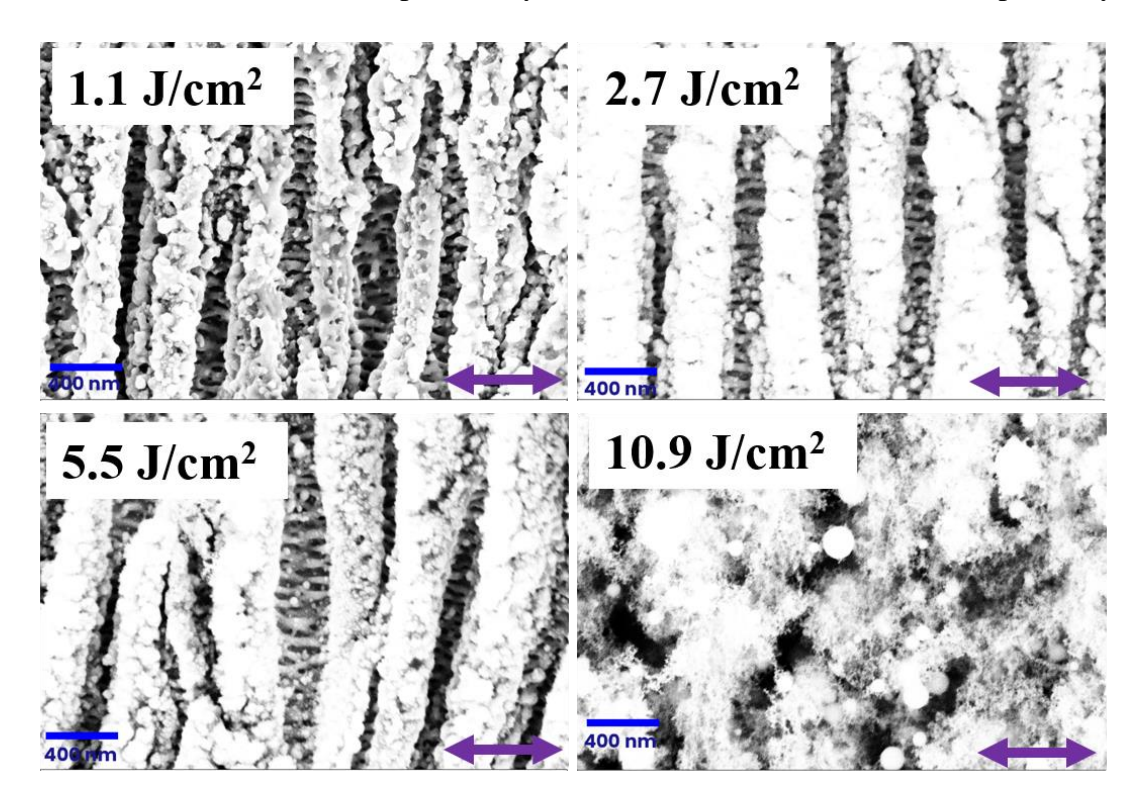
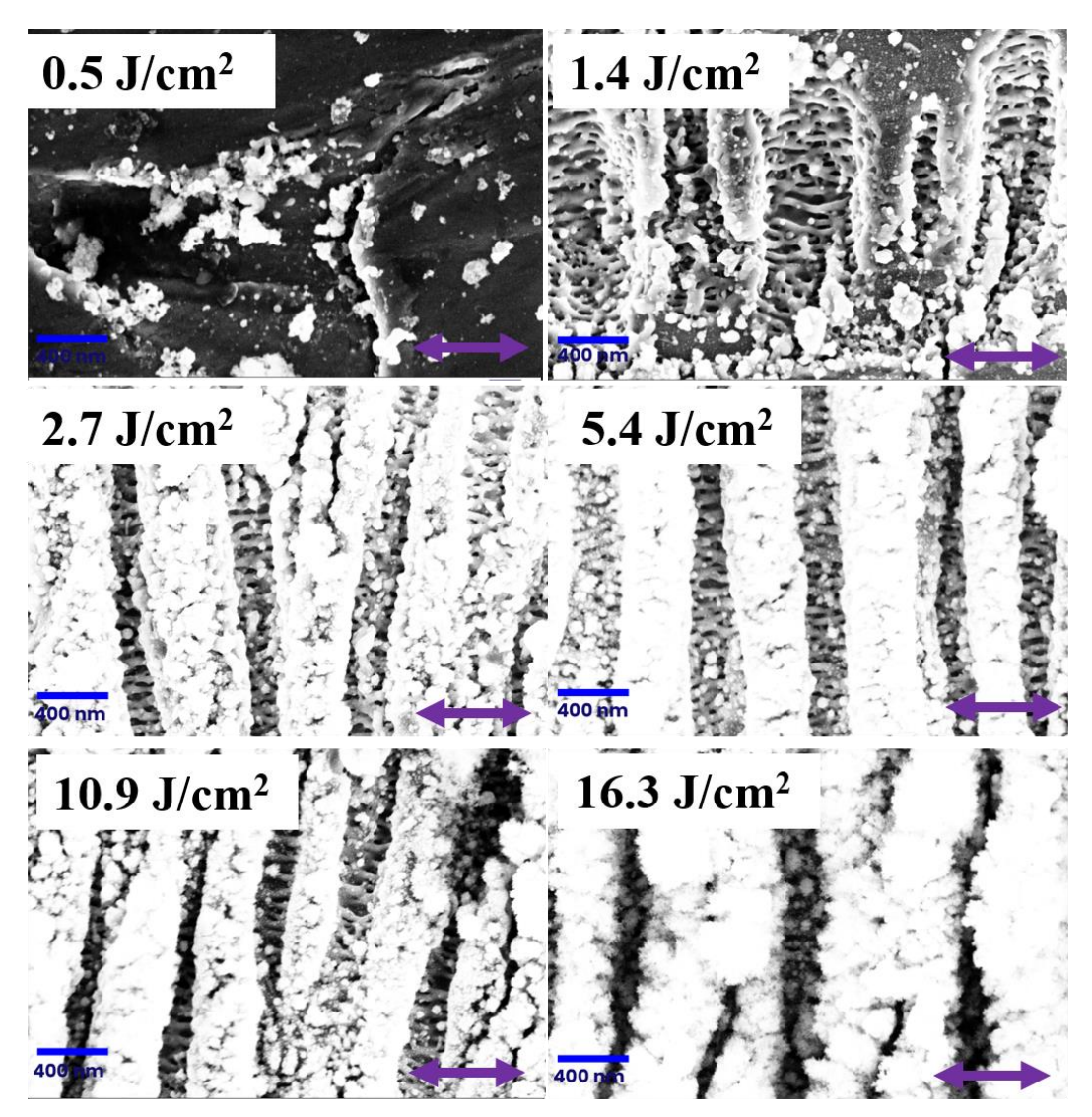


Fig. 3. Variation in LIPSS formation with the incident laser fluence for the incident wavelength of 1200 nm, number of pulses of 96, at a scanning speed of 0.2 mm/s, and a repetition rate of 1 kHz.



*Fig. 4.* Variation in LIPSS formation with the incident laser fluence for the incident wavelength of 1700 nm, number of pulses of 108, at a scanning speed of 0.2 mm/s, and a repetition rate of 1 kHz.

Similar variations are observed when the laser output is tuned to 1200 nm, where we get substantial energy from OPA. **Fig. 3** shows the FESEM images of stainless-steel surfaces irradiated at 1200 nm wavelength for a fixed scan speed of 0.2 mm/s for different incident fluences as indicated on each image. The LSFL and HSFL features started to form at 1.1 J/cm<sup>2</sup> incident laser fluence; as the fluence increased, the best ladder structures were formed at 2.7 J/cm<sup>2</sup>. As we further increase the energy, LIPSS are getting distorted, and these ladder structures are getting destroyed after 5.5 J/cm<sup>2</sup>. At 10.9 J/cm<sup>2</sup> fluence, LSFL structures are entirely degraded. At the optimal laser fluence of 2.7 J/cm<sup>2</sup>, clear ladder

structures are formed everywhere with LSFL periodicity 508±8 nm and HSFL periodicity 80±3.6 nm.

When the incident wavelength is tuned at a higher wavelength of 1700 nm, the energy output from OPA is not sufficient to destruct LIPSS. FESEM images of LIPSS formations are shown in **Fig. 4** for different incident fluences. At 0.5 J/cm², the surface just scratched very little, and this fluence is too low to interact with the surface. At 1.4 J/cm², the surface got ablated but insufficient to produce a good combination of LSFL and HSFL. From this picture, it is clear that even before the formation of LSFL, the HSFL are forming very well. Compared with **Fig. 2** with a 100 nm scale bar, the HSFL features are visible in **Fig. 4**, where the scale bar is 200nm. When the driving force is at higher wavelengths, the LIPSS formation periodicities are also higher. With increased incident fluence from 1.4 J/cm², the ladder structures get better and better until a fluence of 5.4 J/cm². Further increase in fluence, the combined structure of LSFL and HSFL start distorted or randomizing. The best fluence at which the ladder structures are formed is 5.4 J/cm², and the periodicity of LSFL is 612±18.4 nm with an embedded HSFL periodicity of 75±12 nm.

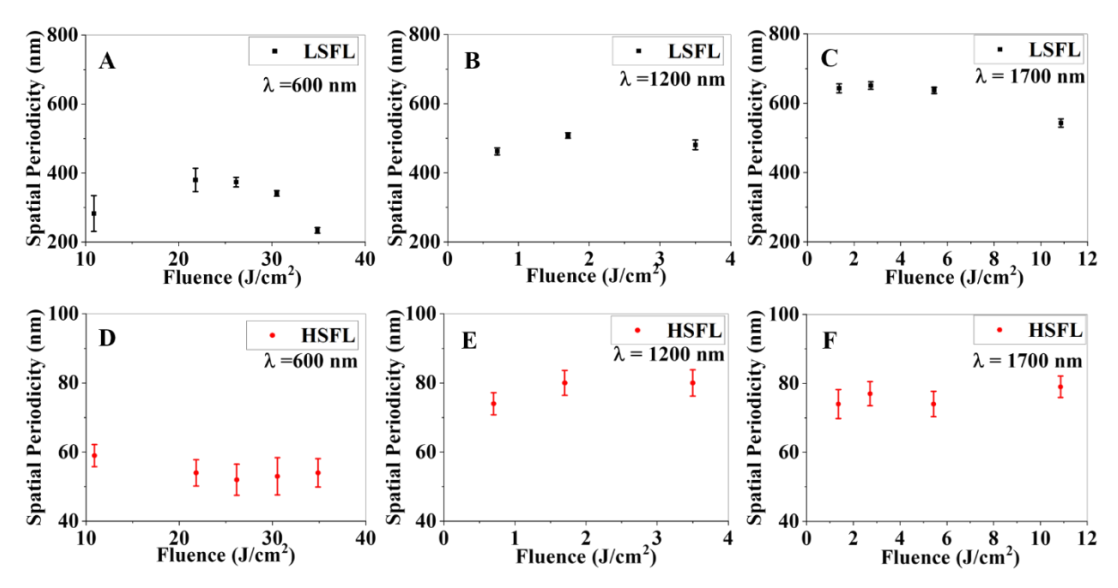


Fig. 5. Effect of fluences on LSFL and HSFL periodicities for three different incident wavelengths. The graphs in the upper row show the variation of LSFL periodicities in (A) for 600 nm, (B) for 1200 nm, and (c) for 1700 nm. Similarly, the variation of HSFL periodicities is shown by the graphs in the upper row in (A) for 600 nm, (B) for 1200 nm, and (c) for 1700 nm.

The summary of fluence variation for these three wavelengths is presented in Fig. 5. The LSFL and HSFL periodicity variations with fluence and wavelength can be seen from these three graphs, and the corresponding FESEM images are shown in Fig. (2-4). Our experiments demonstrate that for good LIPSS structure formation, it is essential to optimize the incident laser fluence for each wavelength. The HSFL periodicities are almost independent of incident laser fluence. Even though the LSFL periodicities vary, the well-defined LSFL and embedded HSFL form only at a particular fluence or very small fluence range. This allows us to systematically study the variation of LIPSS with different incident wavelengths by optimizing the energy for each wavelength to form ladder structures.

# 3.3.2. The optimal laser fluence for formation threshold, Ladder structures, and destruction of LIPSS

As observed in the above section, the material surfaces interact with incident electromagnetic waves differently with the incident laser beam[51]. The same primary analysis is done for all the wavelengths from 400 nm to 2200 nm. The formation threshold of LIPSS, fluence needed for ladder structures, and maximum incident fluence at which LIPSS structures could withstand are studied in detail for each wavelength. The summary of this analysis is shown in Fig. 6. As these parameters change with different incident wavelengths, a careful study is carried out to investigate the range of fluence over which the best possible ladder structures are formed. The best possible ladder structure is the formation of clear and smooth HSFL structures embedded in LSFL structures. We noticed that the formation threshold is low for most of the incident wavelengths within the fluence range of 0.8-25.1 J/cm<sup>2</sup> and keeps varying depending upon the incident wavelength, as shown in Fig. 6. The ablation threshold of the material's surface is the minimum fluence of irradiation needed to ablate the surface, and the surface starts interacting with the irradiated focused laser beam [52–54]. The LIPSS formation threshold is the energy required to form LIPSS. The fluence of the incident-focused laser at which the best possible combination of LSFL and HSFL start forming is defined as the optimal energy for ladder structures (optimal fluence for LS). These optimal fluences for LS are

a small range of incident fluences, and our reported energies are approximate values. We did not use several small step fluence variations over the entire range; however, we took fluence points on either side of the optimal energies. Finally, the destruction energy is the laser fluence at which the LIPSS starts to disintegrate, become random, or form irregular shapes. The summary of all these systematic studies is presented in **Fig. 6**. Note fluence generally decreases with the increase in wavelength as focal spot size increases with wavelength.

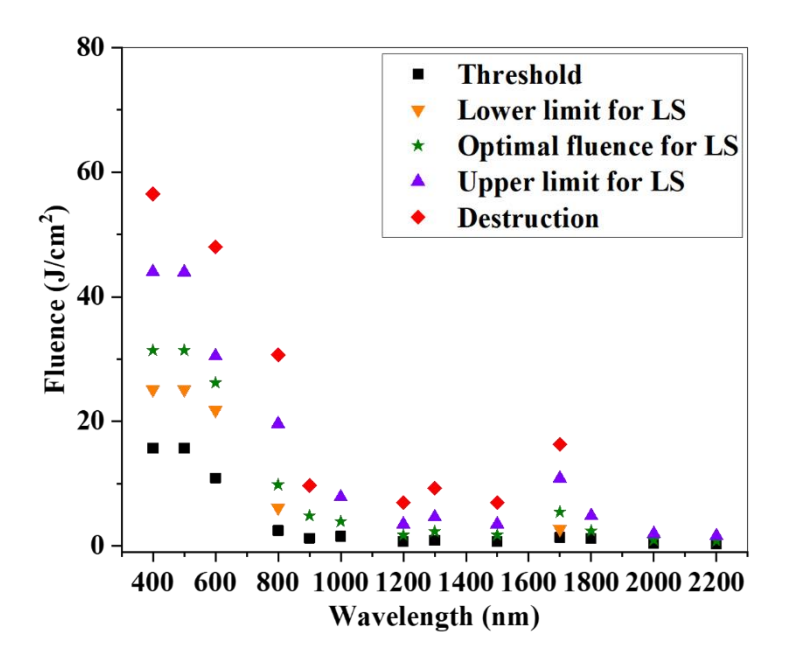


Fig. 6. The incident laser fluence required for the threshold of LIPSS formation, the lower limit of the ladder structure formation (LS), and optimal energy required for the formation of the best ladder structures uniformly everywhere, an upper limit to see the LS and the LIPSS destruction energy as obtained for each wavelength.

#### 3.3.3. Systematic modulation of the LIPSS with the incident wavelengths

The polished stainless-steel surfaces respond differently with each wavelength of a laser beam. The absorptivity of the different incident wavelengths is significantly different, and the interaction mechanism depends upon this property[22]. The precise control of spatial periodicity and their orientations is the most challenging aspect of the LIPSS. We showed this could be manipulated using incident wavelengths, which is evident from the previous sections describing LIPSS periodicity for three different incident wavelengths. Here, the effect of incidents wavelength over 400-2200 nm is discussed. The Optical Parametric

Amplifier generates this broad range of laser beams from the fundamental wavelength 800 nm. **Fig. 7** shows the FESEM pictures, surface morphologies describing spatial periodicity of ladder structure LIPSS using different incident wavelengths irradiated with a fixed scanning speed of 0.2 mm/s. All the images are obtained when ablated with the optimal fluences to form ladder structures. These optimal fluences and their corresponding HSFL and LSFL periodicities are shown in **Table 1**. **Fig. 7**, the magnification of each image is 100 kX, and the double arrows represent the incident beam polarization for each wavelength. The orientations of LSFL are always perpendicular to the incident polarization, and the LIPSS orientations can be changed according to the beam polarization. However, embedded HSFL forms perpendicular to LSFL orientations but parallel to the beam polarization; these ripples lie deep inside the grooves of the LSFL LIPSS. The orientations of LSFL and HSFL are attributed to the electromagnetic origin as reported in the literature[7,36,37]. The origin of HSFL periodicities is reported due to the harmonics of the incident wavelength[5,6,24,42].

**Table 1**. Spatial periodicity of LSFL (Type-2s) and HSFL measured from FESEM images over the broad incident wavelengths 400-2200 nm and their corresponding ratios to the incident wavelengths.

Incident wavelength(λ) nm	Pulse width (fs)	Optimal fluence for LS (J/cm²)	Alsfl nm	Ahsfl nm	λ∕Λlsfl	λ/Λ <sub>HSFL</sub>
400	83	31.4±5.4	238±26.6	45±6	1.68	8.88
500	73	31.4±5.2	304±39.4	44±4.4	1.64	11.36
600	70	26.2±2.5	316±58.9	52±7.6	1.90	11.54
800	83	9.8±1.0	322±14.3	59±6.1	2.48	13.56
900	70	4.9±0.9	323±39.5	61±8.1	2.79	14.75
1000	67	3.9±0.8	399±46.2	63±7.7	2.50	15.87
1200	75	2.7±0.3	530±36.5	79±11	2.26	15.19
1300	86	2.3±0.15	541±68	73±9.5	2.40	17.81
1500	77	17.4±0.07	577±60	89±8.9	2.60	16.85
1700	86	5.4±1.5	612±18.4	75±12	2.78	22.67
1800	91	2.4±1.2	776±53.9	94±13.7	2.32	19.15
2000	93	2.0±0.01	760±50	82±8.6	2.63	24.39
2200	88	0.8±0.02	466±28	74±7.6	4.72	29.73

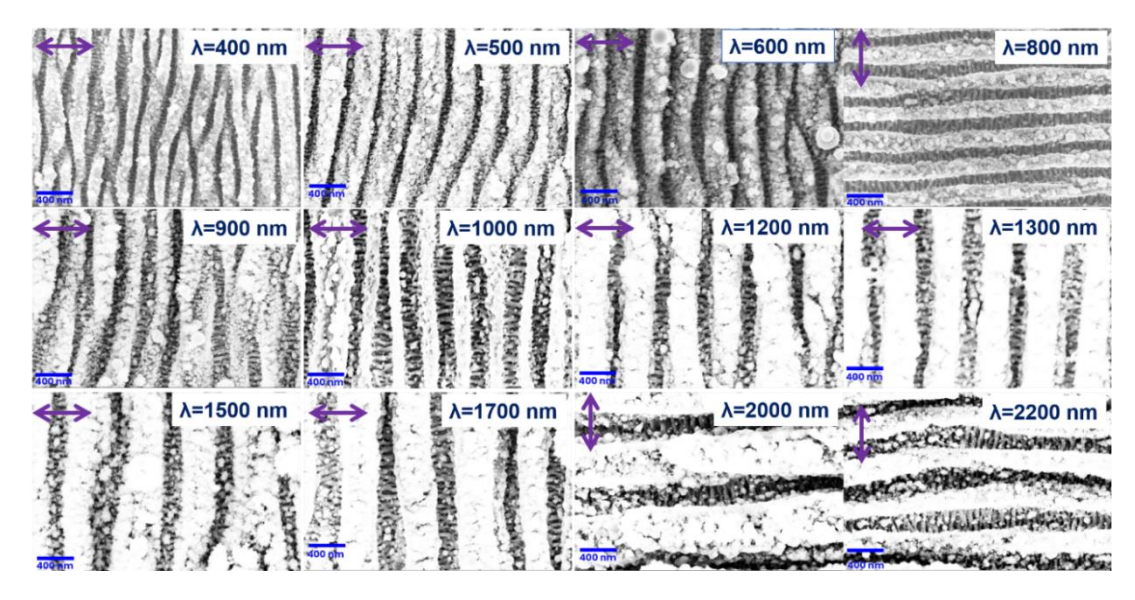


Fig. 7. Surface morphologies of the ladder structure of the stainless-steel surface with different incident wavelengths at a constant scanning speed of 0.2 mm/s. These images are for those fluences where the best possible ladder structures are formed.

**Fig. 7** and **Table 1** indicate that the spatial periodicity of LSFL increases as the incident wavelength increases up to a particular wavelength and then decreases with a further increase of wavelength. Spatial periodicity becomes highest at 1800 nm, and upon a further increase in wavelength, the spatial periodicity starts decreasing. The behavior of LSFL and HSFL will be discussed in detail in the following section.

#### 3.3.4. Effect of periodicity with wavelength for the best ladder-like structures

The periodicities of LSFL and HSFL are discussed in this, and the following sections correspond to the optimal fluences for the best ladder-like structures. One must remember that optimal structures are produced at different fluences and the number of pulses per spot for each wavelength. Controlling or engineering the required spatial periodicity of LIPSS using different incident wavelengths is demonstrated in **Fig. 7** and **Table 1**. In this section, the effect of different incident wavelengths on spatial periodicity on both LSFL and HSFL for optimal ladder structures is analyzed in detail. **Fig. 8(A &B)** show the variation of spatial periodicity of LSFL and HSFL with changing incident wavelength from 400 nm to 2200 nm. The variation of spatial periodicities of LSFL with the incident wavelength is not a linearly dependent function throughout the entire range of the incident

wavelength. The spatial periodicity of LSFL increases almost in a linear fashion in the spectral range of 400 nm to 1800 nm; it may have a specific slope for the SS material. The experimental results suggest that an upper limit of LIPSS spatial periodicity exists at the incident wavelength of 1800 nm. Beyond 1800 nm, the LSFL periodicity is decreased slightly at 2000nm, whereas at 2200 nm, the periodicity decreased almost by half, as shown in **Fig. 8(A)**. The current existing theories for the LIPSS formation do not suggest this experimentally observed behavior. In the literature, it is commonly referred to that the surface plasmons play a critical role in forming LSFL [55,56]. The surface plasmon has resonance frequency and spatial length limit[57]. When the incident laser wavelength is larger at 2200nm, the experiments suggest that it is not easy to drive the surface plasmon modes with a larger scale of length. Instead, some smaller spatial modes are sustained in the material at this wavelength.

For further understanding, the ratio of the incident wavelength ( $\lambda$ ) to the measured LSFL periodicity ( $\Lambda_{LSFL}$ ) is presented in the fifth column of **Table 1** and its corresponding plot in **Fig. 8(C)**. These figures show that the ratio ( $\lambda/\Lambda_{LSFL}$ ) reaches the limit at 1000 nm, and after that, this ratio remained constant between 2.5 and 2.75, considering the experimental errors. At the incident wavelength of 2200 nm, the ratio ( $\lambda/\Lambda_{LSFL}$ ) reaches 4.72 compared to 2.6 (at 2000 nm), suggesting some harmonics of incident wavelength might be involved in driving the natural surface plasmon modes. The literature cites that the LSFL periodicities generally vary between  $\lambda > \Lambda_{LSFL} > \lambda/2$ , where most experiments are done below the 1000 nm wavelength[7,58]. Our experiment suggests that this ratio at higher wavelengths (up to 2000 nm) can be larger between 2.5 to 2.75. Further, this ratio reached even higher to 4.72 for 2200nm. The experimental data of LSFL periodicity is fitted with linear regression up to 1500 nm, R<sup>2</sup> regression coefficient of this fitting is 0.95 with a slope of ~ 0.31 (periodicity variation to wavelength). From these slope values, one can tune the laser wavelength to fabricate the LSFL periodicities anywhere in the range of 240 nm to 780 nm on a SS surface by optimizing the fluence.

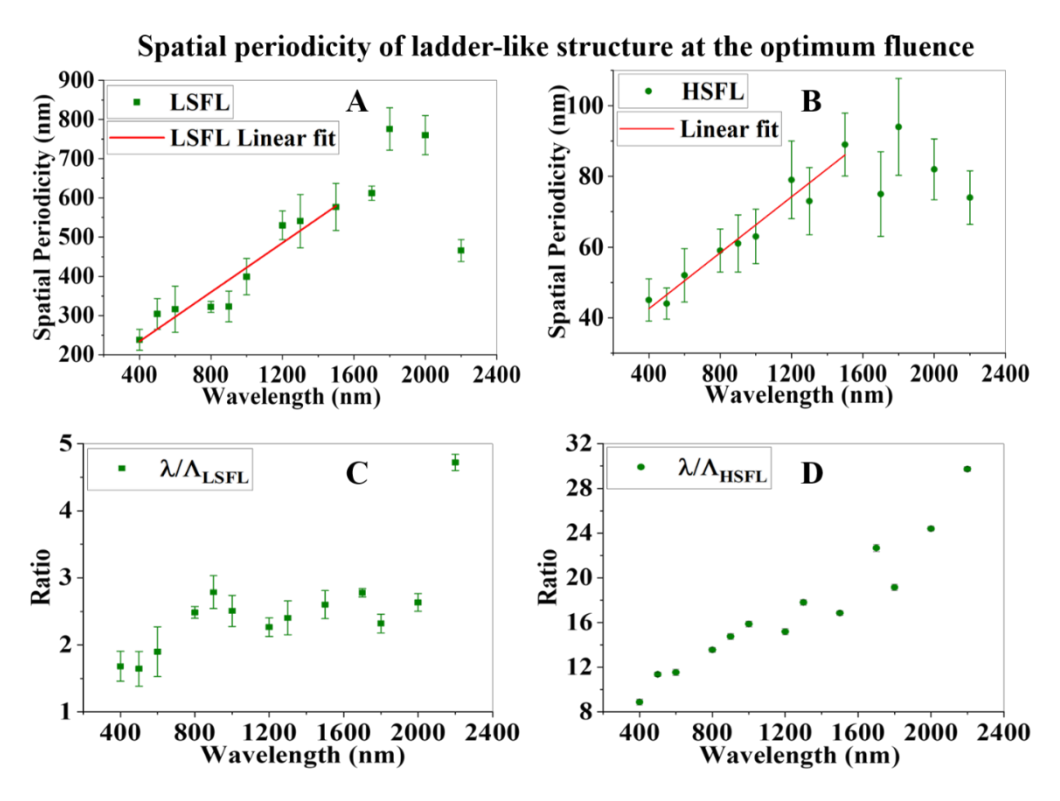
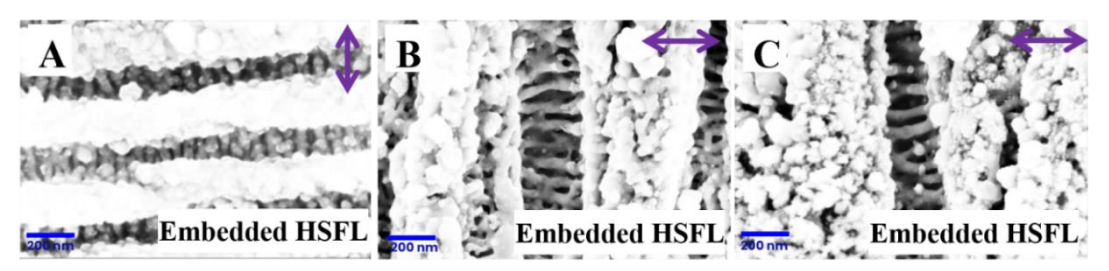


Fig. 8. Variations in spatial periodicity of (A) LSFL and (B) HSFL at optimal fluences with the incident wavelengths. The red line is the linear fit to the experimental values up to specific wavelengths. Fig. 8(C) and Fig. 8(D) show the ratio of incident wavelength to the spatial periodicity of LSFL and HSFL, respectively.

# 3.3.5. The behavior of HSFL periodicities with incident wavelengths for optimal ladder structures

The formation mechanism and behavior of HSFL are contrasting compared to LSFL in many ways, such as orientation, spatial periodicity, the linewidth of HSFL ridges, formed deep inside the grooves, response to the incident laser fluence and wavelength. The HSFL starts forming at the lower values of the incident fluence and destroys at a higher fluence. The combination of LSFL and embedded HSFL form like a ladder shape, and the high-resolution ladder structures are shown in **Fig. 9** for three different incident wavelengths. The spatial periodicity of these embedded HSFL varies from 44 nm to a maximum of 95 nm. The HSFL periodicity also increases linearly with increasing incident wavelength up to 1800 nm of incident wavelength and again decreased after a further increase in incident wavelength, which is evident when we compare the plots of **Fig. 8(A&B)**. This high correlation of these HSFL periodicity patterns with LSFL primary structures suggests that they are mainly dependent on the primary structures created by LSFL. The ratio of the incident wavelength ( $\lambda$ ) to the measured HSFL periodicity ( $\Lambda_{HSFL}$ ) is presented in the sixth column of **Table 1** and its corresponding plot in **Fig. 8(D)**. This periodicity ratio ( $\lambda$ 

/AHSFL) varies from 9 to 30, and these ratios do not show any peculiar points. The HSFL periodicity data in **Fig. 8(B)** is fitted with a linear equation up to 1500 nm; the R<sup>2</sup> regression coefficient of this fit is 0.95, and the slope is 0.04, which is one order slower than LSFL spatial periodicity gradient. The physical origin for the formation of the HSFL is well debated in the literature[37], such as the re-organization effect, harmonics of incident wavelength produced on the top of the surface, etc. Our experimental studies suggest that HSFL periodicities may depend on the primary LSFL structures rather than the incident wavelength.



*Fig. 9.* Shows the formation of Embedded HSFL between the two LSFL, which look like a ladder structure. HSFL formed with the incident wavelengths of 800 nm (A), 1200 nm (B), and 1500 nm(C).

#### 3.3.6. Upper limit of LSFL periodicity

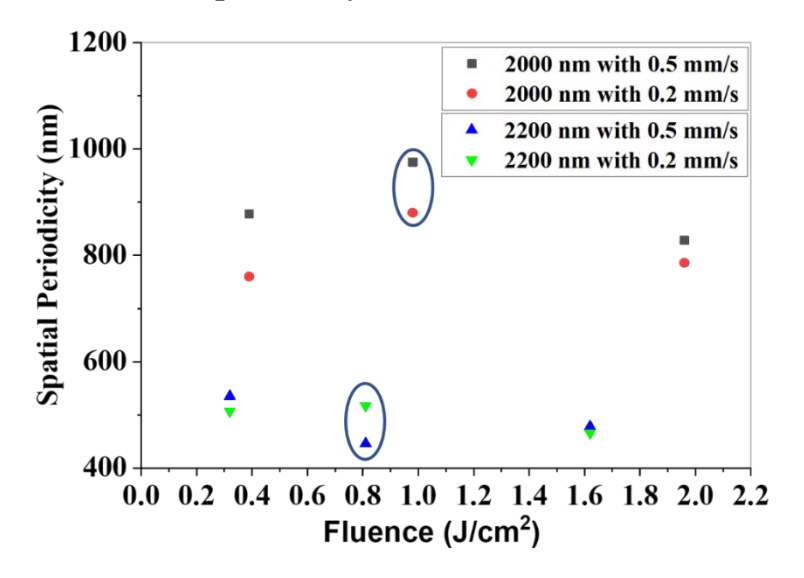


Fig. 10. The behavior of LSFL periodicity at the higher incident wavelengths. Spatial periodicity vs incident fluence for scanning speeds of 0.5 mm/s (red circle) and 0.2 mm/s (blue triangle) at the incident wavelength of (Left) 2000 nm and (Middle) 2200 nm. Spatial periodicity vs incident fluence for the scanning speed of 0.2 mm/s for two incident wavelengths, 2000 nm, and 2200 nm. Only the circled ones are optimal fluence values.

This section discusses the abnormal changes of LSFL spatial periodicity for the incident wavelength of 2000-2200 nm. It is noticed that the spatial periodicity of LSFL decreases

to 466 nm, from 760 nm. This abrupt decrease in spatial periodicity of LSFL seems to be a puzzle and beyond our expectations. The comparative study of LSFL behavior between two incident wavelengths (2000 and 2200 nm) with two different scan speeds (0.5 and 0.2 mm/s) and varying fluences is carried out to understand the behavior of spatial periodicity of LSFL. These experiments are further performed only to confirm this abrupt behavior. The outcome of these experiments is shown in **Fig. 10**. The spatial periodicity for 2200 nm is less than 2000 nm for both scanning speeds and different incident fluences. These experiments give confidence that there is an upper limit for forming the LIPSS periodicity for a given material. Further theoretical and experimental studies on different materials are needed to understand the physics behind the formation of LSFL-LIPSS and the upper limit of periodicities.

#### 3.4. Conclusion

Unique ladder types of LIPSS are fabricated on a stainless-steel surface by irradiating with femtosecond laser pulses over a broad range of wavelengths from 400-2200 nm. We could systematically control the periodicity of LSFL and HSFL by using the different incident wavelengths. The energy optimization for the LIPSS formation threshold, range of ladder structure formation, and destruction of LIPSS are presented for each wavelength. These experiments pave a path to engineering the LSFL periodicity anywhere between ~250 nm to ~800 nm on a SS surface. Also, we could control the HSFL periodicities from ~45 nm to ~90 nm. The literature suggests that LSFL periodicities vary linearly only at smaller wavelengths and periodicity  $\Lambda < \lambda/2$ . For the first time, we have shown the upper limit for the formation of the LSFL periodicity with the increase in wavelength on SS substrates, ~1800 nm. We observed the LSFL periodicities decrease with further increase in wavelength and can reach as low as  $\lambda/4.7$ . The formation of embedded HSFL is purely dependent on the primary pattern of LSFL. We observed it might not be related to the harmonics of the incident wavelength. We printed these ladderlike structures on a large area by iterative scanning as proof of principle. We showed these surfaces have remarkable properties of superhydrophobicity and antireflection properties

as examples. We demonstrated the controlled fabrication of nanostructures, which will have many applications in science and industry.

#### References

- [1] F.A. Müller, C. Kunz, S. Gräf, Bio-inspired functional surfaces based on laser-induced periodic surface structures, Materials (Basel). 9 (2016)476. https://doi.org/10.3390/ma9060476.
- [2] E. Stratakis, J. Bonse, J. Heitz, J. Siegel, G.D. Tsibidis, E. Skoulas, A. Papadopoulos, A. Mimidis, A.C. Joel, P. Comanns, J. Krüger, C. Florian, Y. Fuentes-Edfuf, J. Solis, W. Baumgartner, Laser engineering of biomimetic surfaces, Mater. Sci. Eng. R Reports. 141 (2020) 100562. https://doi.org/10.1016/j.mser.2020.100562.
- [3] R. Stoian, J. Colombier, Advances in ultrafast laser structuring of materials at the nanoscale, 9 (2020) 4665–4688.
- [4] S. Höhm, A. Rosenfeld, J. Krüger, J. Bonse, Laser-induced periodic surface structures on zinc oxide crystals upon two-colour femtosecond double-pulse irradiation, Phys. Scr. 92 (2017) 034003. https://doi.org/10.1088/1402-4896/aa5578.
- [5] R. Le Harzic, D. Dörr, D. Sauer, M. Neumeier, M. Epple, H. Zimmermann, F. Stracke, Large-area, uniform, high-spatial-frequency ripples generated on silicon using a nanojoule-femtosecond laser at high repetition rate, Opt. Lett. 36 (2011) 229. https://doi.org/10.1364/ol.36.000229.
- [6] T.Q. Jia, H.X. Chen, M. Huang, F.L. Zhao, J.R. Qiu, R.X. Li, Z.Z. Xu, X.K. He, J. Zhang, H. Kuroda, Formation of nanogratings on the surface of a ZnSe crystal irradiated by femtosecond laser pulses, Phys. Rev. B Condens. Matter Mater. Phys. 72 (2005) 1–4. https://doi.org/10.1103/PhysRevB.72.125429.
- [7] M.H. Dar, R. Kuladeep, V. Saikiran, N.D. Rao, Femtosecond laser nanostructuring of titanium metal towards fabrication of low-reflective surfaces over broad

- wavelength range, Appl. Surf. Sci. 371 (2016) 479–487. https://doi.org/10.1016/j.apsusc.2016.03.008.
- [8] T. Kobayashi, T. Wakabayashi, Y. Takushima, J. Yan, Formation behavior of laser-induced periodic surface structures on stainless tool steel in various media, Precis. Eng. 57 (2019) 244–252. https://doi.org/10.1016/j.precisioneng.2019.04.012.
- [9] C. Florian, S. V. Kirner, J. Krüger, J. Bonse, Surface functionalization by laser-induced periodic surface structures, J. Laser Appl. 32 (2020) 022063. https://doi.org/10.2351/7.0000103.
- [10] A.Y. Vorobyev, C. Guo, Spectral and polarization responses of femtosecond laser-induced periodic surface structures on metals, J. Appl. Phys. 103 (2008) 101–104. https://doi.org/10.1063/1.2842403.
- [11] M.A. Taher, H. Prasad, Navanith Krishnan P K, N.R. Desai, S.R.G. Naraharisetty, Ellipsoidal droplet formation on anisotropic superhydrophobic copper surface, Surf. Topogr. Metrol. Prop. (2019)035001. https://doi.org/10.1088/2051-672x/ab2d80.
- [12] M.A. Taher, V.K. Rajput, N. Krishnan P K, S.R.G. Naraharisetty, The validity of triple contact line theory from hydrophilic to superhydrophobic surfaces, J. Phys. D. Appl. Phys. 55 (2022) 055305. https://doi.org/10.1088/1361-6463/ac30b8.
- [13] M. Soldera, F. Fortuna, S. Teutoburg-Weiss, S. Milles, K. Taretto, A.F. Lasag, Comparison of structural colors achieved by laser-induced periodic surface structures and direct laser interference patterning, J. Laser Micro Nanoeng. 15 (2020) 97–103. https://doi.org/10.2961/jlmn.2020.02.2004.
- [14] H. Liu, W. Lin, M. Hong, Surface coloring by laser irradiation of solid substrates, APL Photonics. 4 (2019) 051101. https://doi.org/10.1063/1.5089778.
- [15] G. Li, J. Li, Y. Hu, C. Zhang, X. Li, J. Chu, W. Huang, Femtosecond laser color

- marking stainless steel surface with different wavelengths, Appl. Phys. A Mater. Sci. Process. 118 (2015) 1189–1196. https://doi.org/10.1007/s00339-014-8868-3.
- [16] J.Bonse, R. Koter, M.Hartlelt, D. Spaltmann, S. pentzien, S. HÖhm, A. Rosenfeld, J. Krüger, Femtosecond laser-induced periodic surface structures on steel and titanium alloy for tribological applications, (2014) 103–110. https://doi.org/10.1007/s00339-014-8229-2.
- [17] J. Bonse, R. Koter, M. Hartelt, D. Spaltmann, S. Pentzien, S. Höhm, A. Rosenfeld, J. Krüger, Tribological performance of femtosecond laser-induced periodic surface structures on titanium and a high toughness bearing steel, Appl. Surf. Sci. 336 (2015) 21–27. https://doi.org/10.1016/j.apsusc.2014.08.111.
- [18] J.S. Hwang, J.E. Park, G.W. Kim, H. Lee, M. Yang, Fabrication of printable nanograting using solution-based laser-induced periodic surface structure process, Appl. Surf. Sci. 547 (2021) 149178. https://doi.org/10.1016/j.apsusc.2021.149178.
- [19] Y. Shimotsuma, P.G. Kazansky, J. Qiu, K. Hirao, Self-organized nanogratings in glass irradiated by ultrashort light pulses, Phys. Rev. Lett. 91 (2003)247405. https://doi.org/10.1103/PhysRevLett.91.247405.
- [20] E. Skoulas, A.C. Tasolamprou, G. Kenanakis, E. Stratakis, Laser induced periodic surface structures as polarizing optical elements, Appl. Surf. Sci. 541 (2021) 148470. https://doi.org/10.1016/j.apsusc.2020.148470.
- [21] A. Dostovalov, K. Bronnikov, V. Korolkov, S. Babin, E. Mitsai, A. Mironenko, M. Tutov, D. Zhang, K. Sugioka, J. Maksimovic, T. Katkus, S. Juodkazis, A. Zhizhchenko, A. Kuchmizhak, Hierarchical anti-reflective laser-induced periodic surface structures (LIPSSs) on amorphous Si films for sensing applications, Nanoscale. 12 (2020) 13431–13441. https://doi.org/10.1039/d0nr02182b.
- [22] M.A. Taher, S. Ponnan, H. Prasad, D.N. Rao, S.R.G. Naraharisetty, Broadband absorption of nanostructured stainless steel surface fabricated by nanosecond laser irradiation, Nanotechnology. 31 (2020) 175301. https://doi.org/10.1088/1361-

6528/ab674e.

- [23] S. Gräf, F.A. Müller, Polarisation-dependent generation of fs-laser induced periodic surface structures, Appl. Surf. Sci. 331 (2015) 150–155. https://doi.org/10.1016/j.apsusc.2015.01.056.
- [24] D. Dufft, A. Rosenfeld, S.K. Das, R. Grunwald, J. Bonse, Femtosecond laser-induced periodic surface structures revisited: A comparative study on ZnO, J. Appl. Phys. 105 (2009) 034908. https://doi.org/10.1063/1.3074106.
- [25] J. Bonse, S. Höhm, S. V. Kirner, A. Rosenfeld, J. Krüger, Laser-induced periodic surface structures a scientific evergreen, IEEE J. Sel. Top. Quantum Electron. 23 (2017) 9000615. https://doi.org/10.1109/jstqe.2016.2614183.
- [26] S. Höhm, M. Rohloff, A. Rosenfeld, J. Krüger, J. Bonse, Dynamics of the formation of laser-induced periodic surface structures on dielectrics and semiconductors upon femtosecond laser pulse irradiation sequences, Appl. Phys. A Mater. Sci. Process. 110 (2013) 553–557. https://doi.org/10.1007/s00339-012-7184-z.
- [27] R.A. Barb, C. Hrelescu, L. Dong, J. Heitz, J. Siegel, P. Slepicka, V. Vosmanska, V. Svorcik, B. Magnus, R. Marksteiner, M. Schernthaner, K. Groschner, Laser-induced periodic surface structures on polymers for formation of gold nanowires and activation of human cells, Appl. Phys. A Mater. Sci. Process. 117 (2014) 295–300. https://doi.org/10.1007/s00339-013-8219-9.
- [28] A. Turnali, M. Han, O. Tokel, Laser-written depressed-cladding waveguides deep inside bulk silicon, J. Opt. Soc. Am. B. 36 (2019) 966. https://doi.org/10.1364/josab.36.000966.
- [29] C. Florian, J.L. Déziel, S. V. Kirner, J. Siegel, J. Bonse, The role of the laser-induced oxide layer in the formation of laser-induced periodic surface structures, Nanomaterials. 10 (2020) 147. https://doi.org/10.3390/nano10010147.

- [30] A. Abou-Saleh, E.T. Karim, C. Maurice, S. Reynaud, F. Pigeon, F. Garrelie, L. V. Zhigilei, J.P. Colombier, Spallation-induced roughness promoting high spatial frequency nanostructure formation on Cr, Appl. Phys. A Mater. Sci. Process. 124 (2018) 1–12. https://doi.org/10.1007/s00339-018-1716-0.
- [31] P. Dominic, F. Bourquard, S. Reynaud, A. Weck, J.P. Colombier, F. Garrelie, On the insignificant role of the oxidation process on ultrafast high-spatial-frequency lipss formation on tungsten, Nanomaterials. 11 (2021) 1–10. https://doi.org/10.3390/nano11051069.
- [32] L.T. Cangueiro, A.J. Cavaleiro, J. Morgiel, R. Vilar, Mechanisms of the formation of low spatial frequency LIPSS on Ni/ Ti reactive multilayers, J. Phys. D. Appl. Phys. 49 (2016) 365103. https://doi.org/10.1088/0022-3727/49/36/365103.
- [33] H. Hikage, N. Nosaka, S. Matsuo, High-spatial-frequency periodic surface structures on steel substrate induced by subnanosecond laser pulses, Appl. Phys. Express. 10 (2017) 1141-1154. https://doi.org/10.7567/APEX.10.112701.
- [34] J. Bonse, A. Rosenfeld, J. Krüger, On the role of surface plasmon polaritons in the formation of laser-induced periodic surface structures upon irradiation of silicon by femtosecond-laser pulses, J. Appl. Phys. 106 (2009) 1-14. https://doi.org/10.1063/1.3261734.
- [35] J.E. Sipe, J.F. Young, J.S. Preston, H.M. van Driel, Laser-induced periodic surface structure. I. Theory, Phys. Rev. B. 27 (1983) 1141–1154. https://doi.org/10.1103/PhysRevB.27.1141.
- [36] H. Zhang, J.P. Colombier, C. Li, N. Faure, G. Cheng, R. Stoian, Coherence in ultrafast laser-induced periodic surface structures, Phys. Rev. B - Condens. Matter Mater. Phys. 92 (2015) 1–14. https://doi.org/10.1103/PhysRevB.92.174109.
- [37] J. Bonse, S. Gräf, Maxwell Meets Marangoni—A Review of Theories on Laser-Induced Periodic Surface Structures, Laser Photonics Rev. 2000215 (2020) 20002215. https://doi.org/10.1002/lpor.202000215.

- [38] B. Öktem, I. Pavlov, S. Ilday, H. Kalaycioğlu, A. Rybak, S. Yavaş, M. Erdoğan, F.Ö. Ilday, Nonlinear laser lithography for indefinitely large-area nanostructuring with femtosecond pulses, Nat. Photonics. 7 (2013) 897–901. https://doi.org/10.1038/nphoton.2013.272.
- [39] S. Gräf, C. Kunz, S. Engel, T.J.Y. Derrien, F.A. Müller, Femtosecond laser-induced periodic surface structures on fused silica: The impact of the initial substrate temperature, Materials (Basel). 11 (2018) 1340. https://doi.org/10.3390/ma11081340.
- [40] C. Albu, A. Dinescu, M. Filipescu, M. Ulmeanu, M. Zamfirescu, Periodical structures induced by femtosecond laser on metals in air and liquid environments, Appl. Surf. Sci. 278 (2013) 347–351. https://doi.org/10.1016/j.apsusc.2012.11.075.
- [41] T. Kobayashi, T. Wakabayashi, Y. Takushima, J. Yan, Formation behavior of laser-induced periodic surface structures on stainless tool steel in various media, Precis. Eng. 57 (2019) 244–252. https://doi.org/10.1016/j.precisioneng.2019.04.012.
- [42] A. Borowiec, H.K. Haugen, Subwavelength ripple formation on the surfaces of compound semiconductors irradiated with femtosecond laser pulses, Appl. Phys. Lett. 82 (2003) 4462–4464. https://doi.org/10.1063/1.1586457.
- [43] Z. Han, B. Li, Z. Mu, M. Yang, S. Niu, J. Zhang, L. Ren, An Ingenious Super Light Trapping Surface Templated from Butterfly Wing Scales, Nanoscale Res. Lett. 10 (2015) 344. https://doi.org/10.1186/s11671-015-1052-7.
- [44] C. Yao, Y. Ye, B. Jia, Y. Li, R. Ding, Y. Jiang, Y. Wang, X. Yuan, Polarization and fluence effects in femtosecond laser induced micro/nano structures on stainless steel with antireflection property, Appl. Surf. Sci. 425 (2017) 1118–1124. https://doi.org/10.1016/j.apsusc.2017.07.157.
- [45] L. Qi, K. Nishii, Y. Namba, Regular subwavelength surface structures induced by

- femtosecond laser pulses on stainless steel, Opt. Lett. 34 (2009) 1846. https://doi.org/10.1364/ol.34.001846.
- [46] J.E. Sipe, J.F. Young, J.S. Preston, H.M. van Driel, Laser-induced periodic surface structure. I. Theory, Phys. Rev. B. 27 (1983) 1141–1154. https://doi.org/10.1103/PhysRevB.27.1141.
- [47] S. Kumar, S.M. Eaton, M. Bollani, B. Sotillo, A. Chiappini, M. Ferrari, R. Ramponi, P. Di Trapani, O. Jedrkiewicz, Laser surface structuring of diamond with ultrashort Bessel beams, Sci. Rep. 8 (2018) 1–12. https://doi.org/10.1038/s41598-018-32415-0.
- [48] S. Wang, L. Jiang, W. Han, W. Liu, J. Hu, S. Wang, Y. Lu, Controllable formation of laser-induced periodic surface structures on ZnO film by temporally shaped femtosecond laser scanning, Opt. Lett. 45 (2020) 2411. https://doi.org/10.1364/ol.388770.
- [49] M.G. Rahimian, A. Jain, H. Larocque, P.B. Corkum, E. Karimi, V.R. Bhardwaj, Spatially controlled nanostructuring of silicon with femtosecond vortex pulses, Sci. Rep. 10 (2020) 12643. https://doi.org/10.1038/s41598-020-69390-4.
- [50] E. Allahyari, J. JJ Nivas, G. Avallone, M. Valadan, M. Singh, V. Granata, C. Cirillo, A. Vecchione, R. Bruzzese, C. Altucci, S. Amoruso, Femtosecond laser surface irradiation of silicon in air: Pulse repetition rate influence on crater features and surface texture, Opt. Laser Technol. 126 (2020) 106073. https://doi.org/10.1016/j.optlastec.2020.106073.
- [51] M.S. Brown, C.B. Arnold, Laser Precision Microfabrication, 135 (2010) 91–120. https://doi.org/10.1007/978-3-642-10523-4.
- [52] L. Torrisi, A. Borrielli, D. Margarone, Study on the ablation threshold induced by pulsed lasers at different wavelengths, Nucl. Instruments Methods Phys. Res. Sect. B Beam Interact. with Mater. Atoms. 255 (2007) 373–379. https://doi.org/10.1016/j.nimb.2006.12.144.

- [53] E.G. Gamaly, A. V. Rode, B. Luther-Davies, V.T. Tikhonchuk, Ablation of solids by femtosecond lasers: Ablation mechanism and ablation thresholds for metals and dielectrics, Phys. Plasmas. 9 (2002) 949. https://doi.org/10.1063/1.1447555.
- [54] O. Armbruster, A. Naghilou, M. Kitzler, W. Kautek, Spot size and pulse number dependence of femtosecond laser ablation thresholds of silicon and stainless steel, Appl. Surf. Sci. 396 (2017) 1736–1740. https://doi.org/10.1016/j.apsusc.2016.11.229.
- [55] M. Huang, F. Zhao, Y. Cheng, N. Xu, Z. Xu, Origin of laser-induced near-subwavelength ripples: Interference between surface plasmons and incident laser, ACS Nano. 3 (2009) 4062–4070. https://doi.org/10.1021/nn900654v.
- [56] M. Huang, Y. Cheng, F. Zhao, Z. Xu, The significant role of plasmonic effects in femtosecond laser-induced grating fabrication on the nanoscale, 86 (2013) 74–86. https://doi.org/10.1002/andp.201200136.
- [57] I. Gnilitskyi, T.J.Y. Derrien, Y. Levy, N.M. Bulgakova, T. Mocek, L. Orazi, High-speed manufacturing of highly regular femtosecond laser-induced periodic surface structures: Physical origin of regularity, Sci. Rep. 7 (2017) 8485. https://doi.org/10.1038/s41598-017-08788-z.
- [58] Z. Lin, H. Liu, L. Ji, W. Lin, M. Hong, Realization of ~10 nm Features on Semiconductor Surfaces via Femtosecond Laser Direct Patterning in Far Field and in Ambient Air, Nano Lett. 20 (2020) 4947–4952. https://doi.org/10.1021/acs.nanolett.0c01013.

# Chapter 4

# Wavelengths dependent cubic-shaped copper nanoparticles formation

#### Abstract

The effect of changing the incident laser wavelength on the surface morphology is shown via femtosecond laser direct writing on a copper surface. For the first time in the literature, we demonstrated the formation of the cubic-shaped nanoparticles (NPs) on the laser-irradiated copper surface at the incident wavelength of 860 nm. We observed the formation of laser-induced periodic surface structures (LIPSS) are favorable over a broad range of laser fluences at 900 nm irradiation wavelength. We presented the variation of low spatial frequency LIPSS (LSFL) periodicity with the change of the fluence. We did not observe clear LIPSS formation at 960 nm irradiation on the copper surface out of the four wavelengths used. The energy dispersive X-ray (EDX) spectroscopic analysis on the cubic nanostructures reveals the presence of oxygen on the copper surface. The specific copper oxygen composite formation can be achieved at 860nm.

#### 4.1. Introduction

The fabrication and investigation of metallic nanoparticles (NPs) gained tremendous attention from research communities due to their diverse applications in industry and academia[1-3]. NPs can be used in energy storage and conservation devices[4-6], as catalytic materials[3,7], in environmental technology[7–10], biological sensing applications[11,12], surface-enhanced Raman scattering[13–15], and many more. NPs use for catalyst activity triggered the research for synthesis of functionalized NPs including graphene-based catalysts[16], nanocarbon-based catalysts[17], core/shell nano catalysts[18], magnetic supported nano catalysts[19,20], etc. These various needs have been justified by rapid synthesis and preparation of NPs with different-shapes, sizes, and morphology using various methods such as solution-based preparation, e-beam lithography, extraction from the natural biological plants, and laser-induced NPs synthesis[21–25], etc. The fabrication of NPs using above mentioned conventional methods involve multiple steps, complexity, skill dependence and time-consuming. Fabrication of NPs using ultrafast laser irradiation provides a way for an easy, one-step, and green synthesis of nanoparticles. It is reliable technique because of its repeatability, controlled, precise fabrication and pollution-free method [13,14,22,26]. This process can also be easily scaled up to an industrial production.

Ultrafast laser ablation of metallic surfaces was reported using nanoseconds, picosecond, femtosecond pulsed lasers to fabricate superhydrophobic surfaces [27–29], antireflective surfaces [30–32], and various functional surfaces [30,33]. The underlying mechanisms of laser ablation depend on the materials used, irradiation parameters such as incident wavelength, pulse width, repetition rate, scanning speed or number of pulses per spot, and intensity of laser beams[34–38]. Among the class of nanoparticles, the copper NPs got

special attention due to their good performance in heat and electrical conductivity, catalytic activity, and cost-effectiveness compared to the other plasmonic metal NPs such as gold and silver[3,5].

Many researchers use femtosecond lasers for laser writing either at its fundamental frequency or at the second harmonic frequency. However, high-power lasers allow one to tune the frequencies continuously over a broad range with the help of optical parametric amplifiers. The effect of driving force frequency on the formation of the nanostructures and morphology is a relatively unexplored area of research. In this work, for the first time in the literature, we report the fabrication of laser-induced cubic shaped copper NPs decorating the laser structured surfaces. Also, we reported the formations of laser-induced periodic surface structures (LIPSS) with varying incident wavelengths. We observed that cubic-shaped copper NPs can be fabricated at only particular incident laser wavelength and at optimized laser parameters. The formation mechanism, properties of the nanoparticles, and LIPSS are discussed in this work.

#### 4.2. Experimental procedure

We used Ti: Sapphire femtosecond laser pulses of 75 fs time duration, at repetition rate of 1 kHz, 800 nm central wavelength, and energy of 6 mJ per pulse. However, we used 3 mJ/pulse energy to pump commercially purchased optical parametric amplifier (TOPAS Prime, Light Conversion) to generate tunable wavelength of the laser beam from 300 nm - 2400 nm. After initial optimization, we chose to report four wavelengths, viz.: 800 nm, 860 nm, 900 nm, and 960 nm, to irradiate the copper substrate. A microscopic objective of 10X with a numerical aperture of 0.25 is used to focus the laser beam on the substrate's surface, as shown in **Fig. 1**. The substrates were moved on raster scanning with the help of the 3D Newport nano-positioner stage, which is controlled by the ESP motion controller. The substrates were moved with a fixed scanning speed of 0.2 mm/s, and 100 µm spacing was maintained between the successive scanning. The surface morphologies are characterized by Field Emission Scanning Electron Microscope (FESEM, Zeiss Ultra55).

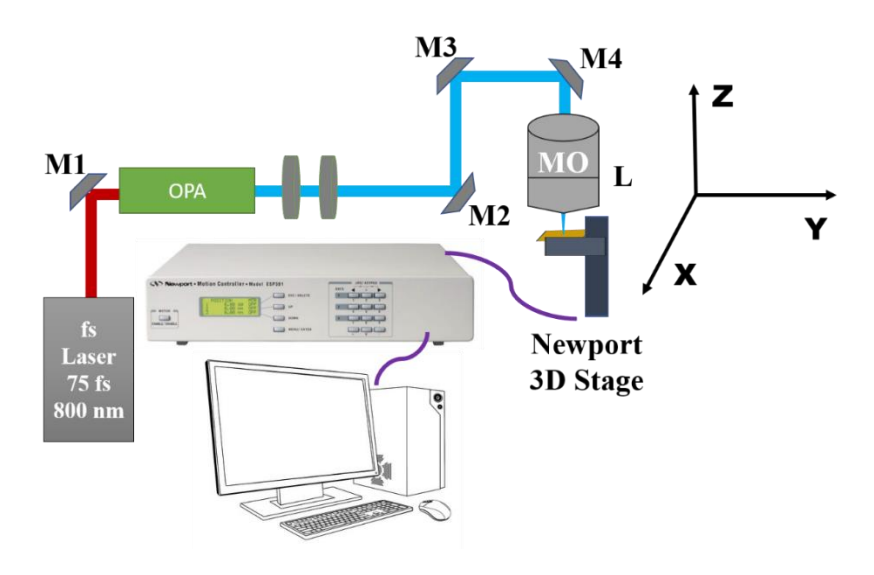


Fig. 1: Schematics of laser direct writing set-up.

#### 4.3. Results and discussions

Our initial goal is to study the variation of the LIPSS spatial periodicity over a broad range of incident wavelengths from 400 nm to 2000 nm on different materials. While working on copper surfaces, only at particular wavelengths, we found unique nanoshaped surface features as serendipity. In this work, we report only those narrow range of wavelengths. The femtosecond laser beam is focused with microscopic objectives (10X/0.25) on copper substrates with four incident wavelengths viz.: 800, 860, 900, and 960 nm, at a fixed scanning speed of 0.2 mm/s. The incident laser fluences for each wavelength are presented in **Table 1**.

**Table 1**: Laser fluences for each wavelength at which the laser direct writing experiments were performed on the copper substrates.

Fluence (J/cm <sup>2</sup> )						
800 nm	860 nm	900 nm	960 nm			
2.5	3.1	2.7	1.3			
4.1	3.9	3.5	2.4			
4.9	4.1	3.9	2.9			
5.4	7.1	6.7	3.7			

## 4.3.1. Surface morphology

### 4.3.1.1. Laser direct writing at 800 nm

**Fig 2.** On each image, the incident fluence used is indicated on the left top corner, and all are irradiated with a fixed central wavelength of 800 nm (**Fig. 2**). The FESEM images show that the low spatial frequency LIPSS (LSFL) are formed at 2.5 J/cm<sup>2</sup>, and their spatial periodicity of LSFL is 515±14 nm. The magnified area of each surface is shown in the bottom row of **Fig 2**. With the increment in fluence, LSFLs tend to get destroyed at the center of the focused beam and form feeble structures at the edges. With further increase of fluence, the LIPSS gets destroyed, and irregularly shaped particles are more likely to form, and they are randomly distributed on the laser-irradiated surfaces.

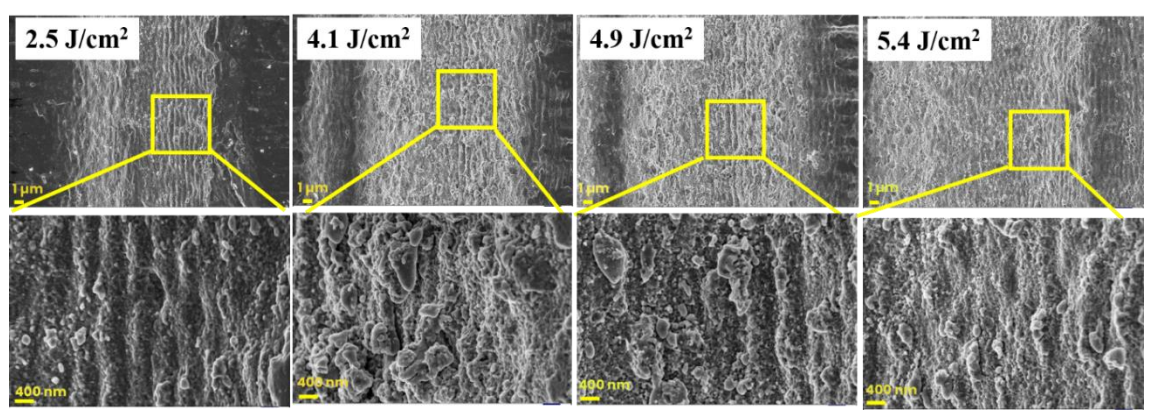


Fig. 2. FESEM images of laser-induced copper surfaces for various fluences for the incident wavelength of 800 nm. The scanning speed is fixed at 0.2 mm/s. Scale bars are equal to 1  $\mu$ m and 400 nm of the images in the first and second row, respectively.

#### 4.3.1.2. Laser direct writing at the central wavelength of 860 nm

**Fig. 3** represents the surface morphology of laser irradiated surfaces with the incident wavelength of 860 nm. The fluence varies from 3.1 to 7.1 J/cm<sup>2</sup> with a constant scanning speed of 0.2 mm/s. At this incident wavelength, the response of the copper surface is significantly different in many aspects. There is the formation of LSFL with the spatial periodicity of 732±35 nm at the incident laser fluence of 4.1 J/cm<sup>2</sup>. The most exciting surface morphological features formed at the fluence from 3.1 to 3.9 J/cm<sup>2</sup>. Apart from

the LSFL, we observe the formation of cubic-shaped copper nanoparticles of variable sizes. The particle's average sizes are found to be 127 nm and 101 nm for the incident fluence of 3.1 J/cm<sup>2</sup> and 3.9 J/cm<sup>2</sup>, respectively. It indicates that the particle sizes are reducing as the fluence increases. Upon further increase in incident fluence, the formation of cubic-shaped particles reduced and distributed over the LSFL ridges.

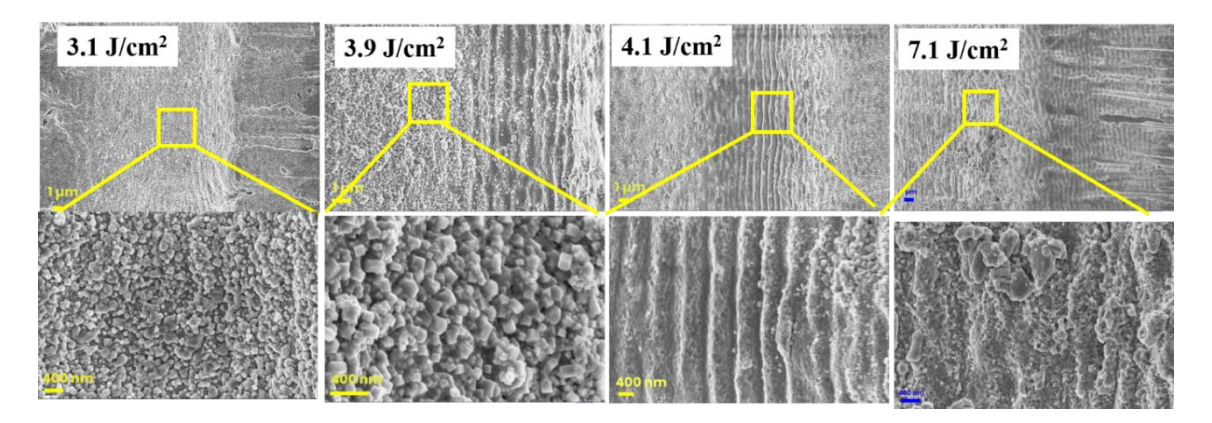


Fig. 3. FESEM images of laser-induced copper surfaces for various fluence for the incident wavelength of 860 nm. The scanning speed is fixed at 0.2 mm/s. Scale bars are equal to 1  $\mu$ m and 400 nm of the images in the first and second row, respectively.

**Fig. 4** depicts that the size of NPs change as the fluence increases; it also illustrates the impact on the shape of the copper nanoparticles. The cubic nature is not completely formed at lower incident fluences, and perfect edges are less prominent at 3.1 J/cm<sup>2</sup>. The perfect cubic nanostructures are formed only at 3.9 J/cm<sup>2</sup>. Upon further increase in incident fluence, the surface density of NPs appearance is reduced drastically and favors the formation of LSFL ridges as primary feature. At the fluence of 4.1 J/cm<sup>2</sup>, the cubic-shaped particles start disappearing, and few particles are scattered at the peripheral area of the grooves and on LSFL ridges. Upon further increase in fluence, even the LSFL structures are destroyed at the fluence of 7.1 J/cm<sup>2</sup>. The most important aspect of the effect of fluence on surface morphology is the formation of highly regular cubic-shaped copper nanoparticles. These cubic-shaped NPs are formed only at a particular fluence range when the irradiated wavelength of 860 nm. This study suggests that one can tune the formation of particle features on surfaces with incident laser parameters.

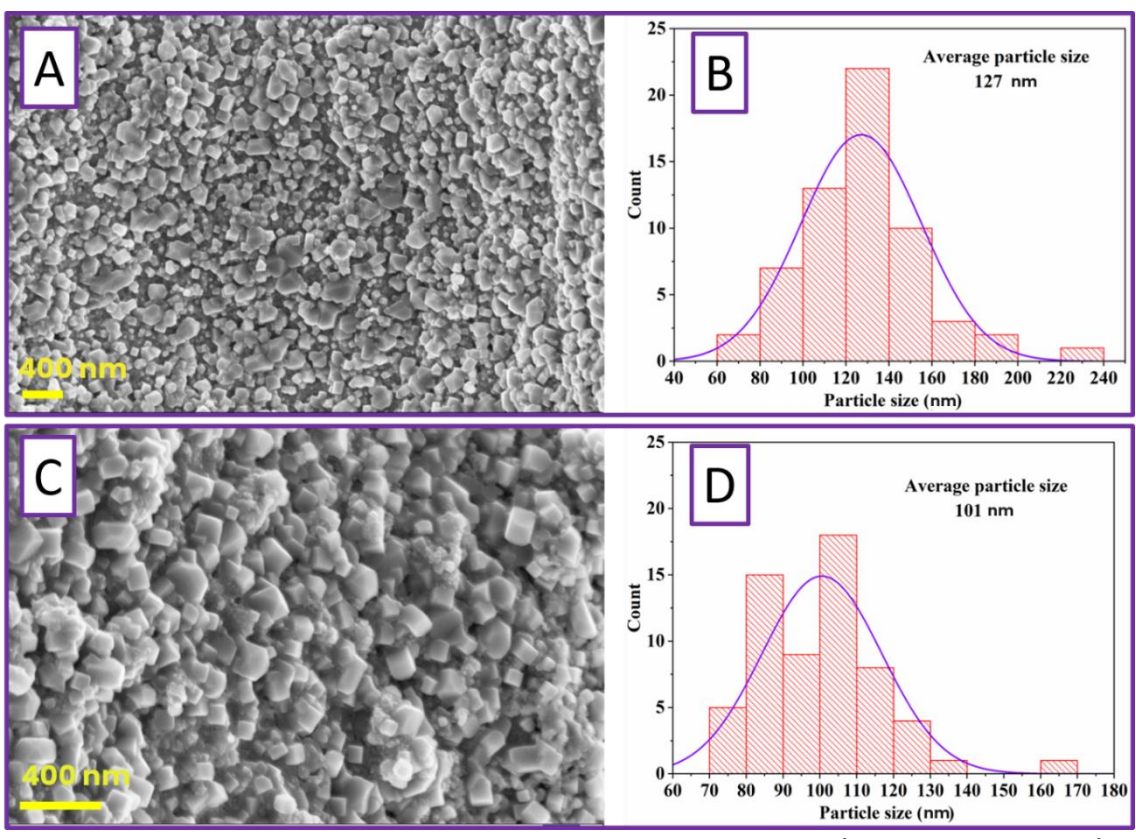


Fig. 4. Distribution of particle for the incident wavelength of  $(A \& B) 3.1 \text{ J/cm}^2$ , and  $(C \& D) 3.9 \text{ J/cm}^2$  on laser irradiated copper surfaces of the incident wavelength of 860 nm.

# 4.3.1.3. Laser direct writing at 900 nm

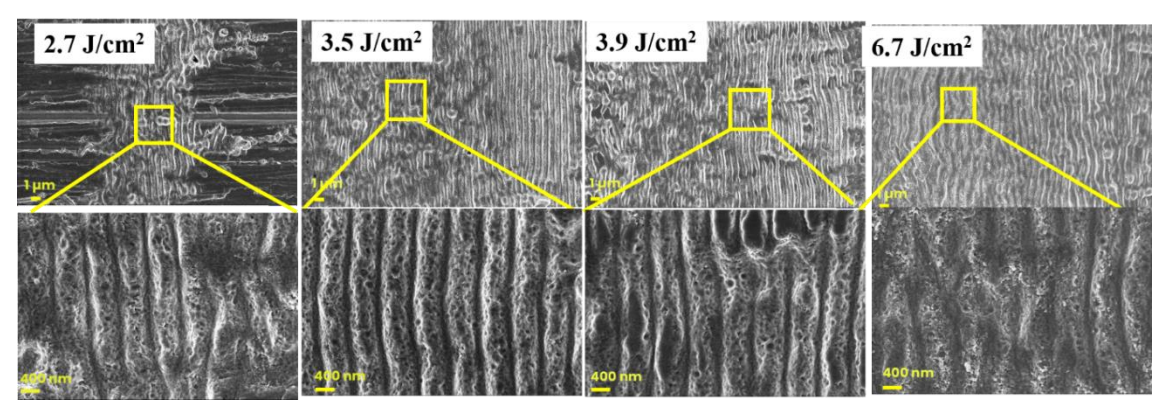
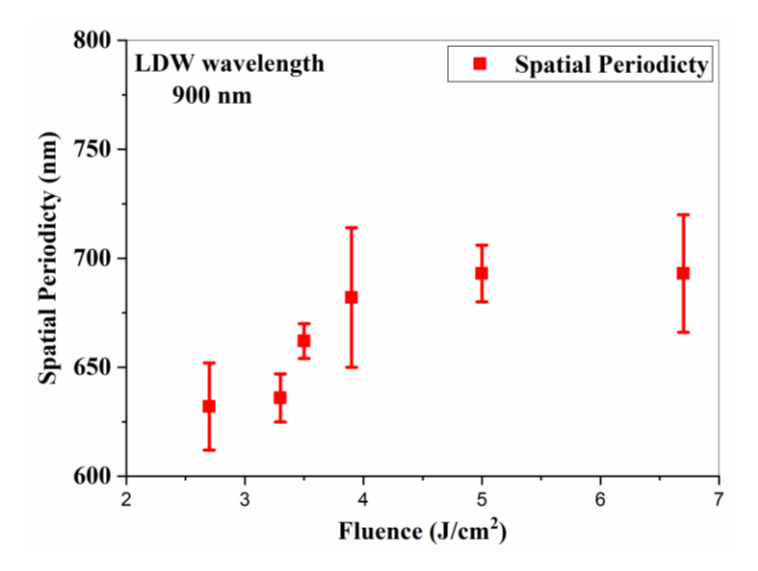


Fig. 5. FESEM images of laser-induced copper surfaces for various fluence for the incident wavelength of 900 nm. The scanning speed is fixed at 0.2 mm/s. Scale bars are equal to 1  $\mu$ m and 400 nm of the images in the first and second row, respectively.

**Fig. 5** shows the surface morphological features of laser irradiated surfaces with the incident wavelength of 900 nm. One can see that for each fluence, the formation of LSFL

is observed. As the fluence increases, the smooth LSFL are formed over a larger area. The best regular LSFL formed at 3.5 J/cm<sup>2</sup> with a spatial periodicity of 662±8 nm.

There is a variation of LSFL spatial periodicity with the incident fluence on the copper irradiated surfaces, with an incident wavelength of 900 nm. The spatial periodicity increases from 632±20 nm to 693±13 nm as the fluence increases from 2.7 J/cm² to 5.0 J/cm². As we increased the fluence further, the spatial periodicity remained close to 693±13 nm. This variation of spatial periodicity with respect to fluence is shown in **Fig.** 6. This analysis is presented only at incident wavelength of 900 nm as LSFL are forming over a broad range of fluences, which is not the case for other wavelengths.



**Fig. 6.** Variation of spatial periodicity of LSFL with incident laser fluence for the incident wavelength of 900 nm.

#### 4.3.1.4. Laser direct writing at 960 nm

The effect of incident fluence on the surface morphology is shown in **Fig. 7** for the incident wavelength of 960 nm. One can observe the formation of particulate-type features throughout the patterned surface for this wavelength. There is no signature of LIPSS formation at this wavelength, even from low to higher fluences for this objective type of focusing. For this incident wavelength, as the fluence increases, the depth of the grooves increases. At the fluence of 2.9 J/cm<sup>2</sup>, the surface morphology at the center of the laser-focused beam looks like a molten state with several cracks throughout the grooves.

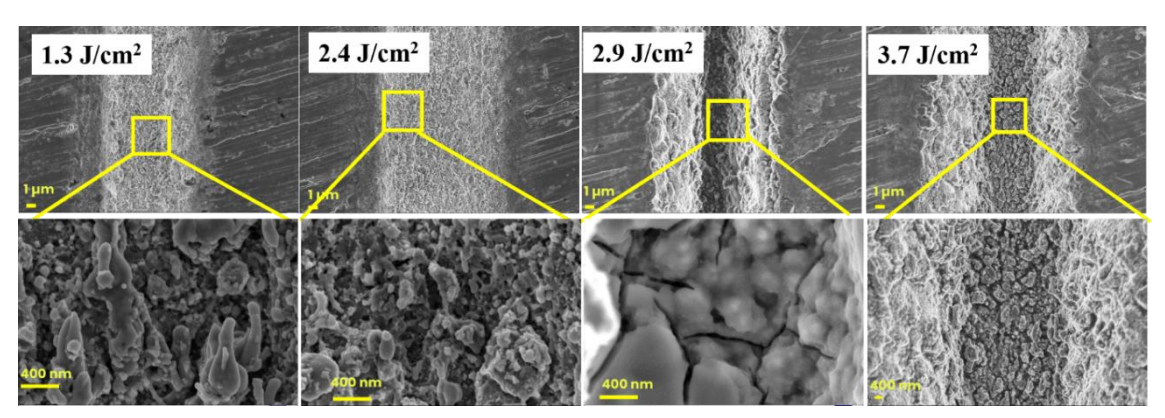


Fig. 7. FESEM images of laser-induced copper surfaces for various fluence for the incident wavelength of 960 nm. The scanning speed is fixed at 0.2 mm/s. Scale bars are equal to 1  $\mu$ m and 400 nm of the images in the first and second row, respectively.

In summary, the response of the surface to the incident wavelength is quite different. Each incident wavelength interacted with the surface differently and led to the formations of various surface morphology. At the incident wavelength of 800 nm, both the irregular particles and LSFL formations are observed, whereas the formation of highly regular cubic shaped NPs and LSFL are appeared for the incident wavelength of 860 nm only. At the incident wavelength of 900 nm, only LSFL formed; no particulate type features nor the regular cubic-shaped structures are formed. Finally, at the incident wavelength of 960 nm, irregular particles formed at the lower side of the fluence. The deep groove with cracks is formed and depth of the groove increased with fluence.

#### 4.3.2. Elemental Analysis on different surface structures

The EDX analysis is carried out to probe the elemental composition of LIPSS, cubic features, and unpatterned surfaces. The EDX of the un-irradiated surface reveals the presence of copper only, as shown in **Fig. 8**.

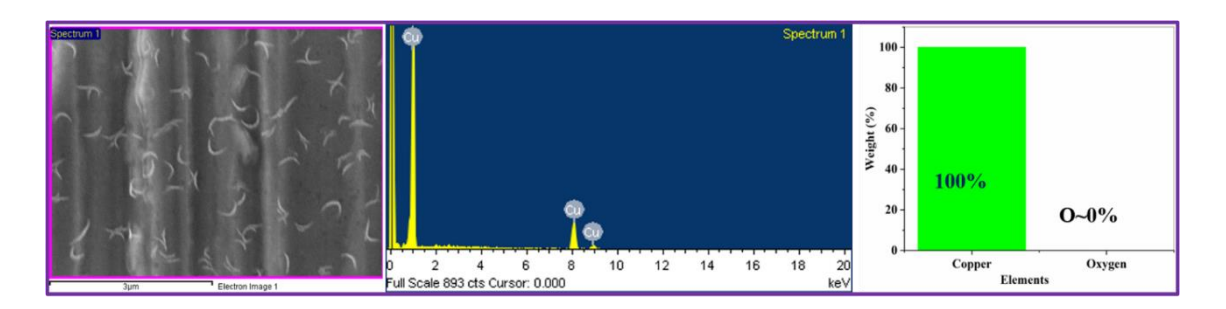


Fig. 8. EDX analysis of the unpatterned surfaces. The scale bar is equal to 3  $\mu$ m.

In **Fig. 9**, the EDX is taken on two different portions of cubic features, (i) large area of cubic structures and (ii) small area of cubic features. It is clear from the EDX analysis, that the percentage weight of copper and oxygen is 95.51% and 4.49%, respectively, over the large area ( $\sim$ 36  $\mu$ m<sup>2</sup>). Large area cubic features are dispersed on the copper surfaces shown in the top row of **Fig. 9**.

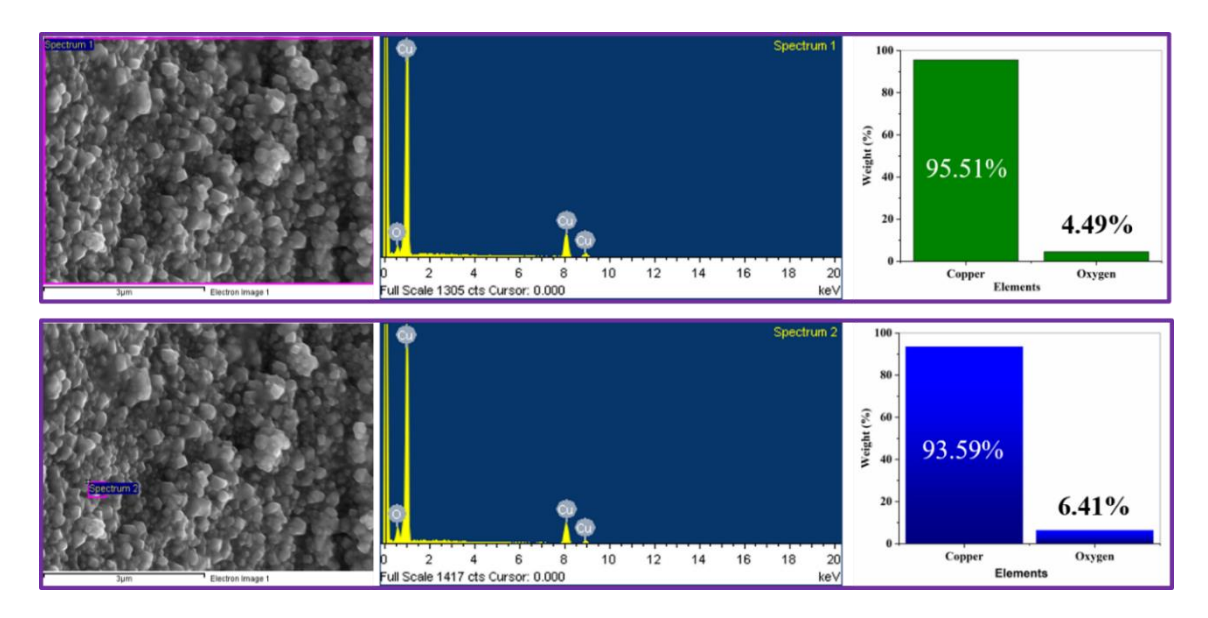


Fig. 9. Energy dispersive analysis of cubic copper features. The scale bar is equal to 3  $\mu$ m.

There is a slight change in elemental composition ratio when EDX is taken at a smaller area ( $\sim 0.09 \ \mu m^2$ ) close to single cube as show in the second row of Fig. 9. The presence of oxygen increased compared to the earlier case; the percentage weight of copper and oxygen are 93.59% and 6.41%, respectively. It clearly shows that oxygen is trapped on the surface during the irradiation using 860 nm, only at lower fluences. In contrast, EDX

analysis depicts completely different aspects of the elemental composition of LIPSS features. The composition analysis reveals 100% copper on LIPSS surfaces, and oxygen is null, as shown in **Fig. 10**.

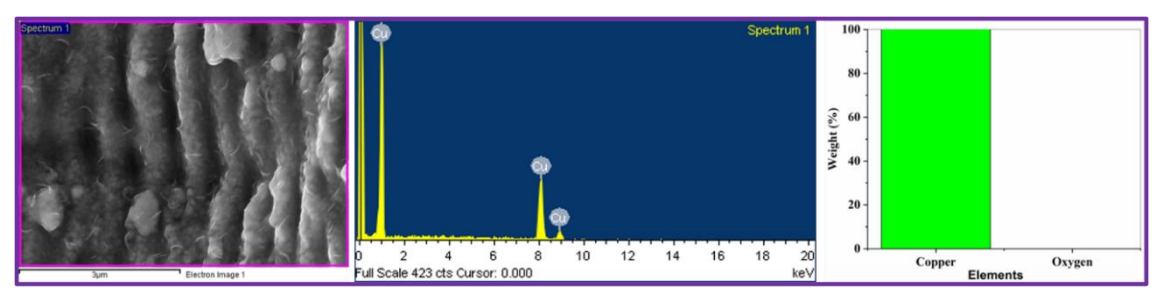


Fig. 10. EDX analysis on LIPSS formation on laser-irradiated surfaces. The X-ray signatures show it is pure copper, and the result is the same even in the zoomed areas moved all over the surface. The scale bar is equal to  $3 \, \mu m$ .

In summary, the compositions of LIPSS are purely periodic modulation of copper materials itself, whereas cubic features are composites of copper and oxygen elements. Further studies and experiments are needed to understand the underlying physics, why the oxygen can gets trapped during the irradiation of 860 nm but not happening at other wavelengths.

#### 4.4. Conclusions

Controlled fabrication of cubic-shaped copper NPs on the surface of copper is shown for the first time in the literature. This can be achieved uniquely via femtosecond laser irradiation using a particular incident wavelength, scanning speed, and incident laser fluence. We showed surface topological structures could be controlled or varied using different wavelengths and irradiation energy. The ideal wavelength for the formation of LIPSS over a broad range of energies is 900 nm. The variation of the LIPSS periodicity with energy is presented for 900 nm; at higher fluences, the periodicities remain constant until they get randomized at destruction energies. At 960 nm of irradiation wavelength, we could not observe any LIPSS formation for any incident energy. Cubic-shaped nanoparticles will have the maximum surface area with many edges can have several potential applications, especially in catalytic reactions as electrodes. The formation of the cubic structures is because of the oxygen being trapped; it is favored only at 860 nm

central wavelength of femtosecond pulses. We believe this type of wavelength-dependent surface structuring will have many more potential applications and new physics to be explored in many more materials.

#### References

- [1] G.H. Chan, J. Zhao, E.M. Hicks, G.C. Schatz, R.P. Van Duyne, Plasmonic properties of copper nanoparticles fabricated by nanosphere lithography, *Nano Lett*. 7 (2007) 1947–1952.
- [2] A. Radi, D. Pradhan, Y. Sohn, K.T. Leung, Nanoscale Shape and Size Control of, *ACS Nano*. 4 (2010) 1553–1560.
- [3] M.B. Gawande, A. Goswami, F.X. Felpin, T. Asefa, X. Huang, R. Silva, X. Zou, R. Zboril, R.S. Varma, Cu and Cu-Based Nanoparticles: Synthesis and Applications in Catalysis, *Chem. Rev.* 116 (2016) 3722–3811.
- [4] S. Lohrasbi, M. Sheikholeslami, D.D. Ganji, Multi-objective RSM optimization of fin assisted latent heat thermal energy storage system based on solidification process of phase change Material in presence of copper nanoparticles, *Appl. Therm. Eng.* 118 (2017) 430–447.
- [5] A. Tamilvanan, K. Balamurugan, K. Ponappa, B.M. Kumar, Copper nanoparticles: Synthetic strategies, properties and multifunctional application, *Int. J. Nanosci.* 13 (2014). https://doi.org/10.1142/S0219581X14300016.
- [6] D. Shin, D. Banerjee, Enhancement of specific heat capacity of high-temperature silica-nanofluids synthesized in alkali chloride salt eutectics for solar thermal-energy storage applications, *Int. J. Heat Mass Transf.* 54 (2011) 1064–1070.
- [7] P. Deka, B.J. Borah, H. Saikia, P. Bharali, Cu-Based Nanoparticles as Emerging Environmental Catalysts, *Chem. Rec.* 19 (2019) 462–473.
- [8] S. Saran, G. Manjari, S.P. Devipriya, Synergistic eminently active catalytic and recyclable Ag, Cu and Ag-Cu alloy nanoparticles supported on TiO2 for sustainable and cleaner environmental applications: A phytogenic mediated synthesis, *J. Clean. Prod.* 177 (2018) 134–143.
- [9] S.C.N. Tang, I.M.C. Lo, Magnetic nanoparticles: Essential factors for sustainable

- environmental applications, Water Res. 47 (2013) 2613–2632.
- [10] S.M. Abdelbasir, K.M. McCourt, C.M. Lee, D.C. Vanegas, Waste-Derived Nanoparticles: Synthesis Approaches, Environmental Applications, and Sustainability Considerations, *Front. Chem.* 8 (2020) 782. https://doi.org/10.3389/fchem.2020.00782.
- [11] M.I. Din, R. Rehan, Synthesis, Characterization, and Applications of Copper Nanoparticles, *Anal. Lett.* 50 (2017) 50–62.
- [12] Y. Tauran, A. Brioude, A.W. Coleman, M. Rhimi, B. Kim, Molecular recognition by gold, silver and copper nanoparticles, *World J. Biol. Chem.* 4 (2013) 35. https://doi.org/10.4331/wjbc.v4.i3.35.
- [13] M. Muniz-Miranda, C. Gellini, E. Giorgetti, Surface-enhanced Raman scattering from copper nanoparticles obtained by laser ablation, *J. Phys. Chem. C.* 115 (2011) 5021–5027.
- [14] P.K. Baruah, A. Singh, L. Rangan, A.K. Sharma, A. Khare, Optimization of copper nanoparticles synthesized by pulsed laser ablation in distilled water as a viable SERS substrate for karanjin, *Mater. Chem. Phys.* 220 (2018) 111–117.
- [15] X. Zhang, S. Xu, S. Jiang, J. Wang, J. Wei, S. Xu, S. Gao, H. Liu, H. Qiu, Z. Li, H. Liu, Z. Li, H. Li, Growth graphene on silver-copper nanoparticles by chemical vapor deposition for high-performance surface-enhanced Raman scattering, *Appl. Surf. Sci.* 353 (2015) 63–70.
- [16] H. Fang, M. Wen, H. Chen, Q. Wu, W. Li, Graphene stabilized ultra-small CuNi nanocomposite with high activity and recyclability toward catalysing the reduction of aromatic nitro-compounds, *Nanoscale*. 8 (2016) 536–542.
- [17] Y. Wang, X. Duan, Y. Xie, H. Sun, S. Wang, Nanocarbon-Based Catalytic Ozonation for Aqueous Oxidation: Engineering Defects for Active Sites and Tunable Reaction Pathways, *ACS Catal.* 10 (2020) 13383–13414.
- [18] R.K. Swarnkar, S.C. Singh, R. Gopal, Effect of aging on copper nanoparticles synthesized by pulsed laser ablation in water: Structural and optical characterizations, *Bull. Mater. Sci.* 34 (2011) 1363–1369.
- [19] R. Hudson, Y. Feng, R.S. Varma, A. Moores, Bare magnetic nanoparticles:

- Sustainable synthesis and applications in catalytic organic transformations, *Green Chem.* 16 (2014) 4493–4505.
- [20] B. Karimi, F. Mansouri, H.M. Mirzaei, Recent Applications of Magnetically Recoverable Nanocatalysts in C-C and C-X Coupling Reactions, *ChemCatChem.* 7 (2015) 1736–1789.
- [21] P. Liu, H. Wang, X. Li, M. Rui, H. Zeng, Localized surface plasmon resonance of Cu nanoparticles by laser ablation in liquid media, *RSC Adv.* 5 (2015) 79738–79745.
- [22] C. Wei, Q. Liu, Shape-, size-, and density-tunable synthesis and optical properties of copper nanoparticles, *CrystEngComm*. 19 (2017) 3254–3262.
- [23] A.R. Sadrolhosseini, A.S.B.M. Noor, K. Shameli, G. Mamdoohi, M.M. Moksin, M. Adzir Mahdi, Laser ablation synthesis and optical properties of copper nanoparticles, *J. Mater. Res.* 28 (2013) 2629–2636.
- [24] I.U. Haq, K. Akhtar, K. Malook, Synthesis and characterization of monodispersed copper oxide and their precursor powder, *Mater. Res. Bull.* 57 (2014) 121–126.
- [25] J. Zizzo, Toxicity effects of Cubic Cu2O nanoparticles on defecation rate and length in C. Elegans, *Biomed. Res. Ther.* 7 (2020) 4045–4051.
- [26] M.I.S.M.H. Tan, A.F. Omar, M. Rashid, U. Hashim, VIS-NIR spectral and particles distribution of Au, Ag, Cu, Al and Ni nanoparticles synthesized in distilled water using laser ablation, *Results Phys.* 14 (2019) 102497.
- [27] C.V. Ngo, D.M. Chun, Control of laser-ablated aluminum surface wettability to superhydrophobic or superhydrophilic through simple heat treatment or water boiling post-processing, *Appl. Surf. Sci.* 435 (2018) 974–982. https://doi.org/10.1016/j.apsusc.2017.11.185.
- [28] M. Martínez-Calderon, A. Rodríguez, A. Dias-Ponte, M.C. Morant-Miñana, M. Gómez-Aranzadi, S.M. Olaizola, Femtosecond laser fabrication of highly hydrophobic stainless steel surface with hierarchical structures fabricated by combining ordered microstructures and LIPSS, *Appl. Surf. Sci.* 374 (2016) 81–89.
- [29] M.A. Taher, H. Prasad, P.K. Navanith Krishnan, N.R. Desai, S.R.G. Naraharisetty, Ellipsoidal droplet formation on anisotropic superhydrophobic copper surface,

- Surf. Topogr. Metrol. Prop. 7 (2019). https://doi.org/10.1088/2051-672X/ab2d80.
- [30] F.A. Müller, C. Kunz, S. Gräf, Bio-inspired functional surfaces based on laser-induced periodic surface structures, *Materials* (*Basel*). 9 (2016). https://doi.org/10.3390/ma9060476.
- [31] M.A. Taher, S. Ponnan, H. Prasad, D.N. Rao, S.R.G. Naraharisetty, Broadband absorption of nanostructured stainless steel surface fabricated by nanosecond laser irradiation, *Nanotechnology*. 31 (2020) 175301. https://doi.org/10.1088/1361-6528/ab674e
- [32] M.A. Taher, S.R.G. Naraharisetty, D. Narayana Rao, Super black stainless steel surface fabricated by nanosecond laser irradiation, *Opt. InfoBase Conf. Pap.* Part F181- (2020). https://doi.org/10.1364/CLEO\_AT.2020.JW2B.21
- [33] X. Zhang, F. Shi, J. Niu, Y. Jiang, Z. Wang, Superhydrophobic surfaces: From structural control to functional application, *J. Mater. Chem.* 18 (2008) 621–633.
- [34] N.K. Roy, O.G. Dibua, W. Jou, F. He, J. Jeong, Y. Wang, M.A. Cullinan, A comprehensive study of the sintering of copper nanoparticles using femtosecond, nanosecond, and continuous wave lasers, *J. Micro Nano-Manufacturing*. 6 (2018) 1–21.
- [35] A.R. Sadrolhosseini, S. Abdul Rashid, A. Zakaria, K. Shameli, Green fabrication of copper nanoparticles dispersed in walnut oil using laser ablation technique, *J. Nanomater*. 2016 (2016). https://doi.org/10.1155/2016/8069685.
- [36] B.D. Harishchandra, M. Pappuswamy, A. PU, G. Shama, P. A, V.A. Arumugam, T. Periyaswamy, R. Sundaram, Copper Nanoparticles: A Review on Synthesis, Characterization and Applications, *Asian Pacific J. Cancer Biol.* 5 (2020) 201-210.
- [37] B. Khodashenas, H.R. Ghorbani, Synthesis of copper nanoparticles: An overview of the various methods, *Korean J. Chem. Eng.* 31 (2014) 1105–1109.
- [38] D.A. Goncharova, T.S. Kharlamova, I.N. Lapin, V.A. Svetlichnyi, Chemical and Morphological Evolution of Copper Nanoparticles Obtained by Pulsed Laser Ablation in Liquid, *J. Phys. Chem. C.* 123 (2019) 21731–21742.

# Chapter 5

# Broadband super black stainless-steel surface fabricated by nanosecond laser irradiation

#### **Abstract**

Broadband absorbing surfaces covering the UV, visible, and near IR regions are of great importance for the low light imaging devices, optical and optoelectronic devices. The fabrication of absorbing stainless steel (SS) surfaces is carried out by Laser Direct Writing Technique with an inexpensive and robust 532 nm ns laser. The nanostructured SS surfaces are highly absorbing due to the presence of nanoflower-like cavity structures along with micro-nano hierarchical surface features. These unique hierarchical structures with nanorods, nanoparticles, and nanocavities completely trap the photon incident on these surfaces due to multiple reflections. The measured specular reflectivity over a wide spectral region (250-1800 nm) is less than 0.5%, over a large range of incident angles and for both orthogonal polarizations. These surface structures and the presence of elemental percentages are changing (especially oxygen) with time. We believe these antireflection surfaces will play a vital role in many modern technological applications because of their high absorption coefficient and long-term stability.

#### 5.1. Introduction

Many industrial applications, such as optical devices in sensing, light energy harvesting devices, anti-reflective devices, low light imaging systems, demand broad band low reflecting or near-complete absorbing surfaces. The study of these surfaces has been a significant field of research for many decades. The destructive interference of dielectric coating optimized for a certain wavelength range is a century-old and still widely used technology. Several multilayers are used in modern technology to couple light over broad wavelength ranges of the order of hundreds of nanometres. [1,2]. Surface structuring at the nanoscale has recently become popular in applications where low surfaces, such as display technologies [3] [4], solar cell panels [5–9], light-emitting diodes [10], optoelectronics [11], etc. The researchers were inspired by nature to investigate these interesting micro and subwavelength hierarchical structures like moth eyes [12,13], grass wing butterfly (Greta Oto)[12,14], which are famous examples of the highly antireflective surface formed due to structured surfaces. The antireflection surface of a moth's eye comprises a sharp array of nipple-like protuberances that are packed hexagonally. Exciting techniques in this direction have been explored with different perspectives such as destructive interference coating[2,4], impedance or gradient refractive index matching[1,15–18], lamellar or geometrical light trapping, selective absorption based on surface plasmon polariton process[3,19–21]. The broad essence of these investigations is that metal nanoparticles with a diameter smaller than the wavelength enhance light coupling into the medium. [7]. The preceding efforts were carried out to obtain nearperfect antireflection effects for narrowband applications.

In this work, we explored the broadband absorption of metal surfaces. Many ways have been ascribed to suppressing reflectance from a metallic surface, such as the construction of quarter-wavelength layers [22], plasmonic light trapping[23–26], and many other chemical coatings [4,26]. Due to induced scattering by surface plasmon resonances, nanoparticles (NPs) deposited on metal surfaces improve light confinement, whose efficiency varies depending on the metal type, size, and shape. Due to backscattering losses, NPs of a single size deposited on a flat surface is inefficient over broadband

absorption. The heterogeneous metal nanoparticles produced by electron beam evaporation, as subwavelength structures, can be used to form broadband absorbing surfaces to some extent [25,27]. The most efficient broadband absorption from UV-visible to near-infrared of any surface is still far from the practical reality with near-complete absorption. Few experimental works have reported effective broadband absorbing surfaces in the infrared region [28–30] and UV-visible [25,27–34] range. The latest work reported by Brain and co-workers showed superefficient absorbing surface effective over UV to THz by growing the carbon nanotubes (CNT) on the Aluminum metal surface [35]. However, this process involves several steps and electro-deposition of materials to form CNT on the surface of the metal, and coating thickness is very large in the orders of ~100µm. In general coating or depositing another material on surfaces, do have a life time and their performance do degrade over a time. In the current work, we present a different technique where no other external chemicals are used and the surface modifications are limited to very few hundreds of nanometers not in the micron level thick coatings.

Pulsed lasers have become a popular tool for fabricating interesting nanostructures on metallic surfaces in recent times, surface modifications thickness of ~ 5 μm, having a wide range of applications in controlling wettability and optical properties [36,37]. The laser patterning is very effective for manufacturing AR surfaces, as it is a single-step process, can be scaled to the industry with precise, controllable parameters. The femtosecond laser surface patterning has demonstrated its ability in sub-wavelength ripples [38], laser-induced periodic surface structures [33,39], non-periodic blackening on semiconductors[30], blackening of metals surfaces [40,41]. Researchers reported the use of picosecond lasers for the fabrication of absorbing copper surfaces[34,42,43]. However, in very few works, lasers with a pulse width in nanoseconds, where the thermal effects are very prominent on the surface, are also explored for antireflective properties. Surface coloring on SS substrates has been shown using nanosecond laser in the recent past by H Liu and his co-workers [44]. Blackening of metals using inexpensive and rugged nanosecond laser is demonstrated on copper[31], Ti surface[45], Nickel surface[46] over 300 nm to 700 nm limited range with effective absorbance greater than

95%. In all the above-presented literature using fs, ps, and ns laser ablation, the best average absorbance is close to 97% over a broad spectrum covering 250nm to 1800 nm. In our current work, we demonstrated near 99.5% absorbance over the range of 250 nm to 1800 nm using the affordable nanosecond laser on the SS surface. This is the best antireflective SS surface, fabricated using the nanosecond laser ablation to the best of our knowledge. The observed efficiencies are due to the efficient light trapping in the fascinating micro-nano hierarchal structures formed after the laser patterning. We observed various types of morphology changes while varying the fluence of laser pulses used for irradiating the SS surface. We observed phenomenally low reflectivity as less than 0.14% in the visible region. We have observed the evolution of surface morphological features over one year, where these surfaces have shown excellent stability without any degradation in their performance.

#### 5.2. Experimental Procedure

We employed a nanosecond pulsed Nd: YAG laser (Quanta-Ray INDI) second harmonic with a central wavelength of 532 nm, 6 ns pulse width at FWHM, and 10 Hz repetition rate for direct laser writing. As shown schematically in **Fig. 1**, we kept the substrates on two-dimensional (XY) synchronized stepper motor stages that interface with the LabVIEW software. We chose SS304 as the substrate for this work because of its outstanding strength, corrosion resistance, metallic shine, and flexibility. Before the direct laser writing, the substrates were polished with SiC sandpapers of grit size 600, then 1200, and finally 1500 for a uniform surface finish. The substrates are then gently rinsed with water, then distilled water before being sonicated with methanol for 10-15 minutes to clean them thoroughly. We performed direct laser writing on five stainless substrates A1, A2, A3, A4, and A5 at a fluence of 5.65 J/cm², 7.07 J/cm², 8.48 J/cm², 9.90 J/cm², and 28.28 J/ cm², respectively, presented in **Table 1**. After the direct laser writing, the substrates were sonicated once more to remove any weakly bound particles and dirt from the surface.

T-11. 1. I		C 1	C	C	<b>:</b>
Table.1: Laser irradiation	parameters o	r substrates	tor sur	тасе рашеі	mıng.

Substrate	Energy per pulse (mJ)	Fluence (J/cm <sup>2</sup> )
A1	4	5.65
A2	5	7.07
A3	6	8.48
A4	7	9.90
A5	20	28.28

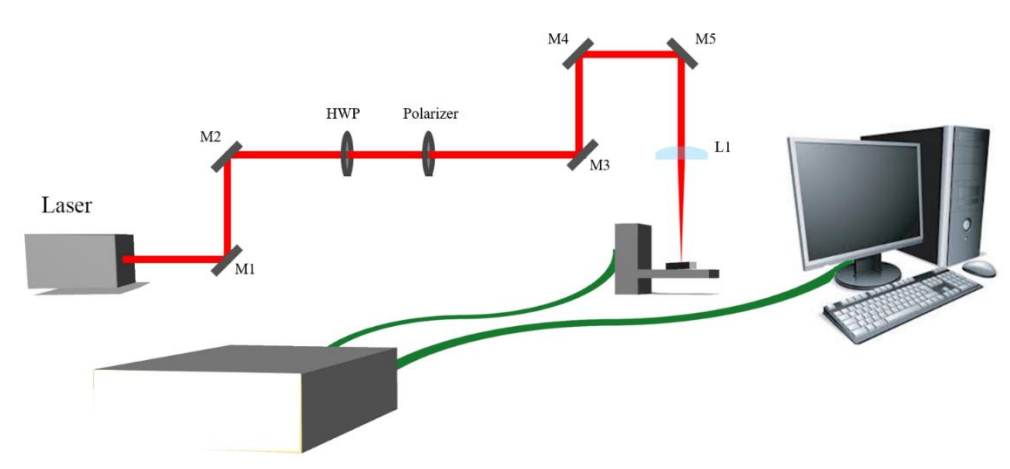


Fig. 1. Schematic of Experimental setup for laser surface structuring.

Surface morphology and elemental distribution were analyzed with a high-resolution FESEM (Zeiss Ultra55) with an accelerating voltage in the range of 5-10 kV. The reflectivity measurement is carried out using a commercial UV-Vis-NIR spectrophotometer (JASCO V-670, ARN-731) in single beam mode with a variable angle. XRD study was done using Xpert analytical (Cu source  $K_{\alpha 1} = 1.540598 \, \dot{A}$ ).

#### 5.3. Results and discussions

Reflectivity is described as the fraction of electromagnetic power reflected from a material's interface, and it is highly dependent on the wavelength of the incident light, angle of incidence, dielectric constants of the interfaces, and surface morphology. We used a nanosecond pulsed laser to manufacture composite micro-nano structured metallic surfaces to achieve a near-perfect absorbing surface over a wide wavelength range. Using laser writing techniques, the macroscopic properties of the surface are generally

controlled by manipulating the surface morphological characteristics. Laser and processing parameters such as pulse fluence, repetition rate, pulse width, wavelength, and scanning speed are frequently exploited for surface patterning. This work investigated laser pulse fluence's effect on surface topography SS substrates for five distinct values, as shown in **Table 1**. The samples are patterned by raster scanning, with a line spacing of 320 µm and a scanning speed of 0.4 mm/s. In the first section, we will discuss the impact of pulse fluence on the substrate's surface morphology; in the second section, we will discuss incident angle dependence reflectivity; and in the third section, we will discuss the effect of polarisation dependence reflectivity for each patterned surface.

# **5.3.1. Surface morphology**

**Fig. 2** shows the optical microscope images of nanosecond irradiated substrates with different fluences (A1-A5 as per **Table 1**). The FSESM images at 100 μm scale bar show that all macroscopic surface morphologies of substrates were more or less similar to having the same features, as shown in the middle column of **Fig. 2**; one can observe track of the laser scanning. However, at higher resolutions. Surface morphologies reveal two distinct regions: inside the irradiated focused beam and peripheral areas. There were particulate types of features within the focused beam spot that appeared inside the beam track, as could be seen from first column images as shown in **Fig. 2** with 4 μm scale bar. One can observe near-spherical-shaped microparticles deposited in this region. With the increase of fluence, the number of microscopic particles density is increasing from A1 to A4, average RMS roughness obtained by Gwyddion software is increasing from A1 to A4 as 42, 50, 50, and 57 nm, respectively. At A4, one can observe maximum density; with the increase of fluence, these particles completely lost their features, as shown in the first column of A5.

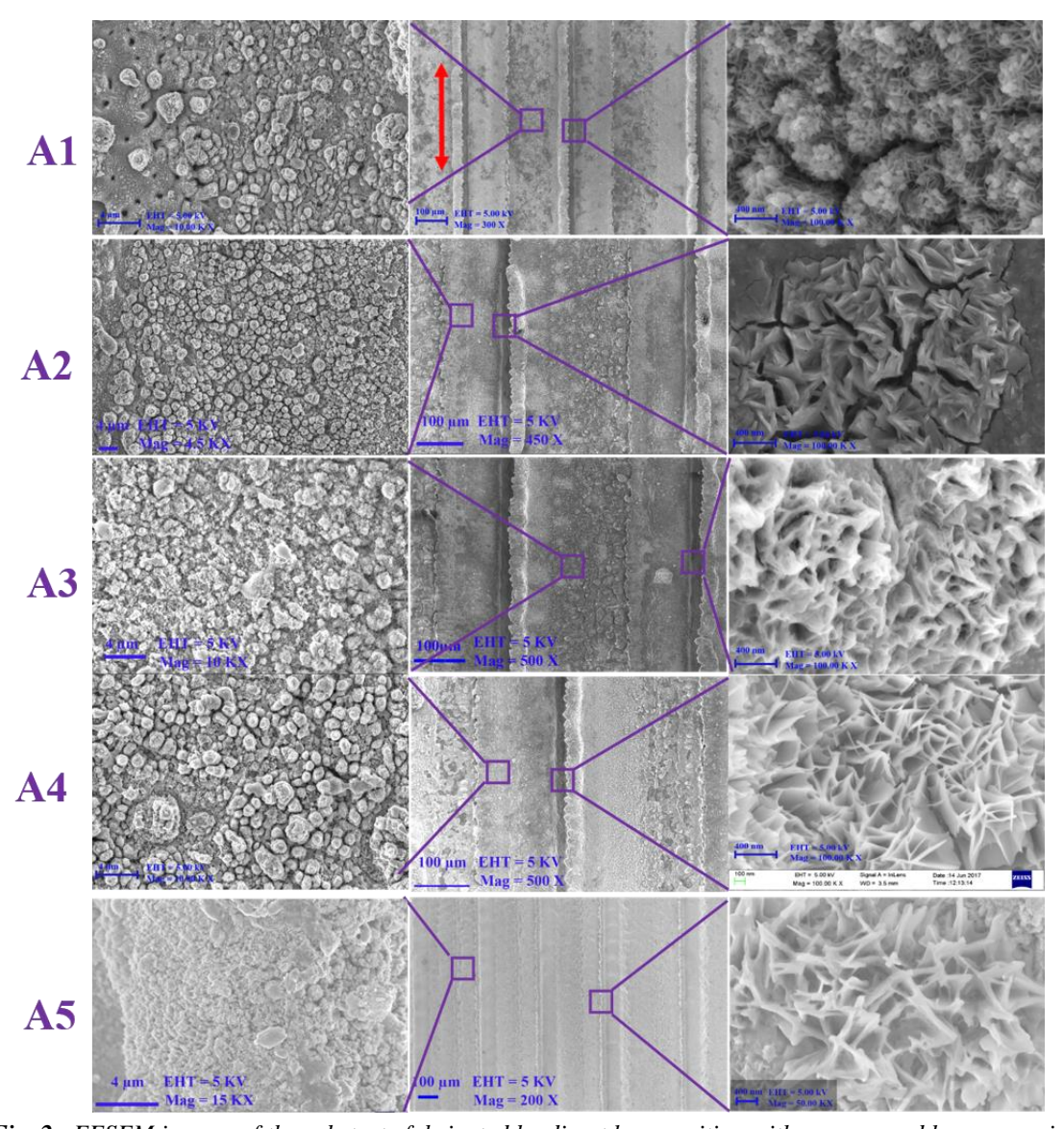


Fig. 2. FESEM images of the substrate fabricated by direct laser writing with nanosecond laser scanning with periodical fashion and line spacing between two consecutive scans are 320  $\mu$ m. A1 to A5 are different substrates (as per table) with a scanning speed of 0.4 mm/s. The red double arrow shows the laser scanning direction.

At even higher magnification (400 nm resolution bar) in the peripheral areas, we could observe superfine features, and the surface morphologies are significantly different at different fluences, as shown in the last column of **Fig. 2**. At a lower fluence (A1, 5 .65 J/cm<sup>2</sup>), the surface morphologies at the periphery of the grooves have composite nanoparticle types of features. Each of the particulates are connected with nanowires at the surface level, cactus spine-like futures. These surfaces act as a three-dimensional

mesh for the incident photons. At slightly higher fluence (A2, 7.07J/cm²), nano-rods turned into the molten state features having several cracks at the peripheral area, and more nanostructures are formed with reduced air gaps. At higher fluences for A3 and A4, those molten state again turns into flower-type features with very sharp boundaries, no air gaps, and depth, which is more suitable for acting as a nanocavity to trap the incident photons. Also, surface plasmons get excited by the incident light on these nanocavities and propagate along the substrate's surface. This leads to an efficient absorption of the incident photons[3,23,24,26,27]. When we further raise the fluence in A5, the sharpness of these flower-like futures has been destroyed, as evident from **Fig. 2**. The best microparticles and the nano-flower-like features are observed in the A4 substrate, and we treat this as optimized laser energy for obtaining these hierarchical structures. These surface morphologies are ideal for better trapping the photons incident on them over broad wavelength ranges, which can be realized from the discussions in the following sections.

### 5. 3.2. Reflectivity

The FESEM images for different samples are shown in **Fig. 2**, giving an insight into the plenty of nanoscale spatial features such as the nanoparticles, nanocavities, etc., along with hierarchical macro structures formed during the grove patterning of the laser. These images are taken after substantial time to allow the samples to undergo an oxidation process to form finer structures. Time evolution details are discussed in detail in a later section. These micros-nanostructures have large size distribution varying in the length scale of UV, visible, and near IR wavelength orders. These structures can act as cavities for the geometrical light trapping due to multiple reflections and possible coupling to the surface plasmons. By properly tuning the laser parameters for surface patterning, we could optimize to achieve the best anti-reflective nature of the surfaces.

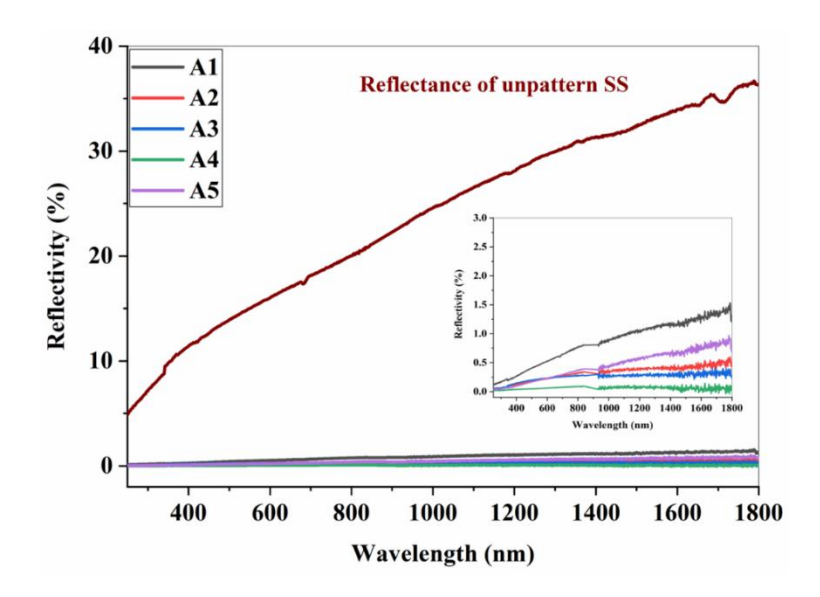
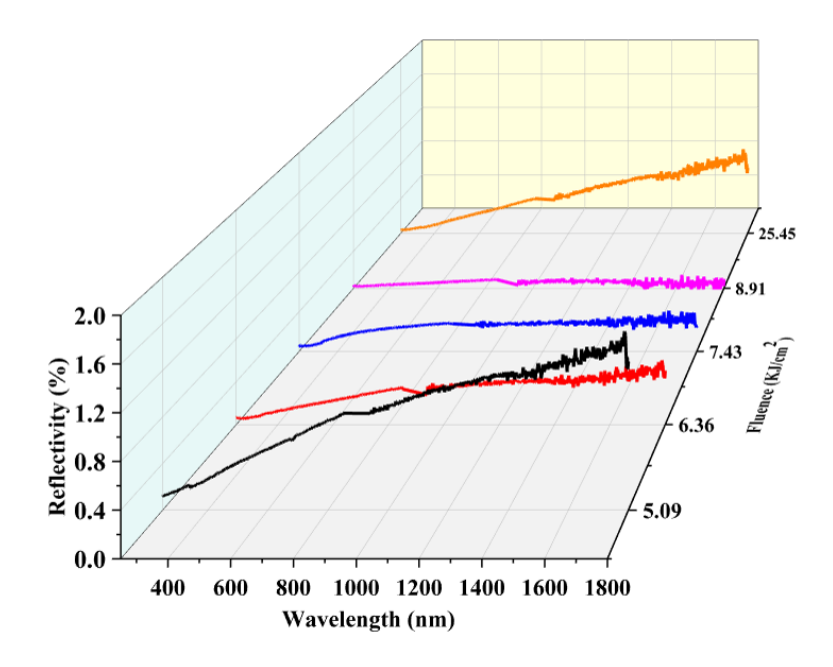


Fig. 3. The reflectivity of laser-irradiated stainless-steel surfaces. The wine-colored curve shows the reflectivity for the unirradiated surface in the main plot, whereas other curves show the reflectivity for the substrate irradiated with five different substrates A1, A2, A3, A4, A5, respectively, with corresponding color code. Inset shows the magnifying image for the reflectivity of nanostructured SS surfaces.

Reflectivity spectra have been taken individually for each patterned surface for several incidence angles for both S and P polarization for samples described in Table 1. The reflection spectra of polished SS surfaces have been shown in Fig. 3 as maximum values, along with reflectivity spectra of nanostructured stainless surfaces with different irradiation fluence at an incidence of 3.3°. From the figure, it is evident that the specular reflectivity from these surfaces is predominately decreased compared to the polish surface. Here we report, these surfaces are the best anti-reflection surfaces or highly absorbing nanostructured SS surfaces. The anti-reflectivity of the A4 sample achieved the best values over a broad wavelength range from 250 to 1800 nm; these are the lowest reflectivity values reported using laser ablation compared with the existing literature to the best of our knowledge. Over the entire broadband from 250 nm to 1800 nm, the reflectivity of the A4 sample is less than 0.14 %. This surface absorbs >99 % of the incident light at smaller wavelengths in the UV and visible region. As concluded from the earlier section, the A4 has the best surface morphological features for better trapping of the incident photons is also evident from Fig. 3. As discussed in the above section, the efficient trapping of the photons on the A4 sample is due to the nanoscale features.

#### **5.3.2.1.** Effect of pulse fluence



**Fig. 4.** The reflectivity of the nano-structured SS surface for the substrates A1, A2, A3, A4, and A5 (indicated by the color bar on the plot) for P polarized intensity of light at the incident angle of 3.3°.

Reflectivity spectra of nanostructured SS substrates are shown by **Fig. 4**, from UV to near IR (250-1800 nm), for different laser irradiating fluence values at a fixed angle of incidence 3.3°. One can notice that reflectivity decreases with laser fluence and then increases after optimum value. The three-dimensional figure, **Fig. 4**, shows the necessity to optimize the laser energy for achieving the best anti-reflection properties for a given material. These optimal values for laser energy could vary from material to material and depend on the pulse characteristics, which are beyond the scope of this article. As concluded from the earlier sections, the A4 laser fluence parameters are ideal for the antireflection properties.

#### 5.3.2.2. Effect of incidence angle

This section presents the reflectivity spectrum of the SS textures surface irradiated with optimized pulse fluence of 9.90 J/cm<sup>2</sup> (A4) for several angles of incidence to the surface normal. **Fig. 5** shows the reflectivity spectrum with 3.3°, 15°, 30°, 45°, 60°, and 75° incident angles for P polarized incident beam. The trend of the curves indicates that the

reflectivity coefficients increase as the incident angle increases. We also observed the higher reflectivity for the incident angle of 75 ° as compared to other reflectivities for the lower incident angle, which is according to the theory of Fresnel's coefficient of reflection. The reflectivity of the substrate A4 is efficient up to the incident angle of 45 °, which is less than 0.1%, and the values are much better for the range of 250-850 nm, which is less than 0.03 %. We conclude that for normal to 45 ° angle of incidence, there are hardly any reflections out of the surface; the surface is completely absorbing the incident light. At the higher wavelength range of 850 to 1800 nm, we observed more reflectivity where the surface features size distribution is going out of order of the incident wavelength.

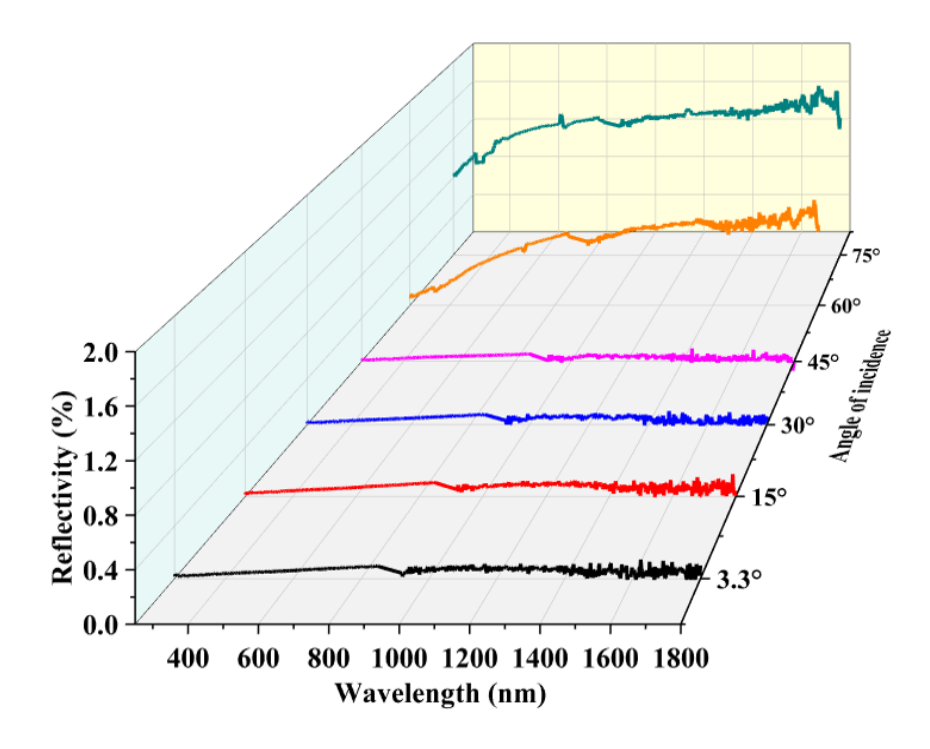


**Fig.5.** The reflectivity of the nano-structured SS surface at the incident angle of 3.3°, 15°, 30°, 45°, 60° and 75° for the substrate A4 as described in **Table 1** for P polarized incident beam.

# 5.3.2.3. Effect of incidence beam polarization

It is essential to understand the reflectivity of the sample with different polarizations. This section presents the reflectivity of S and P polarization for all the samples from A1 to A5, as shown in **Fig.6**. The solid line curves for the P polarization and the dashed lines for

the S polarization. For the samples A1 to A3 and A5, the S polarization is slightly higher than P polarization which could be coming due to the slight anisotropy of the surface during the laser grove patterning. However, for the optimized fluence values of A4 both S and P polarization are minimized indicating the patterned surface is behaving close to isotropic material in terms of surface reflectivity, which is ideal for the real-time applications where both S and P polarized lights are together incident on the surface.

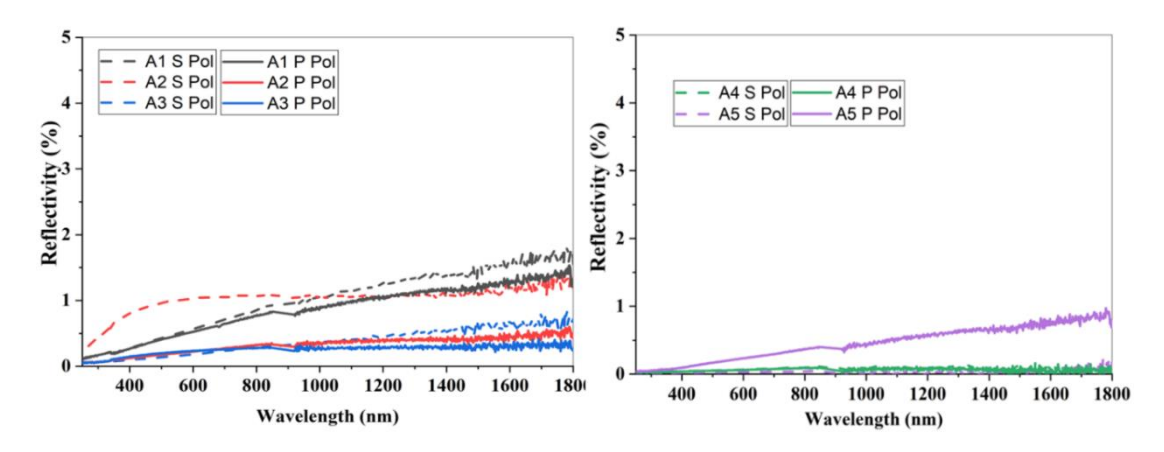
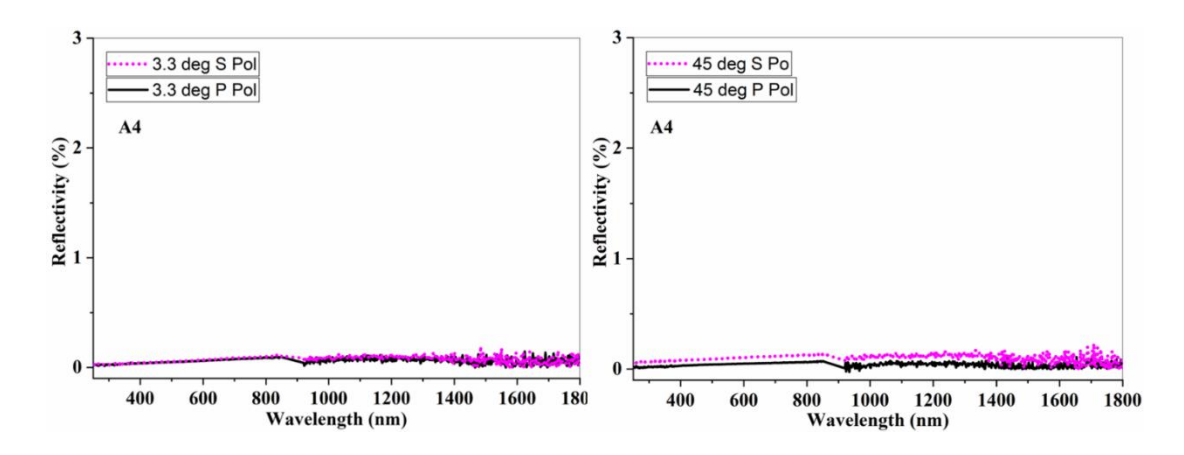


Fig. 6. The reflectivity of surface irradiated with a fluence of the substrates A1, A2, A3, A4, and A5 as per Table.1 S polarized and P polarized for the incident angle of 3.3°.

Fig. 5 investigated the reflectivity changes with incident angles for only P-polarized light. However, to compare the reflectivity of S and P polarization for different angles, we presented the reflectivity of the A4 sample in **Fig.7**. We presented the reflectivity curves at 3.3° and 45° incident angles in these two graphs. At a lower angle of incidence, there is no difference in the S and P polarization reflectivity, but at a 45° angle of incidence, the surface shows a very minute difference in the S and P polarizations. This difference can be neglected for real-time applications.



*Fig. 7.* Differential Reflectivity of the nano-structured SS surface at the incident angle of 3.3° and 45° for the substrate A4 for P polarized incidence beam.

#### 5. 3. 3. Elemental distribution

Upon irradiation of pulsed laser on the material surface, the materials get ablated in the laser track and redeposit the metallic particles in the adjacent areas. In this process, surface nanostructure features formation occurs rapidly, and as a result, the surface area increases in different morphological features, as discussed in earlier sections. In this section, we are investigating how the elemental composition changes or distributing on the SS. Also, after the time evolution by oxidation of the surface, how the elemental distribution changes and leads to unique features formation. To purview this, we took EDX (energy-dispersive X-ray) analysis on the FESEM images, inside the laserirradiated grooves, and in the peripheral area surface as shown in the 1st and 2nd row of Fig. 8, respectively and compared with the unpatterned surface shown in the third row of Fig.8. The weight percentage of the elements present in the laser-irradiated surface is depicted in Table 2. The elements are distributed over the different regions of the irradiation are presented in the elemental distribution micrograph along with the electron micrograph and mix spectrum in Fig. 8. We have noticed that the percentage of elemental weight is quite different within the two different regions of the substrate compared with the unpatterned surface. There is a significant weight percentage of the oxygen inside the grooves (22.9%) and peripheral area of the grooves (16.84%) compared with the unpatterned surface with mere 5.5% oxygen. Therefore, the oxidation rate is not the same throughout the microscopic area, and it is obvious because of groove depth and the surface area.

	Table 2. The wei	ght percentage of elemen	nts presents at the lase	er-irradiated surface.
--	------------------	--------------------------	--------------------------	------------------------

Elements	Weight percentage (Inside the grove)	Weight percentage (Peripheral area)	unpatterned surface
O (Oxygen)	22.9	16.84	5.15
Fe (Iron)	55.39	61.65	65.15
Cr (Chromium)	11.24	13.01	19.7
Mn (Manganese)	9.68	7.79	9
Si (Silicon)	0.79	0.71	1

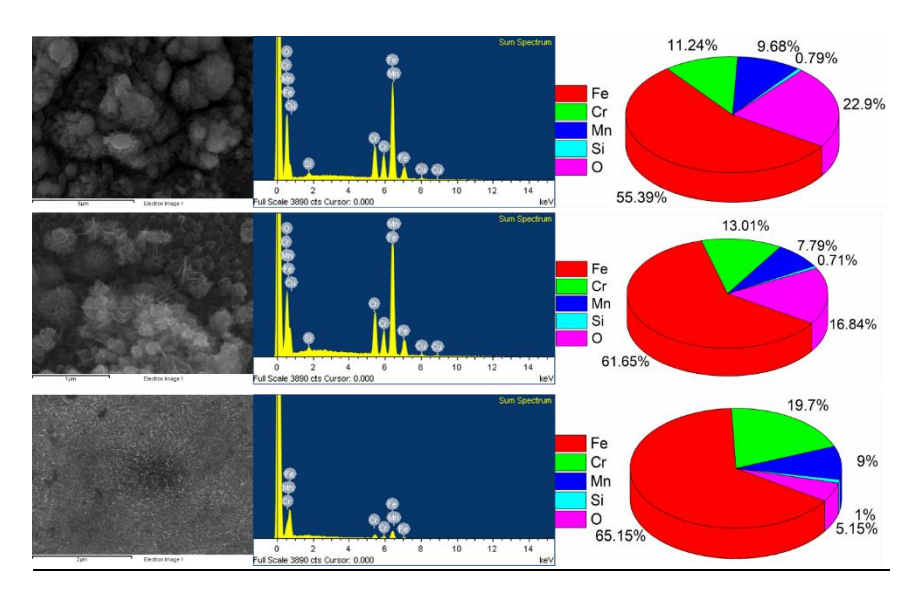


Fig. 8. Elemental analysis using dispersive energy X-ray (EDX) on FESEM images.  $1^{st}$  row: elemental distribution inside the focused laser beam,  $2^{nd}$  row: Elemental distribution on the peripheral area of laser scanning lines, and  $3^{rd}$  row: elemental distribution of the unpatterned SS substrates.

Upon further scrutiny, one can find the presence of the other compositional elements (Fe, Cr, Mn, and Si). Their percentage weight of presence is 61.65%, 13.01%, 7.79% and 0.71% and 56.39%, 11.24%, 9.08% and 0.79% peripheral area and inside the grooves respectively. One has to understand the crystal structure of these elements for further analysis, which is beyond the scope of this work. The reason behind the different weight percentages of elements is may be the fact that during the interaction of high intensity focused laser pulse and the material's surface, the efficiency of materials being

redistributed is different for different elements [47]. In other words, the threshold for material removal is different for different elements for a given laser fluence at the same ambient condition. This analysis can conclude that the oxygen percentage is quite different from unpatterned and patterned surfaces.

# 5.3.4. X-ray diffraction analysis

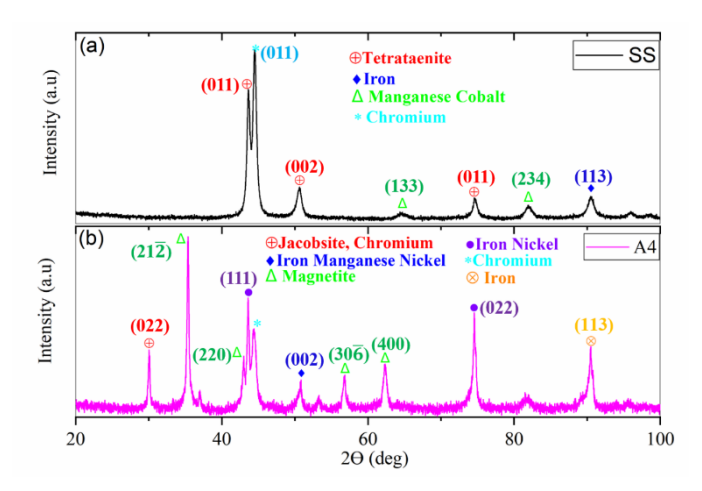


Fig. 9. X-ray Diffraction patterns of (a) unpatterned SS surface displaying four crystalline phases of Tetrataenite (Fe<sub>1</sub>Ni<sub>3</sub>, Tetragonal), Manganese Cobalt (Co<sub>0.15</sub>Mn<sub>0.85</sub>), Iron (Fe<sub>1</sub>, Cubic,) and Chromium (Cr<sub>1</sub>, Cubic)) and (b) nanosecond laser irradiated SS surface displaying five crystalline phases of Jacobsite, Chromium (Cr<sub>0.5</sub>Fe<sub>1.5</sub>Mn<sub>1</sub>O<sub>4</sub>, Cubic), Iron Manganese Nickel (Fe<sub>0.5</sub>Mn<sub>0.2</sub>Ni<sub>0.3</sub> Cubic), Magnetite (Fe<sub>3</sub>O<sub>4</sub>, Monoclinic), Iron Nickel (Fe<sub>3</sub>Ni<sub>1</sub>, Cubic) and Chromium (Cr<sub>1</sub>, Tetragonal). Different peaks are marked with the miller indexes and the phases present by different colors and symbols.

X-ray diffraction analysis of unpatterned and nanostructured SS (A4) substrates was carried out using a commercial XRD instrument (X'pert PANalytical) with Cu source  $K_{\alpha 1} = 1.540598 \ \dot{A}$ . We observe two important aspects: (1) The unpattern specimen shows broad features compared to the irradiated sample, and when analyzed through the Debye-Scherrer formula, the corresponding widths are found to be  $16\pm1.7 \ \text{nm}$  and  $39\pm3.0 \ \text{nm}$  average size approximately; (2) Few new peaks appear indicating the formation of nanocrystals of the alloys. These peaks have been identified and indicated in **Fig. 9**.

**Fig. 9(a)** shows the unpatterned SS comprised of four phases, viz.: Tetrataenite (Fe<sub>1</sub>Ni<sub>3</sub>, Tetragonal), Manganese Cobalt (Co<sub>0.15</sub>Mn<sub>0.85</sub>), Iron (Fe<sub>1</sub>, Cubic,) and Chromium (Cr<sub>1</sub>, Cubic) and the peaks of the corresponding phases are identified with cross-reference

number ICSD: 190821, ICSD: 163415, ICSD: 185754 and ICSD: 426936 respectively which are available in X'Pert HighScore Plus software. From **Fig. 9(b)**, one can notice a few extra peaks in the x-ray diffraction of the nanostructured stainless-steel surface. There are the compositional changes induced due to high-intensity laser pulses (fluence 9.90 J/cm²). Jacobsite, Chromium (Cr<sub>0.5</sub>Fe<sub>1.5</sub>Mn<sub>1</sub>O<sub>4</sub>, Cubic), Iron Manganese Nickel (Fe<sub>0.5</sub>Mn<sub>0.2</sub>Ni<sub>0.3</sub> Cubic), Magnetite (Fe<sub>3</sub>O<sub>4</sub>, Monoclinic), Iron Nickel (Fe<sub>3</sub>Ni<sub>1</sub>, Cubic), and Chromium (Cr<sub>1</sub>, Tetragonal) phases have appeared newly on the nanostructured surface. The corresponding cross-reference numbers to identify the peaks of the phases present are ICSD: 44409, ICSD: 103522, ICSD: 164814, ICSD: 188233, and ICSD: 625712, respectively. All the diffracted peaks are marked with the miller indices and the phases present by different colors and symbols in **Fig. 9**. The average crystallite sizes using Debye-Scherrer equation of unpatterned and nanostructured stainless-steel surfaces are found to be 16±1.7 nm and 39±3.0 nm, respectively which is in good agreement with FESEM images. Nanostructure nucleation growth with time is beyond the scope of the current work.

# 5. 3.5. Evolution of surface morphology over time

After the laser irradiation, the surface area of the substrate increases due to ablation and redisposition of the particles. The newly formed surface properties are quite different from the bulk material. We observed their ability to oxidize is extremely high, and these structures evolve with time to form fascinating structures under ambient atmospheric conditions. During this process, their antireflection properties do get enhanced. To understand these aspects, we present our investigation of the samples fabricated using the laser parameters of A4.

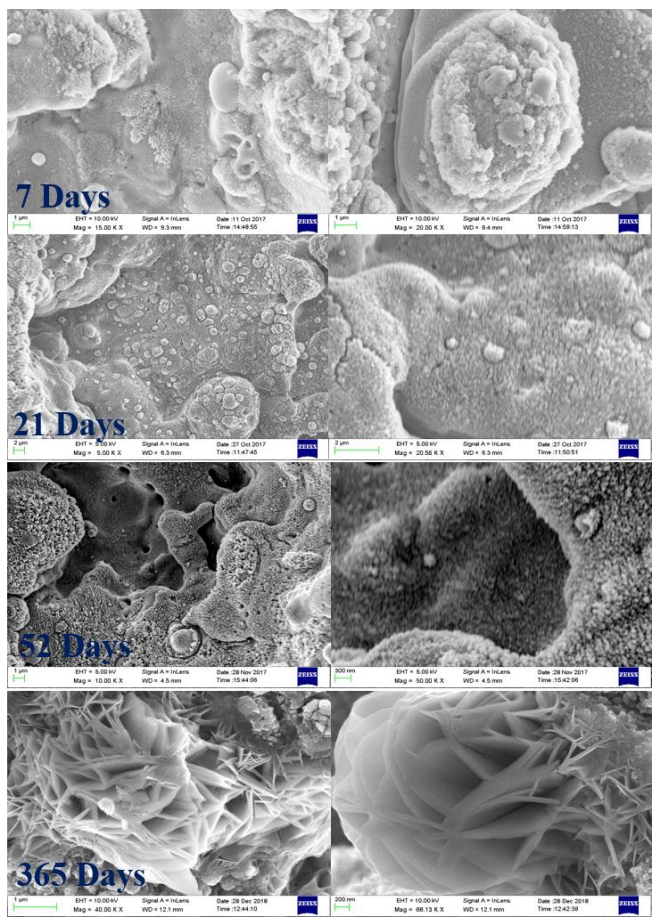


Fig. 10. Evolution of the micro and nanostructures on the SS surface for the first 7, 21, 52, and 365 days presented in each row, respectively.

**Fig. 10** presents the FESEM images of micro-nano structuredA4 samples after 7, 21, 52, and 365 days in each row, respectively. Immediately after the laser ablation, there are no fine structures on the samples, which are efficient in trapping the photons. From the second row of **Fig. 10**, the fine nanostructures just started evolving. After giving sufficient time, about 50 days, one can visually see the eruption of nanostructures on the surface of the SS substrate. Their reflectance properties get much better within the 50 days' time, as evident from **Fig. 11** and **Fig.12**. These figures show the evolution of reflectivity with time. After a year, the microscopic surface morphology gets completely changes. One can observe much efficient nano-flower-like cavities on a micro-scale if one allows the surface to oxidize over a year; refer to the last row of **Fig. 10**. The main underlying reason

behind the composite micro-nanoscopic surface morphology change can be due to slow oxidation processes occurring over time [48].

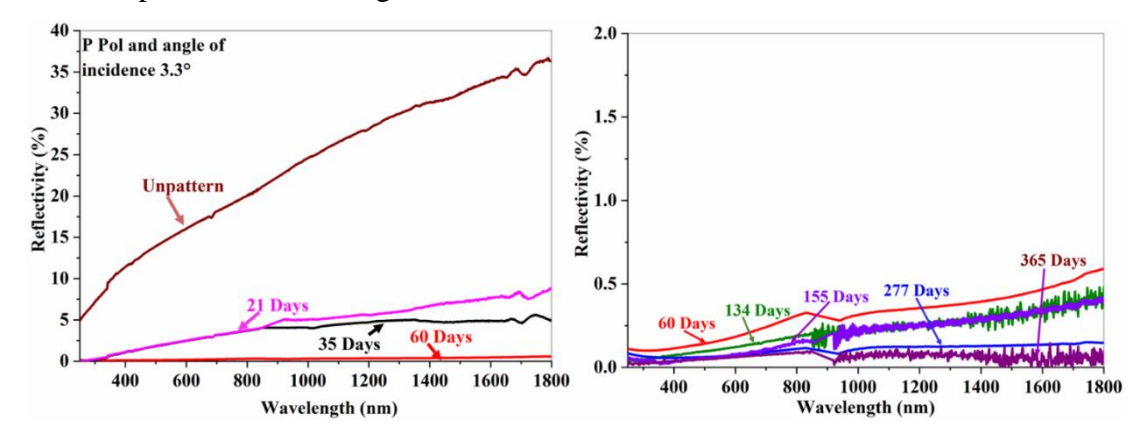
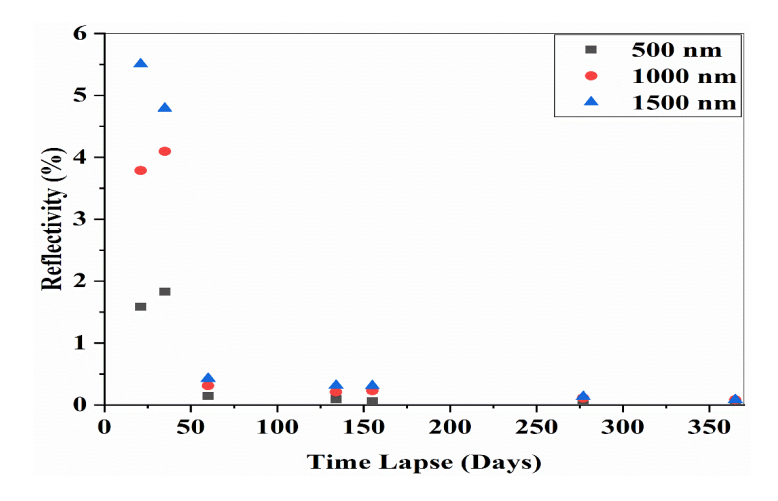


Fig. 11. Evolution of the reflectivity with a period (in days). Left plot: comparison of the reflectivity of unpatterned (Solid wine curve) SS surfaces with nanosecond patterned surface of A4 substrate with time evolution depicted for the first 60 days. The right plot shows the evolution from 60 days to year with a much-reduced y-axis scale. All the reflectivity measurements have been taken at an incident beam angle of 3.3° and a P polarized beam.

The FESEM images at different times give a clue that the surface can effectively trap the incident photons on it by multiple reflections like a cavity. As anticipated, the reflection patterns change drastically with time, as shown in the first picture of **Fig. 11**. The surface evolves very fast in the first 60 days to reach its overall reflectivity under 0.5% over the entire broad wavelength region. By further allowing the surface to oxidize, the reflectance gets further reduced with time. We presented the data for one year of evolution in **Fig.11**. These surfaces are highly stable with time, and they are better in their properties. One can further see how the reflectivity decrease with oxidation for three particular wavelengths from **Fig. 12**, presented for 500 nm, 1000 nm, and 1500 nm. The visible part reaches 99.9

% absorption within two months of oxidation, but the substrate takes a little longer for higher wavelengths to be super-efficient.



**Fig. 12.** Time evolution of the reflectivity of the substrate A4 for different wavelengths. The presented data is taken on 21, 35, 60, 134 155, 277, and 365 days, respectively. The complete analysis we presented in the above sections was done during 277 days.

#### 5. 4. Conclusions

We showed that nanosecond pulse laser irradiation enables the formation of composite micro-nano hierarchical surface structures and the surface appears completely black after laser patterning. By laser irradiation, surface nanostructure formed on the surface will increase the area compared to the bare polished SS surface. This study shows that the nanosecond pulse laser irradiation can be used as a scientific tool to create peculiar types of features such as superfine rods and flowers structure with appropriate control of laser fluence. We could achieve the near-complete absorption of the surfaces 99.9 % over a broad wavelength region covering UV, visible, and near IR. These surfaces are very efficient antireflection over a wide angle of incidence ±75 ° to the normal. Also, the optimized surfaces are isotropic for both S and P polarizations, ideal for solar illumination optical systems. We achieved less than 0.14% surface reflectivity in the visible range (250-850 nm) and less than 0.5 % in the infrared region (900-1800 nm). These robust pulsed textured metal surfaces show extremely low reflection and find application as super absorbers of light in many optical devices, space applications, lowlight imaging, etc.

#### References

- [1] Xi J Q, Schubert M F, Kim J K, Schubert E F, Chen M, Lin S Y, Liu W and Smart J A 2007 Optical thin-film materials with low refractive index for broadband elimination of Fresnel reflection *Nat. Photonics* **1** 176–9.
- [2] Kats M A, Blanchard R, Genevet P and Capasso F 2013 Nanometre optical coatings based on strong interference effects in highly absorbing media *Nat. Mater.* **12** 20–4.
- [3] Liu N, Mesch M, Weiss T, Hentschel M and Giessen H 2010 Infrared perfect absorber and its application as plasmonic sensor *Nano Lett.* **10** 2342–8.
- [4] Raut H K, Ganesh V A, Nair A S and Ramakrishna S 2011 Anti-reflective coatings: A critical, in-depth review *Energy Environ. Sci.* **4** 3779–804.
- [5] Lee Y J, Ruby D S, Peters D W, McKenzie B B and Hsu J W P 2008 ZnO nanostructures as efficient antireflection layers in solar cells *Nano Lett.* **8** 1501–5.
- [6] Leem J W, Song Y M and Yu J S 2011 Broadband antireflective germanium surfaces based on subwavelength structures for photovoltaic cell applications *Opt. Express* **19** 26308.
- [7] Ng C, Yap L W, Roberts A, Cheng W and Gómez D E 2017 Black Gold: Broadband, High Absorption of Visible Light for Photochemical Systems *Adv. Funct. Mater.* 27.
- [8] Makableh Y F, Al-Fandi M, Khasawneh M and Tavares C J 2018 Comprehensive design analysis of ZnO anti-reflection nanostructures for Si solar cells *Superlattices Microstruct.* **124** 1–9.
- [9] Jeong H J, Kim Y C, Lee S K, Yun J H and Jang J H 2019 Enhanced spectral response of CIGS solar cells with anti-reflective subwavelength structures and quantum dots *Sol. Energy Mater. Sol. Cells* **194** 177–83.
- [10] Ichon P I P, Arbet A D B, Lanchot J E A N H B, Ruon F R D, Alembois F R B and Eorges P A G 2018 Light-emitting diodes: a new paradigm for Ti: sapphire

- pumping 5.
- [11] Mahani F F and Mokhtari A 2018 TiO 2 Circular Nano-Gratings as Anti-Reflective Coatings and Potential Color Filters for Efficient Organic Solar Cells *J. Nanoelectron. Optoelectron.* **13** 1624–9.
- [12] Stavenga D G, Foletti S, Palasantzas G and Arikawa K 2006 Light on the motheye corneal nipple array of butterflies *Proc. R. Soc. B Biol. Sci.* **273** 661–7.
- [13] Ji S, Song K, Nguyen T B, Kim N and Lim H 2013 Optimal moth eye nanostructure array on transparent glass towards broadband antireflection *ACS Appl. Mater. Interfaces* 5 10731–7.
- [14] Han Z W, Wang Z, Feng X M, Li B, Mu Z Z, Zhang J Q, Niu S C and Ren L Q 2016 Antireflective surface inspired from biology: A review *Biosurface and Biotribology* 2 137–50.
- [15] Rephaeli E and Fan S 2008 Tungsten black absorber for solar light with wide angular operation range *Appl. Phys. Lett.* **92** 1–4.
- [16] Zhu J, Yu Z, Burkhart G F, Hsu C M, Connor S T, Xu Y, Wang Q, McGehee M, Fan S and Cui Y 2009 Optical absorption enhancement in amorphous silicon nanowire and nanocone arrays *Nano Lett.* **9** 279–82.
- [17] Diedenhofen S L, Vecchi G, Algra R E, Hartsuiker A, Muskens O L, Immink G, Bakkers E P A M, Vos W L and Rivas J G 2009 Broad-band and omnidirectional antireflection coatings based on semiconductor nanorods *Adv. Mater.* **21** 973–8.
- [18] Zhang S, Li Y, Feng G, Zhu B, Xiao S, Zhou L and Zhao L 2011 Strong infrared absorber: surface-microstructured Au film replicated from black silicon *Opt. Express* **19** 20462.
- [19] Landy N I, Sajuyigbe S, Mock J J, Smith D R and Padilla W J 2008 Perfect metamaterial absorber *Phys. Rev. Lett.* **100** 1–4.
- [20] Teperik T V., García De Abajo F J, Borisov A G, Abdelsalam M, Bartlett P N, Sugawara Y and Baumberg J J 2008 Omnidirectional absorption in nanostructured metal surfaces *Nat. Photonics* **2** 299–301.
- [21] Yao Y, Yao J, Narasimhan V K, Ruan Z, Xie C, Fan S and Cui Y 2012 Broadband light management using low-Q whispering gallery modes in spherical nanoshells

- *Nat. Commun.* **3** 664–7.
- [22] Letsou T, ElKabbash M, Iram S, Hinczewski M and Strangi G 2019 Heat-induced perfect light absorption in thin-film metasurfaces for structural coloring [Invited] *Opt. Mater. Express* **9** 1386.
- [23] Tan H, Santbergen R, Smets A H M and Zeman M 2012 Plasmonic light trapping in thin-film silicon solar cells with improved self-assembled silver nanoparticles *Nano Lett.* **12** 4070–6.
- [24] Fang Z and Zhu X 2013 Plasmonics in nanostructures *Adv. Mater.* **25** 3840–56.
- [25] Lee S K, Tan C L, Ju G W, Song J H, Yeo C II and Lee Y T 2015 AuAg bimetallic nonalloyed nanoparticles on a periodically nanostructured GaAs substrate for enhancing light trapping *Opt. Lett.* **40** 5798.
- [26] Baryshnikova K V., Petrov M I, Babicheva V E and Belov P A 2016 Plasmonic and silicon spherical nanoparticle antireflective coatings *Sci. Rep.* **6** 1–11.
- [27] Tan C L, Jang S J and Lee Y T 2012 Localized surface plasmon resonance with broadband ultralow reflectivity from metal nanoparticles on glass and silicon subwavelength structures *Opt. Express* **20** 17448.
- [28] Fan P, Bai B, Long J, Jiang D, Jin G, Zhang H and Zhong M 2015 Broadband High-Performance Infrared Antireflection Nanowires Facilely Grown on Ultrafast Laser Structured Cu Surface *Nano Lett.* **15** 5988–94.
- [29] Fan P, Bai B, Jin G, Zhang H and Zhong M 2018 Patternable fabrication of hyperhierarchical metal surface structures for ultrabroadband antireflection and self-cleaning *Appl. Surf. Sci.* **457** 991–9.
- [30] Vorobyev A Y and Guo C 2011 Direct creation of black silicon using femtosecond laser pulses *Appl. Surf. Sci.* **257** 7291–4.
- [31] Tang G, Hourd A C and Abdolvand A 2012 Nanosecond pulsed laser blackening of copper *Appl. Phys. Lett.* **101.**
- [32] Vorobyev A Y and Guo C 2008 Femtosecond laser blackening of platinum *J. Appl. Phys.* **104** 1–5.
- [33] Caizhen Y, Yayun Y, Baoshen J, Yuan L, Renjie D, Yong J, Yuxin W and Xiaodong Y 2017 Polarization and fluence effects in femtosecond laser induced

- micro/nano structures on stainless steel with antireflection property *Appl. Surf. Sci.* **425** 1118–24.
- [34] Fan P, Zhong M, Li L, Schmitz P, Lin C, Long J and Zhang H 2014 Angle-independent colorization of copper surfaces by simultaneous generation of picosecond-laser-induced nanostructures and redeposited nanoparticles *J. Appl. Phys.* 115.
- [35] Cui K, Wardle B L and Wardle B L 2019 Breakdown of Native Oxide Enables Multifunctional, Free-Form Carbon Nanotube–Metal Hierarchical Architectures *ACS Appl. Mater. Interfaces* **11** 35212–20.
- [36] Fan P, Bai B, Jin G, Zhang H and Zhong M 2018 Patternable fabrication of hyper-hierarchical metal surface structures forultrabroadband antireflection and self-cleanining Appl. Surf. Sci. **457** 991-999.
- [37] Taher M A, Prasad H, Krishnan P K N, Naraharisetty S R G and Desai N R 2019 Ellipsoidal droplet formation on anisotropic superhydrophobic copper surface Ellipsoidal droplet formation on anisotropic superhydrophobic copper surface Surf. Topogr. Metrol. Prop. 7 035001.
- [38] Dar M H, Saad N A, Sahoo C, Naraharisetty S R G and Desai N R 2017 Ultrafast laser-induced reproducible nano-gratings on a molybdenum surface *Laser Phys. Lett.* **14.**
- [39] Dar M H, Kuladeep R, Saikiran V and Rao N D 2016 Femtosecond laser nanostructuring of titanium metal towards fabrication of low-reflective surfaces over broad wavelength range *Appl. Surf. Sci.* **371** 479–87.
- [40] Huang H, Yang L-M, Bai S and Liu J 2015 Blackening of metals using femtosecond fiber laser *Appl. Opt.* **54** 324.
- [41] You A, Be M A Y and In I 2015 Enhanced absorption of metals over ultrabroad electromagnetic spectrum **121106**.
- [42] Fan P, Zhong M, Li L, Huang T and Zhang H 2013 Rapid fabrication of surface micro/nano structures with enhanced broadband absorption on Cu by picosecond laser *Opt. Express* **21** 11628.
- [43] Fan P, Zhong M, Bai B, Jin G and Zhang H 2015 Tuning the optical reflection

- property of metal surfaces via micro-nano particle structures fabricated by ultrafast laser *Appl. Surf. Sci.* **359** 7–13.
- [44] Liu H, Lin W and Hong M 2019 Surface coloring by laser irradiation of solid substrates *APL Photonics* **4.**
- [45] Samanta A, Wang Q, Singh G, Shaw S K, Toor F, Ratner A and Ding H 2019 Nanosecond Pulsed Laser Processing Turns Engineering Metal Alloys Antireflective and Superwicking 47th SME North Am. Manuf. Res. Conf. NAMRC 47 34 260–8.
- [46] Fu J, Liang H, Zhang J, Wang Y, Liu Y and Zhang Z 2017 Enhanced optical absorbance and fabrication of periodic arrays on nickel surface using nanosecond laser *Opt. Commun.* **389** 170–5.
- [47] Russo R E, Mao X and Mao S S 2008 Peer Reviewed: The Physics of Laser Ablation in Microchemical Analysis *Anal. Chem.* **74** 70 A-77 A.
- [48] He A, Liu W, Xue W, Yang H and Cao Y 2018 Nanosecond laser ablated copper superhydrophobic surface with tunable ultrahigh adhesion and its renewability with low temperature annealing *Appl. Surf. Sci.* **434** 120–5.

# Chapter 6

# Anisotropic non-wetting metallic surfaces: triple contact line theory approach

#### Abstract

The anisotropic droplet formulation is generalized from hydrophilic to superhydrophobic surfaces. An experimental approach for calibrating the ellipsoidal droplet volume is described on both hydrophilic and hydrophobic surfaces. Using femtosecond laser patterning, a wide range of contact angles of the ellipsoidal droplets are achieved on copper and stainless-steel surfaces. On establishing anisotropic contact angles, the impacts of line spacing between laser scanning are addressed. The evolution of anisotropic contact angles and the spreading dynamics of droplets are investigated on both metallic surfaces. According to the Triple Contact Line (TCL) theory, contact angles are determined by the triple contact line between droplet and surface rather than the contact area. We demonstrated the mathematical formalism and experimental validity of the TCL theory over a broad range of contact angles on ellipsoidal droplets, from 37° to 172°.

#### 6.1. Introduction

A liquid droplet on an isotropic surface takes the form of a spherical droplet, with contact angles (CAs) depending on the surface properties. As the surface roughness increases, the CA can behave as a superhydrophobic surface if the CAs are greater than 150°. Water droplet rolls off on these surfaces with little disturbance, and this kind of behavior is called the "lotus leaf effect." Nature made this kind of surface for self-cleaning applications in plant leaves, flower petals, gecko pads, insect wings, legs [1–4]. The ability to mimic these surfaces has been exhibited on a variety of surfaces, notably ZnO nanorods [5], metallic surfaces [6–8], polymers [9], semiconductors [10], etc. Wenzel [11] and Cassie- Baxter models[12,13]intensively refer to liquid wetting behavior on twodimensional symmetric surfaces. According to the Wenzel model, a liquid droplet penetrates the surface's micro-cavities. In the Cassie-Baxter model, an intermediate interface is filled with air between the water droplet and substrate; the air in the surface valleys suspends liquid droplets. Some intermediate models in which droplets will be partially in the Cassie state and partially in the Wenzel state [14–16]. These models suggest that CAs are influenced by surface roughness. However, the contact angle formation is a one-dimensional problem suggested by D. C. Pease and demonstrated by Gao et al.[17]. According to Gao, the CA behavior (advancing, receding, and hysteresis) is solely governed by interactions between the liquid and the solid at the three-phase contact line, with the interfacial area within the contact perimeter being immaterial. H. Y. Erbil examines the dependence of contact angles on a three-phase contact line in detailed [18]. Liu looked further into Gao's investigations to examine the wetting behavior of spherical droplets[19]. This theoretical work relates the droplet's effective volume and contact angles, expressed in terms of physical dimensions/parameters of the triple contact

line of a spherical droplet. All of the references above are for isotropic surfaces with spherical drops. The formation of spherical sessile droplets on a smooth surface is far from feasible; instead, gravity pulls droplets to develop an ellipsoidal shape [20,21]. This paper formulates and experimentally validates the TCL model on asymmetric droplets over a broad range of CAs.

Because the laser-patterned surfaces are anisotropic, the droplet takes on an ellipsoidal rather than a spherical shape. Anisotropic droplet formation with lower CAs (< 150°) has been reported previously[22–28]. Anisotropic wetting characteristics on various materials have many potential advantages in manufacturing [29,30]. The study of longitudinal and transverse contact angles of a droplet on micro-grooved surfaces has gained immense attention to researchers due to its potential applications. Some of the areas of applications are movement dynamics[31], transporting droplets through the anisotropic surface[32], spreading dynamics of the ellipsoidal droplet[33], anisotropic flow behavior on corrugated semiconductor surface[34], sliding dynamics of the droplets on microgrooves[35], icephobicity[36], the controllable valve in microfluidics[30], photothermal control of micro fluids[37], directional anchoring of patterned superamphiphobic surfaces[38], droplet bouncing hydrodynamics[39], mechanoresponsive tuning[40], harvesting of dew droplets[41,42], etc.

In the literature, there are numerous approaches for artificially simulating superhydrophobic surfaces [43,44]. For these significant industrial applications, laser direct writing is widely used [45–49]. The production of superhydrophobic stainless steel and copper surfaces using femtosecond laser direct writing is demonstrated in this paper. These surfaces form anisotropic droplets with CAs as high as 172°.

Because of the parallel groove structures, the femtosecond laser patterned surface displays inherent asymmetry. The anisotropy of surface morphology has two orthogonal directions of geometry, along the line of laser writing (along the grooves) and orthogonal to the laser writing (perpendicular to the grooves). Higher CAs were observed in the orthogonal direction of laser grooves than CAs along the groove. Water droplets formed on these surfaces are not spherical; they get stretched in the groove direction because there is no barrier to liquid flow, but they are compressed in the perpendicular direction

owing to groove barriers [50,51]. In this analysis, we developed mathematical formalism to test this idea from hydrophilic to superhydrophobic surfaces. We could observe the droplets with CAs ranging from 37° to 172°, and we have taken these sessile droplet images for the volume estimation.

# **6.2. Experimental Procedure**

Femtosecond fiber laser (Satsuma HP2, Amplitude system) is used to surface processing on stainless steel (SS304) and copper (Cu) substrates. Its central wavelength is 1030 nm, with a pulse duration of 350 fs, and is operated at a 200 kHz fixed repetition rate. The substrate is mounted on a motorized XYZ stage (Newport), of which movement is controlled by an ESP motion controller (ESP300) for precise patterning with 1µm accuracy, as shown in **Fig. 1**. Laser patterning is performed in a raster fashion over the entire surface, as shown schematically in **Fig. 1(B)**, in the case of single scan substrates. For double scan substrates, a second scan is performed in the orthogonal direction to the first scan (this will overwrite the earlier scan). In the case of the double scan, the second scan direction is considered along the groove direction. The scanning speed of 4 mm/s is fixed in this work, and the area covered is 1.0 x 1.0 cm2 for all the substrates.

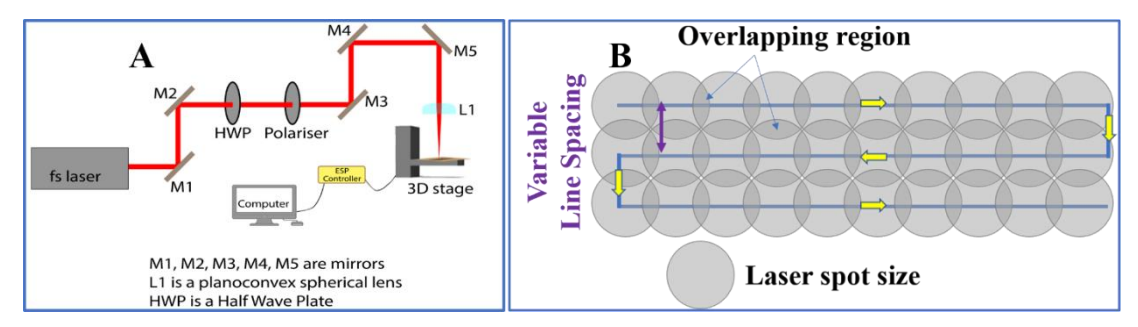


Fig. 1: Schematics of (A) laser direct writing setup and (B) periodic raster scanning processes.

We have used two different focal lengths of plano-convex lens to carry out two different kinds of investigation: one is for the fabrication of superhydrophobic surfaces and another for hydrophilic to superhydrophobic surfaces. The pulsed laser beam was focused using the plano-convex lens of 6 cm focal length. The estimated beam waist at the focus is  $26\pm1$  µm, while our incident laser beam diameter is  $3.5\pm1$  mm. Two different sets of fluence

values (1.2 J/cm<sup>2</sup> and 0.5 J/cm<sup>2</sup>) are used for laser direct only on copper substrates and are presented in **Table 1**. Two different sets of successive line spacing of 15 µm and 20 μm are employed during laser patterning for the single and double scan copper substrates. A plano-convex lens of 5 cm focal length is used to focus the laser pulses at the normal incidence on the substrate. The approximate spot diameter at the focus is 22±1 µm, with an input beam diameter of 3.5± 1 mm. Two different kinds of substrates, stainless steel (SS) and copper (Cu), were fabricated with line spacing from 15 µm to 60 µm at a fixed fluence of 1.3 J/cm2 and for each spacing in single and double scan modes (see **Table 2**). Substrates are ultrasonically cleaned in distilled water after irradiation treatments. As reported in the literature [43,44], these substrates change their wetting properties with time and become more stable. All droplet static contact angles presented in this work are made after the stabilization of the sample, and for statistics, measurements were performed several iterations after the stabilization. Surface morphological characterization of laser patterned surfaces was performed by FESEM (Zeiss Ultra) and atomic force microscope (AFM, VEECO diNanoscope V). One-dimensional root means square surface height deviation (1D RMS SHD) was analyzed using the Gwyddion software on AFM with a strip size of 0.4 µm by 94 µm. CA measurements were performed using home-built CA measurement equipment, as shown in Fig. 2A. This comprises a Canon EOS 700D camera positioned in the same plane as the water droplet-containing substrate. We took droplet pictures in two orthogonal directions for anisotropic CA measurements, keeping the camera positions at the same distance from the droplet lying on the substrates, as shown in Fig. 2A. For example, we provided one of the sets of CAs observed in Fig. 2B. The droplet-substrate system was illuminated with diffused source from the opposite side of the camera position for high contrast. Using the ImageJ software, the acquired image was processed and analyzed using an active contour-based method [45]. This approach, based on active contours, can accurately estimate CA with an error of less than 0.10 for a particular droplet formation.

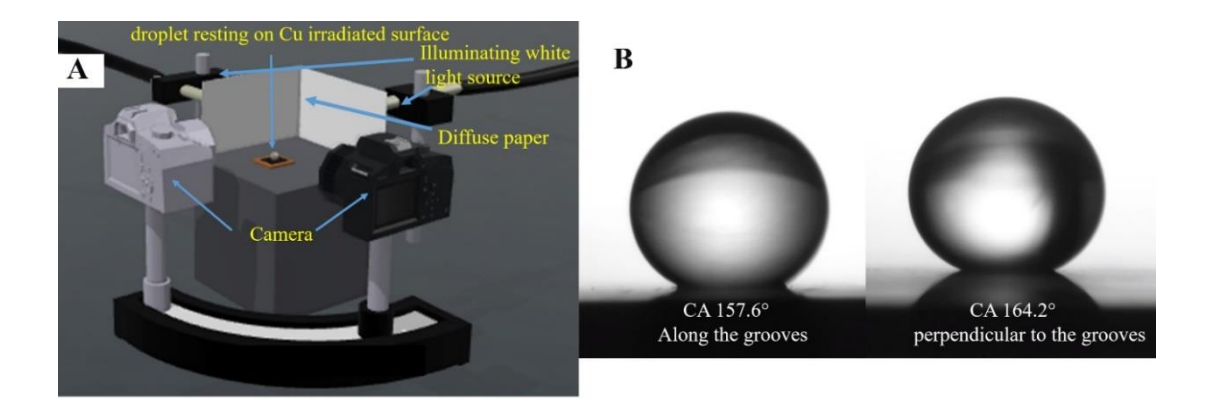


Fig. 2. A: Schematic home-built CA measurement set up. B: Droplets resting on the surface of substrate vi, one of the statistical sample data with the highest observed contact angle measurement, is presented.

# 6. 3. Results and Discussion

# 6. 3.1. TCL theory on superhydrophobic substrates

Six Cu substrates were patterned under different experimental conditions and their corresponding experimentally observed measurements are presented in **Table 1**. Laser fluence used for four substrates is  $1.2 \text{ J/cm}^2$  and for another two substrates,  $0.5 \text{ J/cm}^2$ , as shown in **Table 1**. CAs of the droplets on patterned substrates were measured and presented in **Table 1**,  $\theta_x$  &  $\theta_y$  are CAs along the groove and perpendicular to the groove, respectively. All the measurements were made in a static condition with a fixed volume of the water droplet of 5  $\mu$ L. Substrate (ii) and substrate (vi) showed CAs greater than  $150^\circ$  satisfying the criteria of superhydrophobic nature of the surface. These substrates were laser patterned at a higher laser fluence of  $1.2 \text{ Jcm}^{-2}$  using double scan or grid spacing of  $15 \mu$ m and  $20 \mu$ m, respectively. For substrate (vi), we observed the maximum CA of about  $164^\circ$  perpendicular to the grooves formed along the direction of the second scan, and in another orthogonal direction, measured CA was  $157^\circ$ , the schematic of CAs measurements is shown in **Fig. 2B**.

**Table 1:** Laser textured Cu substrates with different experimental conditions and CAs of the droplets on surfaces. The  $\theta_x$  and  $\theta_y$  are the CAs along the grooves and perpendicular to the grooves respectively and  $\Delta \theta = \theta_y - \theta_x$ . CAs and surface roughness parameters of the textured Cu surfaces with different experimental conditions.  $S_{q\parallel}$  and  $S_{q\perp}$  are the average of 1D slope along and perpendicular to the grooves on laser textured surface respectively and  $\Delta S_q = |S_{q\perp} - S_{q\parallel}|$ .

Subst rate	Fluence (J/cm²))	Spacing (µm) and scan type	CA (θ <sub>x</sub> ) degrees	CA (θ <sub>y</sub> ) degrees	Δθ degrees	S <sub>q⊥</sub> (nm)	S <sub>ql</sub> (nm)	ΔS <sub>q</sub> (nm)	Surface roughness Rq (nm)
i	1.18×10 <sup>3</sup>	15, Single scan	142.3±2.2	143.0±2.2	0.6±0.16	391.5	364.9	26.7	428
ii	1.18×10 <sup>3</sup>	15, Double scan	155.1±3.4	157.8±3.2	2.7±0.67	1036.0	537.9	498.6	931
iii	4.7 ×10 <sup>2</sup>	15, Single scan	119.4±2.2	120.9±2.2	1.5±0.22	239.0	180.3	88.7	273
iv	4.7 ×10 <sup>2</sup>	15, Double scan	134.5±2.1	136.0±2.2	1.5±0.05	716.5	500.0	216.5	777
V	1.18×10 <sup>3</sup>	20, Single scan	147.1±2.2	148.5±2.2	1.5±0.14	309.3	289.4	19.9	352
vi	1.18×10 <sup>3</sup>	20, Double scan	153.0±2.7	158.2±3.5	5.2±0.89	1713.1	414.2	1298.9	2109

The FESEM images of all the substrates (presented in **Table 1**) are shown in **Fig 3**. These pictures are presented in different scales to emphasize the different macroscopic and microscopic features. In **Fig. 3**, the first and second columns show the single scan and double scan images, respectively. The scales of inset images are chosen to emphasize particular secondary features that are forming for those experimental conditions. We could tune the CAs between  $115^{\circ}$  to  $164^{\circ}$  due to different primary and secondary microstructures forming under different experimental conditions, as shown in **Fig. 3**. The first and third rows of the images are for surfaces patterned with a common fluence of 1.2 J/cm<sup>2</sup> and spacing of 15  $\mu$ m and 20  $\mu$ m between successive laser scans, respectively. Images in the second row are patterned with a fluence of 0.47 J/cm<sup>2</sup> and 15  $\mu$ m successive line spacing. More prominent primary and secondary structures are forming at higher fluence and double scanning. One can observe that there are no proper grooves in the single scan images compared to the double scan, as shown in the first column of **Fig. 3**.

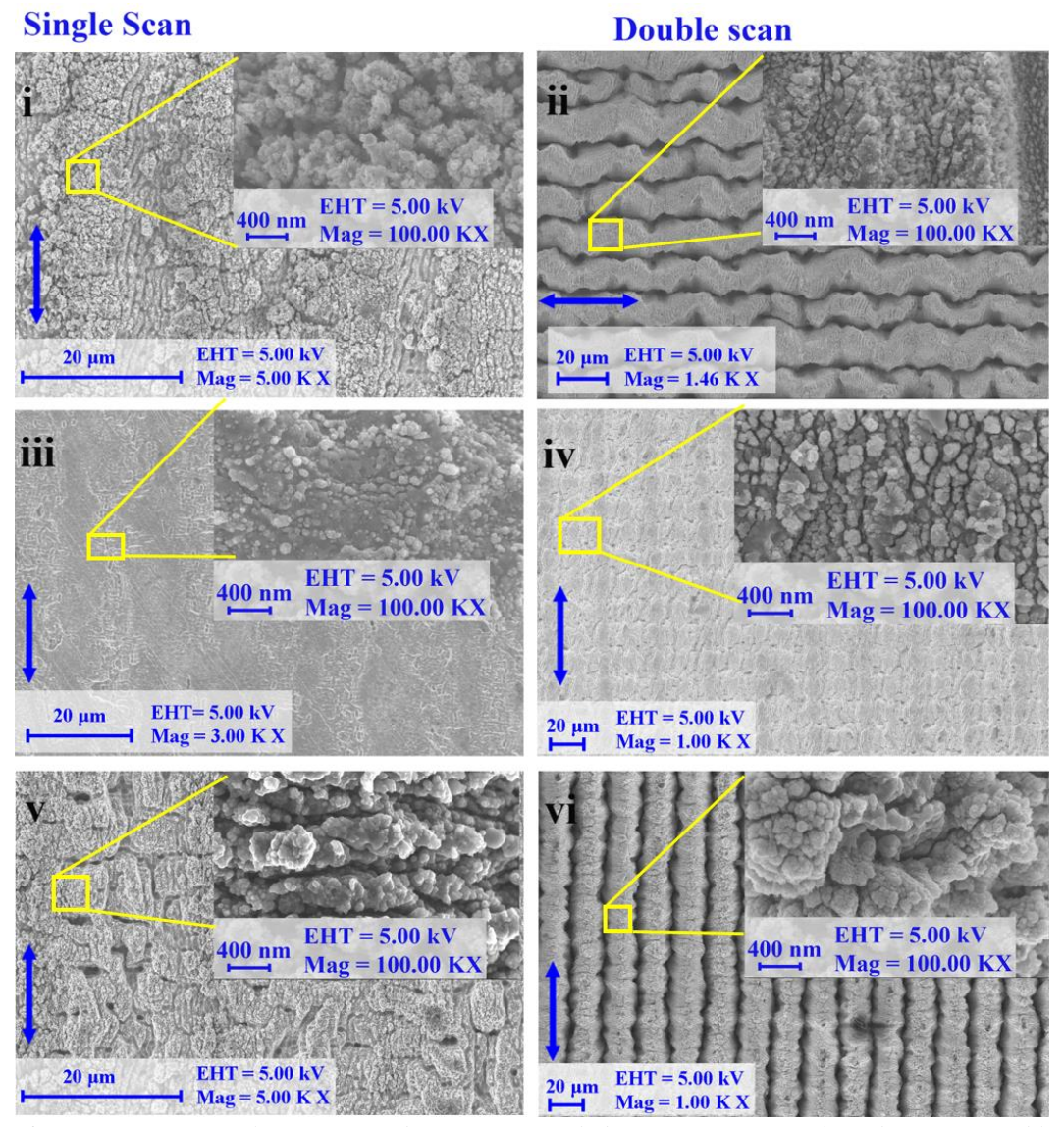


Fig. 3: FESEM images of laser patterned Cu surfaces with different experimental conditions (see Table 1). Images in the first column are for a single scan, and the second column is a double scan which is patterned orthogonal direction to the first scan. Blue arrows show the first and second scanning direction for single and double scans, respectively. Insets show surface morphology at a higher magnification (100 kX) corresponding to each substrate's surface. The bars are equal to 20 µm and 400 nm in the main and inset images, respectively.

It takes different elongations in different directions of the droplet, leading to an ellipsoidal shape formed approximately over a macroscopic contact diameter of 400  $\mu$ m. We present the corresponding CA measurements of the droplet in orthogonal directions in **Table 1**. When one compares the CAs and surface roughness of samples (iv) and (v) in Table 1, it

can be seen that higher roughness has a lower contact angle and vice versa. We are in the quest to find the correlation between the measured anisotropy CAs ( $\Delta\theta$ ) and other parameters that dictate the anisotropy. For further investigation, we performed a 3D surface profile of the substrates using AFM. These AFM images are presented in Fig. 4 in two columns similarly as explained in Fig. 3. AFM image data is further analyzed for a parameter to correlate the anisotropy,  $\Delta\theta$  of droplets. Our previous discussion of FESEM images shows that the larger the groove depth and better the secondary structures, the higher the observed CAs. These primary and secondary structures form peaks and valleys at different length scales. To quantify these peaks and valleys, we analyzed a onedimensional root mean square surface height deviations (1D RMS SHD) parameter. This parameter is measured from AFM data over a small area covering 0.4 µm width and 90 μm length, using Gwyddion software that gives the RMS variation over the selected region. A small selected strip is translated along the length of the substrate and obtained 1D RMS SHD values for each translation. The plots of the 1D RMS SHD vs. position of the substrates are presented in **Fig. 5**, for both cases where the one-dimensional translation strip is along the groove and across the groove.

For substrate (vi), where well-defined grooves are formed, as anticipated along the groove, the magnitude of 1D RMS SHD will be smaller, and this magnitude of variations gives insight about the secondary structures such as cauliflower structures as shown in the FESEM images. On the other hand, 1D RMS SHD magnitude for substrate (vi) will be large when translated perpendicular to the grooves; these are evident from the last plot of **Fig. 5**.

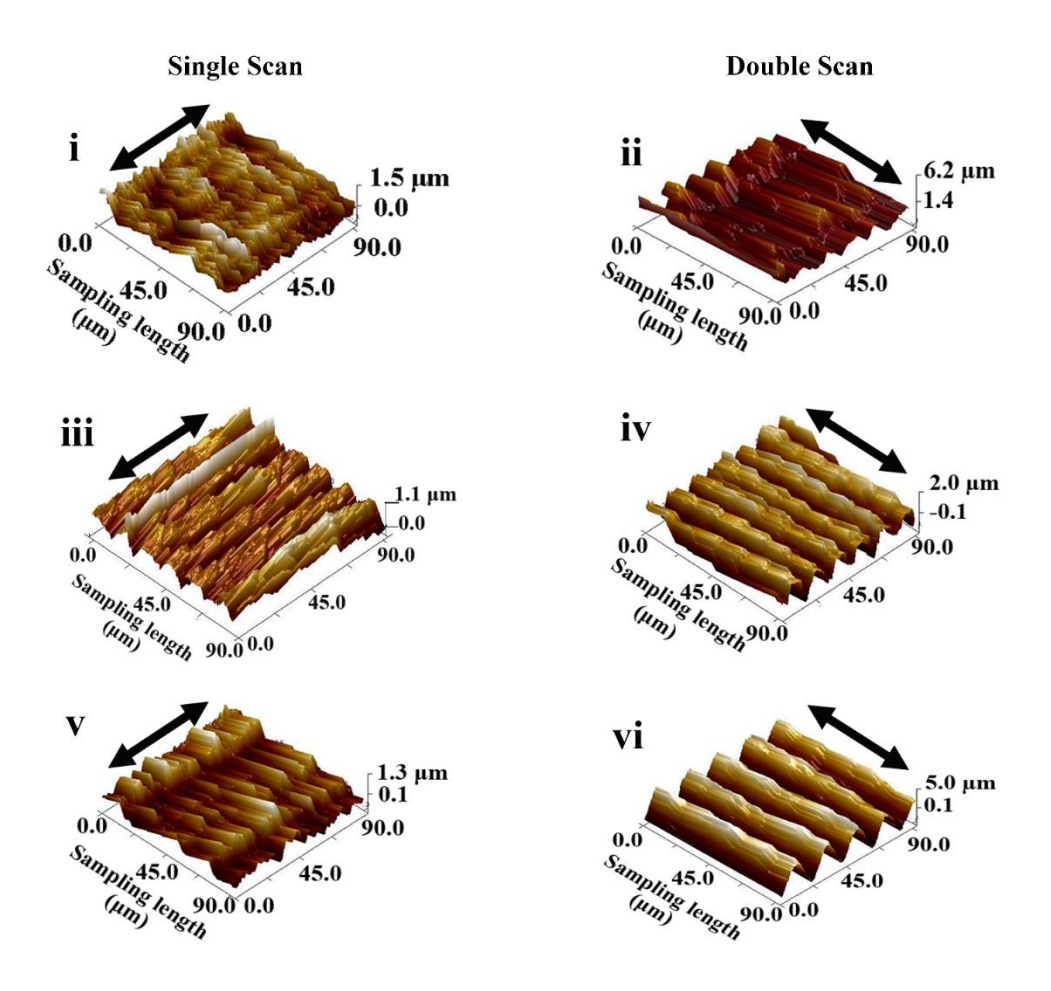


Fig. 4: AFM height sensor of laser patterned Cu surfaces with different irradiation parameters as shown in Table 1. Arrows show the first and second scanning directions in each image.

These higher 1D RMS SHD will also account for a higher barrier for the liquid flow and allow for better pinning of the boundary to exhibit the highest CAs on both directions for sample (vi). For the substrates (ii) and (vi), the groove depth is higher; hence, the 1D RMS SHD separation along the groove and across the groove is larger, as shown in **Fig.** 5. For other substrates, this difference is not large or equal, which essentially shows the surface is random rather than anisotropic. One has to pay attention to the magnitude of variation on the Y-axis scale, which gives an insight into how the secondary and primary structures are forming.

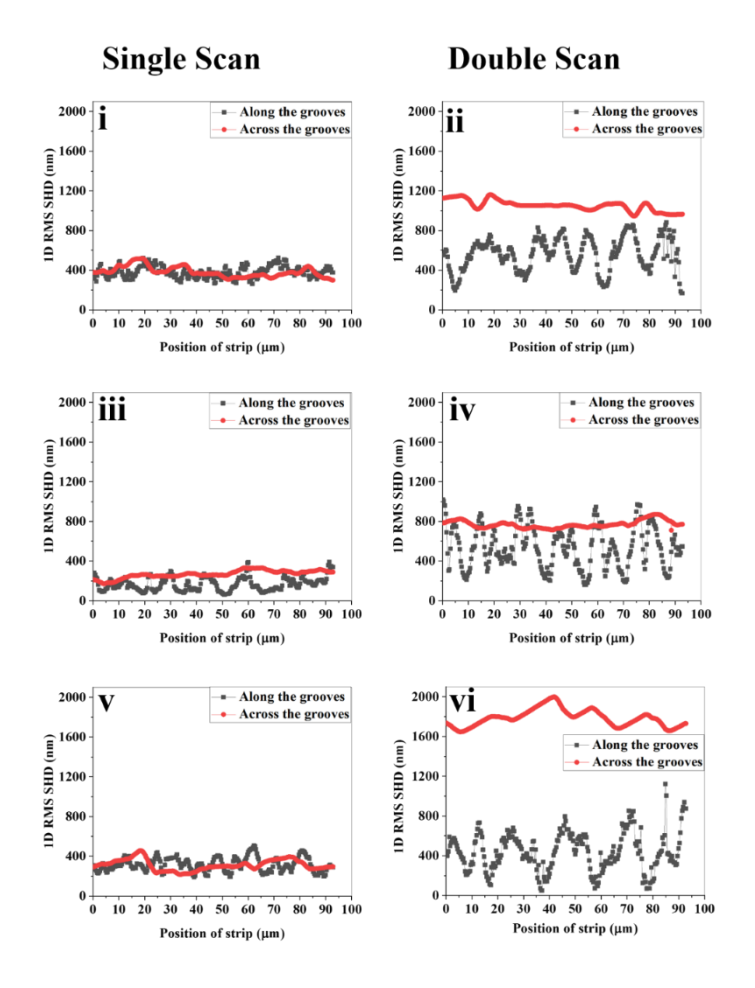


Fig. 5: 1D RMS SHD as a function of sample position over the laser patterned Cu surfaces with different sets of irradiation parameters along with two perpendicular directions. The first and second columns of plots are for single and double scan patterned surfaces, respectively.

To quantify this, we took an average value of the 1D RMS SHD for each substrate to give two values along the grooves  $(S_{q\parallel})$  and perpendicular to the grooves  $(S_{q\perp})$ . A parameter  $\Delta S_q = S_{q\perp}$ -  $S_{q\parallel}$ , defined as the difference of the 1D RMS SHD in the two orthogonal directions, was obtained for all the substrates [46]. The plot of  $\Delta S_q$  vs.  $\Delta \theta$ , from **Table 1** values, is shown in **Fig. 6**. The correlation value for the linear fit for  $\Delta S_q$  and anisotropy in CAs  $\Delta \theta$  is found to be 0.98; this parameter predicts the anisotropy to the best accuracy. Also, from **Table 1**, it is clear that the droplet assumes a nearly circular shape at low  $\Delta S_q$ . Thus,  $\Delta S_q$  determines the shape of a droplet on an anisotropic rough surface.

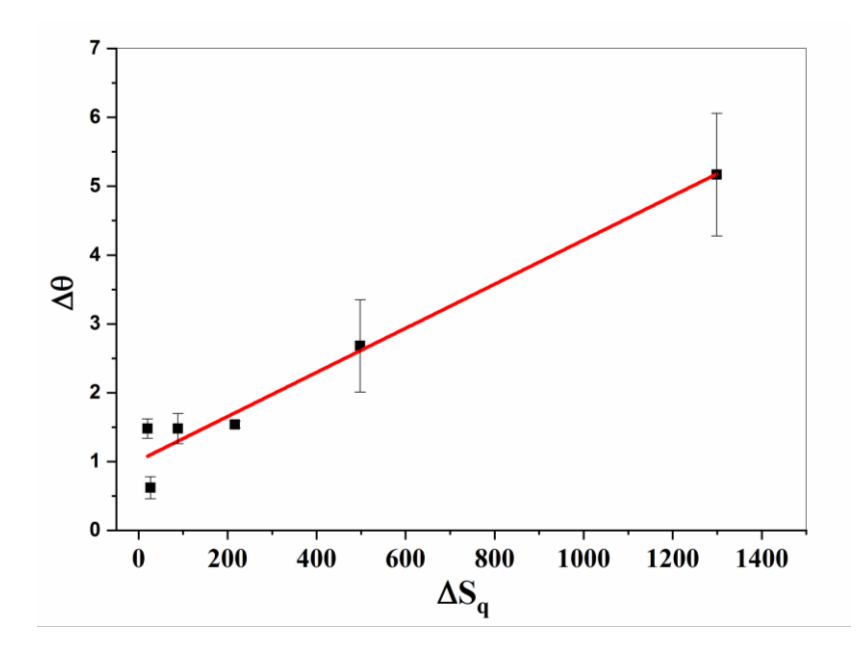


Fig. 6: Change in CA of the ellipsoidal water droplets on laser-irradiated Cu surfaces as a function of change in average 1D RMS SHD along with two perpendicular directions. Error bar represented in the plot is obtained from the measurement statistics.

In **Table 1**, the last column gives the average RMS roughness of each substrate over the entire surface. One can notice that the CAs have no proper correlation with the roughness of the surface, which is predicted by TCL theory. The CAs in such a state are well explained using triple contact line theory proposed by Liu [39] based on the spherical droplet assumption.

$$\frac{3V_e}{\pi r^3} = \frac{(1-\cos\theta)(2+\cos\theta)}{\sin\theta(1+\cos\theta)} \tag{1}$$

Where  $V_e = V - \overline{V}$ , is the effective volume of the droplet on the patterned surfaces, V is the total volume of the droplets  $\overline{V}$  fraction of the droplet that penetrates the micro-structures of the patterned surface, and r is the contact radius of a sphere the liquid-solid interface as shown schematically in **Fig. 7A**. As there is no liquid penetration into the microstructures in Cassie state, therefore effective volume of the droplet is V itself. We have investigated the TCL theory with our experimentally observed anisotropic CAs. The black dashed curve represents the theoretical TCL plot for the spherical droplet assumption [39]. Our experimentally measured CAs are not obeying spherical droplet

TCL theory predictions. The reasons are a) the patterned surfaces are no longer isotropic; b) droplets are ellipsoidal rather than spherical. Hence this model based on a triple contact line may not apply to anisotropic water droplets, and further investigation is required. We derived an equation that can relate the ellipsoidal cap volume of the droplets to the anisotropic CAs (which is the actual volume of the droplets resting on the patterned surfaces). The direction of semi-axes and orientation of the CAs are shown in **Fig. 7(B-D)**. We derived the relationships between anisotropic CAs in two orthogonal directions and their semi-axes (a, b, & c) along with the elliptical liquid-solid interface as shown in **Fig. 7(C-D)**. Semi axes 'a' are along the groves, 'b' is perpendicular to the groove and 'c' is along Z-axis, as shown in **Fig. 7(B-D)**.

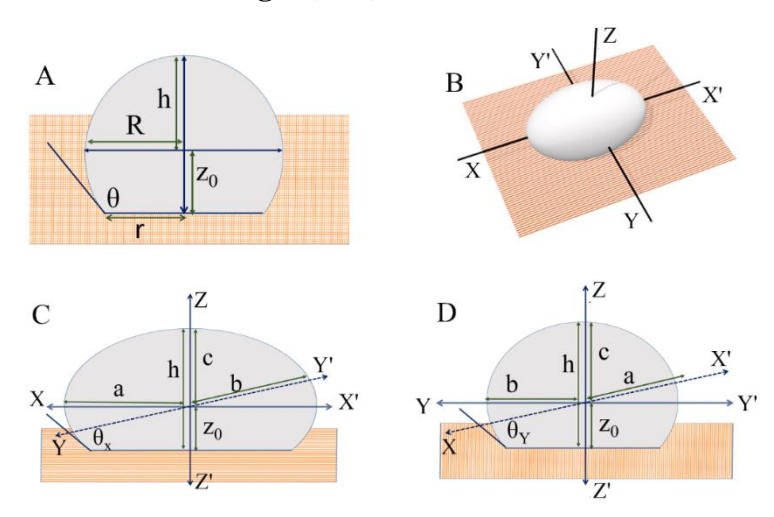


Fig. 7: Schematic of spherical water droplets on copper irradiated surfaces. A: Schematic spherical water droplet resting on the isotropic surface. B: The axis orientation shows which X and Y axes are along the grooves and perpendicular to the grooves, respectively. C: Ellipsoidal water droplet resting on the anisotropic surfaces.  $\theta_X$  and major axis are measured along the grooves. D:  $\theta_Y$  and minor axis are measured perpendicular to the grooves.

The following function expresses an ellipsoid,

$$\frac{x^2}{a^2} + \frac{y^2}{b^2} + \frac{z^2}{c^2} = 1 \tag{1}$$

Where a, b, and c are the semi-axes with  $a \neq b \neq c$ , a > 0, b > 0, and c > 0.

The volume of the ellipsoidal cap of height h is given by

$$V_C = \frac{\pi abh^2(3c-h)}{3c^2} \tag{2}$$

We derived the following relations between the semi-axes and anisotropic CAs, as shown in **Fig. 7(C-D)**.

$$a = \frac{c\sqrt{c^2 - z_0^2 \cot \theta_x}}{z_0}$$
 3(a)

$$b = \frac{c\sqrt{c^2 - z_0^2 \cot \theta_y}}{z_0}$$
 3(b)

$$h = c + z_0 3(c)$$

Where  $\theta_x$  and  $\theta_y$  are the CAs along X-axis and Y-axis, respectively,  $Z_0$  is the perpendicular length from the center of the droplet to the midpoint of the liquid contact of the surface. We arrived at the following equation for the droplet volume in terms of anisotropic CAs and droplet parameters.

$$V_C = \frac{\pi (2ch^3 - h^4)(3c - h)\cot\theta_x \cot\theta_y}{3(h - c)^2}$$
 (4)

We define a dimensionless volume function  $f(\theta_x, \theta_y)$  by arranging the variables in equation 5.

$$f(\theta_x, \theta_y) = \frac{3V_C(h-c)^2}{\pi(2ch^3 - h^4)(3c - h)} = \cot \theta_x \cot \theta_y \qquad (5)$$

This function is plotted and shown in **Fig. 8** by a solid dark cyan curve along with the experimentally measured data points.

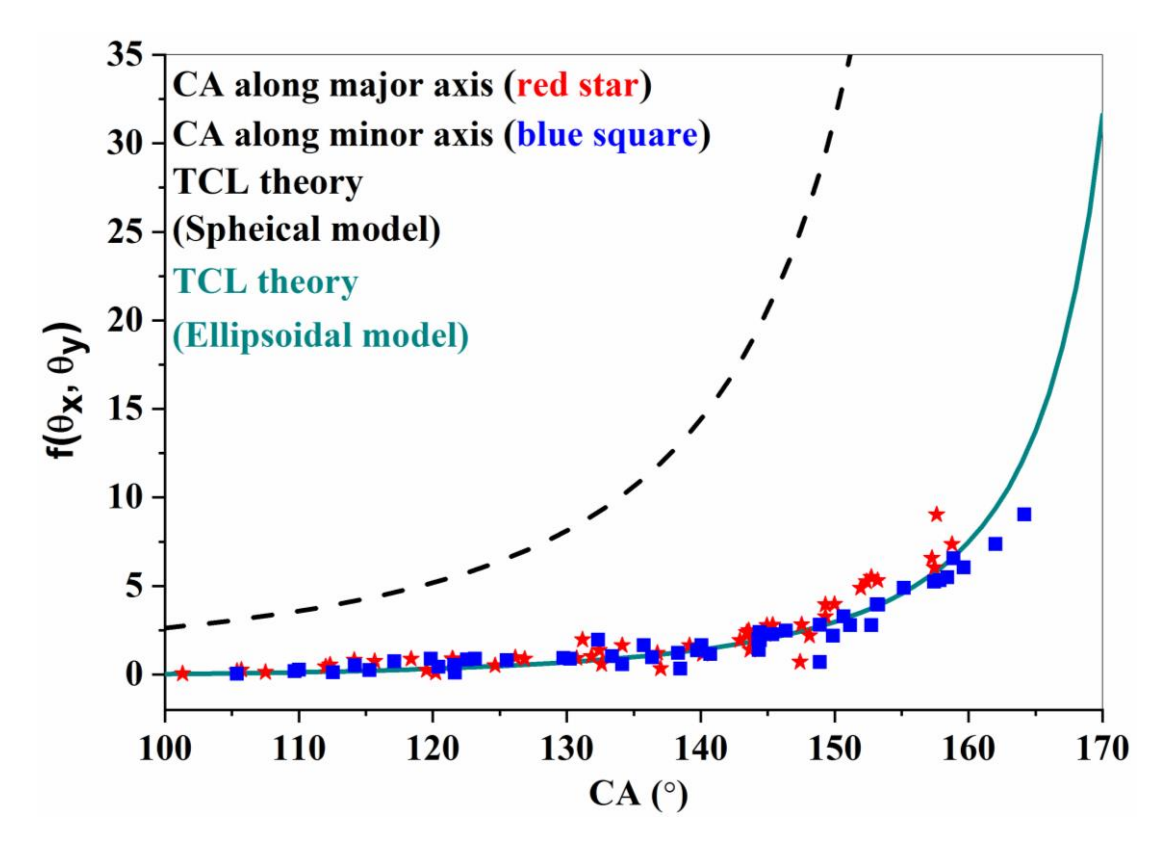


Fig. 8: This graph shows the variation of  $f(\theta_x, \theta_y) = \cot \theta_x \cot \theta_y$  as a function of two anisotropic CAs, the Black dashed, and dark cyan curves are the variations of CAs (theoretically) of the TCL model based on spherical and ellipsoidal water droplets, respectively. The red stars and blue squares show the experimental data points corresponding to the CAs along the grooves and perpendicular to the grooves, respectively. A total of 48 measurements was made on all the substrates from (i) to (vi).

One can observe, our experimental data points match very well with the theoretical model represented by the solid line with a very slight deviation. For an elliptical droplet, the plot of **Fig. 8** is not a true representation; it is just a special case where  $\theta_x$  and  $\theta_y$  have equal values (a slice of **Fig. 9(ii)**, however it is not equal to the spherical case as ("a = b  $\neq$  c"). It has been presented only to compare with the previous spherical model. The fitting appears very close because of anisotropy in CAs is within 6°. The effective volume function should be represented as a 3D picture with  $f(\theta_x, \theta_y)$ ,  $\theta_x$ , &  $\theta_y$  as three axes. The dimensionless volume function is plotted as contour plot and 3D surface plot along with our experimental data points as shown in **Fig. 9(i)** and **Fig. 9(ii)**, respectively. The average relative error of the experimental value of  $f(\theta_x, \theta_y)$  from the theoretical is 4.74 %, which

is within the experimental errors. These experiments and the fittings strongly support the TCL theory, where the contact line pinning dictates the contact angle of the water droplet.

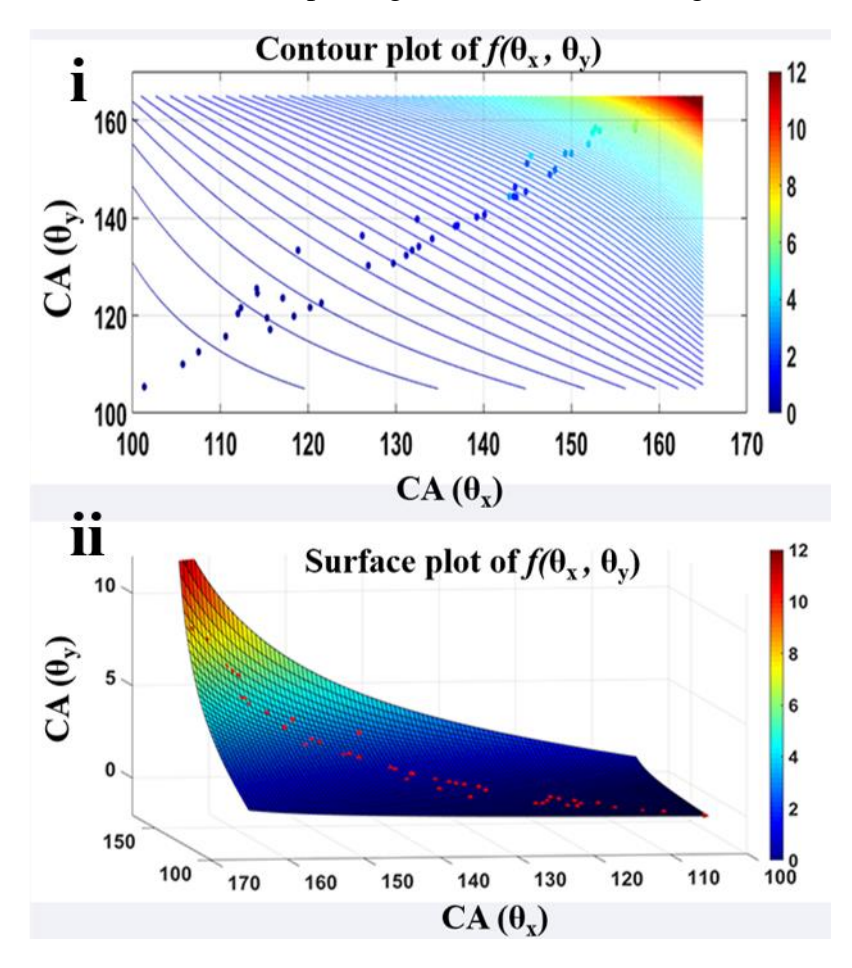


Fig. 9: TCL model for Ellipsoidal droplet with experimental data points for CA along the minor axis (in degree). Plot (i) and (ii) show the contour and surface plot, respectively.

# 6.3.2. Validity of TCL theory from hydrophilic to superhydrophobic surfaces

In the earlier section, the TCL theory is experimentally verified only for superhydrophobic surfaces (Cu substrates only), and contact angles were more than  $100^{\circ}$ . This section will extend the work over the large range contact angle from  $37^{\circ}$  to  $172^{\circ}$ . The qualitative approach of spreading dynamics of the droplets on the anisotropic surfaces is discussed. The evolution of contact angle on the surfaces is provided. Total 16 substrates of Cu and SS were fabricated with the fixed fluence of 1.3 J/cm2, with line spacing of 15, 30, 45, and 60  $\mu$ m. Each spacing set is with both single and double laser

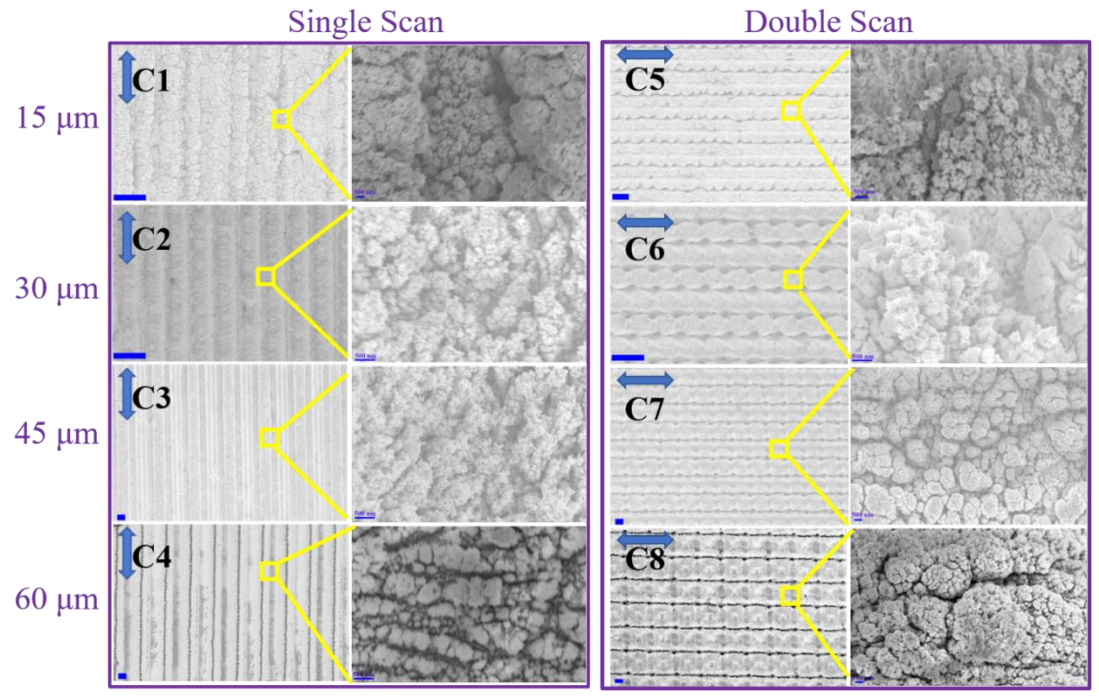
scan methods, as presented in **Table 2**. Anisotropic CAs are shown in **Table 2** for Cu and SS substrates. Using a commercial Eppendorf micropipette, we used a fixed droplet volume of 7  $\mu$ L for each CA measurement for Cu and SS. Our laser fabricated surfaces yield a very high CA as much as ~172° on Cu for C5 substrate, as shown in **Table 2**. All these surfaces evolve with time due to oxidation of the surface under ambient laboratory conditions. The CAs presented in **Table 2** are the final values after 125 days of evolution. After this time, the surface behaves very stably in terms of wetting properties.

Table 2. Laser parameters and corresponding CAs on the Cu and SS substrates.

Line	Type of Scan	Cu substrates				SS substrates				
spacing (µm)		No.	$\theta_{x}$	$\theta_{y}$	Δθ	No.	$\theta_{x}$	$\theta_{\mathrm{y}}$	Δθ	
15	Single	C1	167.7±1.2°	170.5±2.7°	2.8±1.5°	S1	164.1±0.8°	165.1±0.6°	1±0.2°	
30	Single	C2	166.4±2.5°	168.6±1.8°	2.4±0.7°	S2	134.8±2.1°	141.6±1.5°	6.8±1.3°	
45	Single	СЗ	165.1±2.4°	166.5±2.3°	1.4±0.1°	S3	163.2±0.1°	165.9±0.1°	2.7±0.0°	
60	Single	C4	162.8±5.4°	166.1±3.5°	3.3±1.9°	S4	162.7±1.1°	164.6±1.4°	1.9±0.2°	
15	Double	C5	169.3±1.4°	172.4±2.1°	3.1±0.7°	S5	164.8±0.9°	167.6±0.9°	2.8±0.0°	
30	Double	C6	167.6±2.7°	169.2±2.7°	1.6±0.0°	S6	167.5±2.2°	168.4±2.1°	0.9±0.1°	
45	Double	C7	167.1±1.2°	168.1±1.5°	1.0±0.3°	S7	168.3±1.9°	169.6±2.4°	1.3±0.5°	
60	Double	C8	169.3±0.6°	171.0±0.7°	1.7±0.1°	<b>S</b> 8	168.6±0.8°	171.1±1.0°	3.5±0.2°	

The FESEM images are shown in **Fig. 10** and **Fig. 11** for Cu and SS substrates, respectively. Each substrate's FESEM image is presented in two different magnifications to understand their macroscopic surface morphologies (scale bar is 20 µm) and microscopic nanostructures (scale bar 500 nm). In **Fig. 10** and **Fig. 11**, the first and second columns show the single and double scan images, respectively, with corresponding line spacing. The first scan of direct laser writing increases the surface roughness and optical absorption compared to the un-patterned surface [47,55]. It is easier to ablate a rough surface than a smooth surface. Therefore, the second scan (orthogonal to the first scan)

generates higher and smoother groove depth due to increased efficiency in material ablation. The combination forms a very clear macroscopic square grid structure, with the second scan groove being deeper over and on top of the first scan groove. The macroscopic surface morphologies of double scan substrates are different from single scan substrates, which can be observed from the lower magnified FESEM images. The cauliflower-like hierarchical micro-nano structures are observed only with line spacing 45 and 60  $\mu$ m for double scanned substrates but not prominent in single scan substrates. The hierarchical structures of grooves and cauliflower-like secondary nano shapes offer a better barrier against the liquid flow, which is evident from observed higher CAs.



**Fig. 10**. Optical micrographs of the laser-irradiated Cu surfaces. The single and double scanned images are represented in two columns for the line spacing of 15, 30, 45, and 60  $\mu$ m. The magnified images with a scale bar of 500nm are shown next to each substrate's main images (20  $\mu$ m scale bar), and the arrows represent the scanning direction.

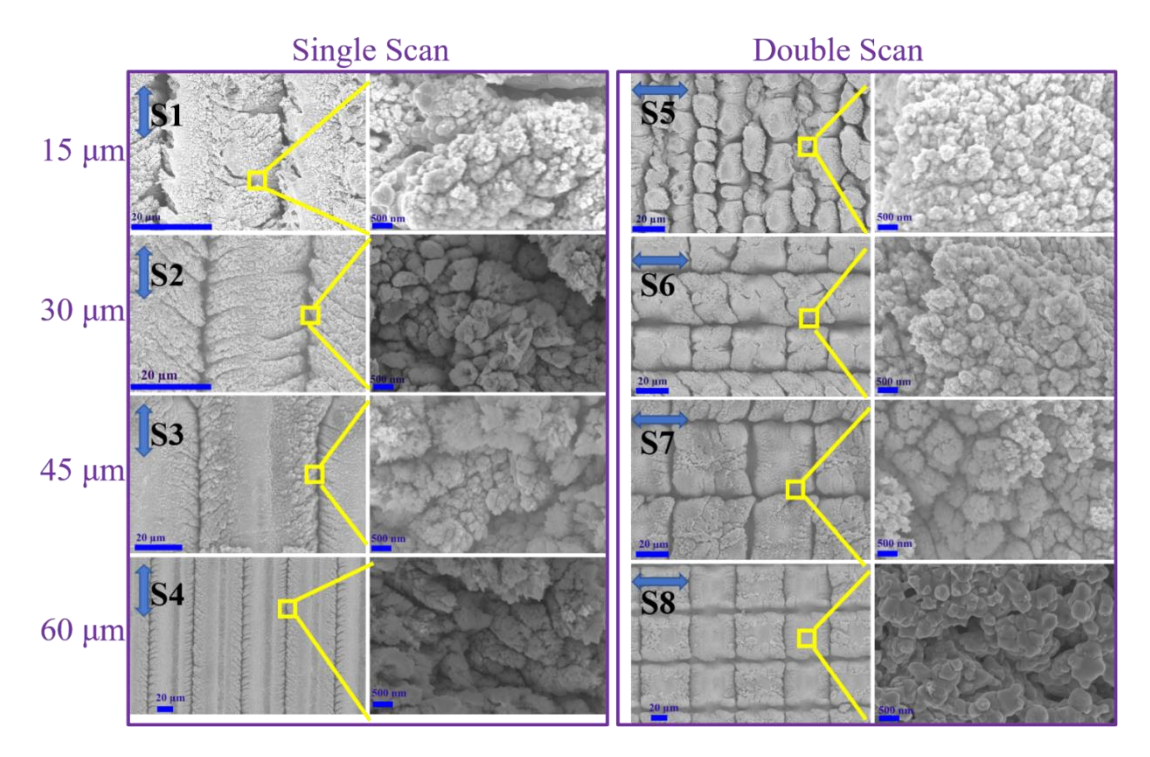


Fig. 11. Optical micrographs of the laser-irradiated SS surfaces. Notations are similar to Fig. 10.

# 6.3.2.1. Spreading dynamics of the droplet immediately after fabrication

The comparative study of the evolution of CAs with time (in the scale of days) on nanostructured Cu and SS surfaces is carried out. Contrasting results were observed between the Cu and SS substrates immediately after the laser writing. We present the qualitative spreading characteristics of water droplets on C1, C5, S1, and S5 substrates. As presented in the earlier reports, the surfaces become hydrophilic immediately after laser writing[53]. Our experiment observed that the laser patterned SS surfaces become hydrophilic immediately after the laser writing, both in single and double scan cases. We investigated the droplets' spreading behavior on these substrates and found the difference in droplets' spreading rate in the two orthogonal directions. The liquid water starts spreading quickly when we place the droplet on S1. The spreading rate is faster along the direction of the grooves and is slower in the perpendicular, which is also consistent with earlier reports[56].

Similarly, the liquid starts spreading immediately after placing the liquid droplet on S5. The spreading rate is the same in two orthogonal directions of the surfaces. But in contrast

to the SS surfaces, the Cu surface behaves differently. The liquid does not spread on the surface of C1; instead forms an ellipsoidal droplet with  $CA_x$  110° and  $CA_y$  113°. In the case of C5, the surface gets wet, and water starts spreading homogeneously after being placed on the sample. But the rate of spreading is much slower than S1 and S5.

The polished SS substrate, which is intrinsically hydrophilic, becomes super hydrophilic immediately after the laser patterning[57]. On the other hand, the unpatterned Cu surface has CAs greater than 90°. The laser patterned surfaces do evolve with time due to the oxidation process. They form the secondary structures on top of the primary structures of laser grooves, as shown in **Fig. 10** and **Fig. 11**. As they evolve, their wetting properties also evolve to form stable superhydrophobic surfaces nearly after 90 days. The evolution of the SS and Cu surface's wetting properties is presented in **Fig. 12**. Typically, this evolution pattern is observed on all surfaces. Cu surface is observed to evolve faster than SS surface. Note: in this process of evolution, the droplets take different shapes from hydrophilic to hydrophobic. These droplet parameters of different wetting properties on the surface are taken as data for the TCL theory validity, which we shall discuss in the following sections.

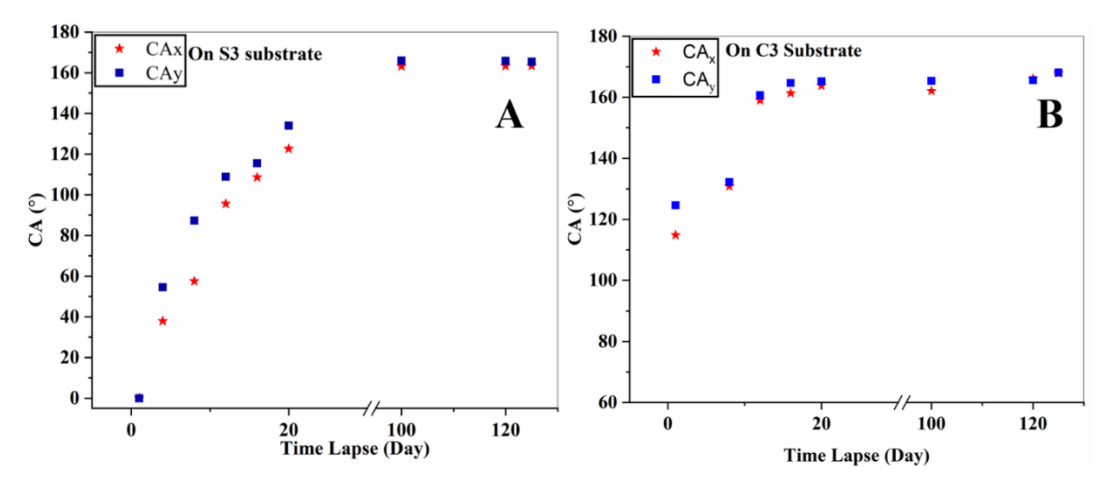


Fig. 12. CA evolution on two different substrates (stainless steel and copper) for 125 days. A: the evolution of CAs on S3. B: the evolution of CAs on C3. The red stars and blue squares represent the CAs along the grooves and perpendicular to the grooves, respectively.

#### 6.3.2.2. Surface evolution from Petal effect to lotus leaf behavior

It is observed, despite high CA (~122.9°) on copper (on the 11<sup>th</sup> day after the fabrication); still, the droplets are not rolling off from the surface even when the substrate is held vertically in the upside direction or even inverted. The adhesive force of the surface to the water droplet is so high that droplets cannot roll-off due to gravity or external disturbances. This behavior is popularly known as the petal effect. We have observed this behavior on substrates C1, C5, S1, and S5 on the 11<sup>th</sup> day after laser fabrication. The S1 and S5 have the CA of 164.9° and154.1°, respectively, but droplets did not roll off even at a 90° tilt angle. Similar behavior was observed in C1 and C5 on the 11<sup>th</sup> day of fabrication, CAs with 122.9° and 168.9° respectively but did not roll off at any tilt angle. The kind of surface chemistry that leads to these strong adhesive forces needs to be further investigated; it is beyond the scope of this paper. This behavior changes within a few days after this, and even with slight tilt angles, they get rolled off, leading to the lotus leaf effect. Note that the petal effect is observed only from the 11<sup>th</sup> day, and slowly within a few days, they lose this property and turn to the lotus leaf behavior.

#### 6.3.2.3. The effect of line spacing and multiple scans on the anisotropic CAs

The CAs can be tuned with line spacing [57], the effect of line spacing between two successive scans is presented. **Fig. 13** presents the holistic results we observed with variation of line spacing. The first and second columns of **Fig. 13** show the copper and the SS substrates, respectively. The upper row shows the change of the CAs with the line spacing, while the bottom row shows the change of anisotropy of the droplets with line spacing. The data is plotted from **Table 2**, whose CAs were obtained after 125 days of evolution and stabilization. The line spacing experiments are performed at 15  $\mu$ m, 30  $\mu$ m, 45  $\mu$ m, and 60  $\mu$ m. Only in the case of 15 $\mu$ m spacing, the laser beam overlaps with the following scan by approximately ~32%; in all other cases, there is no overlap region of laser spots between the successive scans.

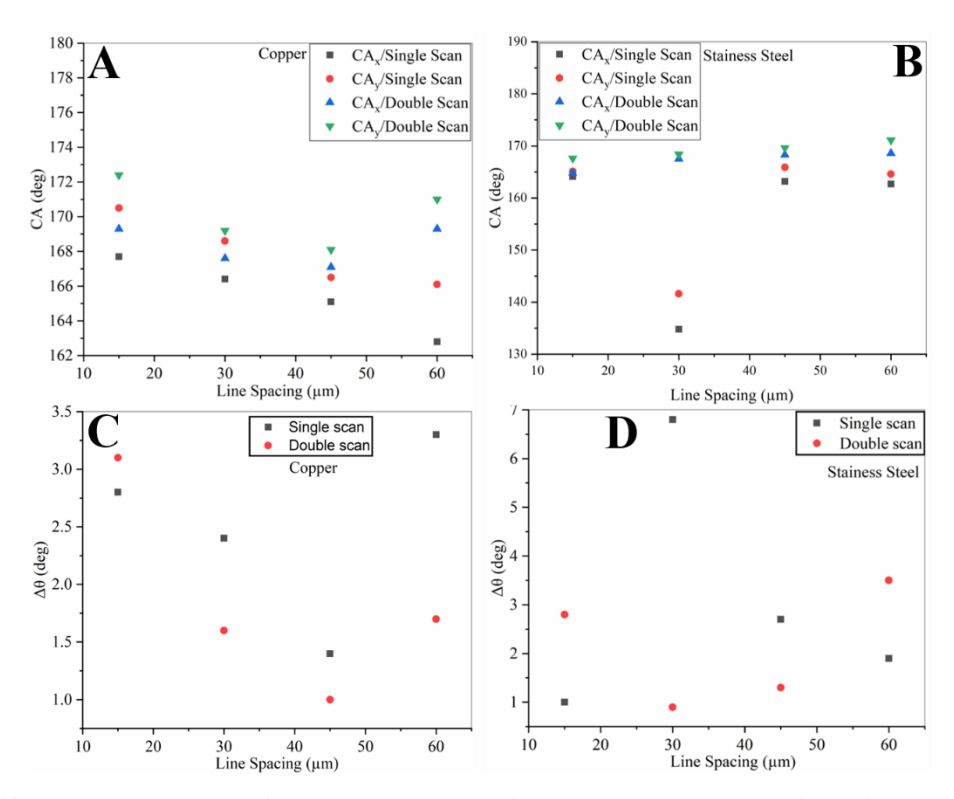


Fig. 13: Variation of CAs and anisotropy in CAs to line spacing on copper and stainless-steel irradiated surfaces for single and double scans. A: CAs on copper substrates, B: CAs on stainless steel substrates, C: anisotropy of CAs on copper, D: anisotropy of CAs on SS.

One can observe in **Fig. 13(A)** and **Fig. 13(B)**, black squares are consistently below the red circles in both Cu and SS substrates. Single scan along x-direction creates groove along the x-axis, the  $\theta_x$  will be lower along the groove direction as it does not have a large barrier against the flow of liquid, compared to orthogonal direction  $\theta_y$  is perpendicular to the groove the barrier will be high. With the increase of spacing for a single scan in Cu surfaces, the CAs consistently decrease due to the rise in the non-irradiated area. However, this scenario for the single scan is similar for the SS surface, except for 30  $\mu$ m spacing (in **Fig. 13(B)**), the scale on the y-axis is different from the adjacent figure). One can get a hint from **Fig. 11** (S2 substrate) that the lower CA is due to the long perpendicular cracks almost reaching the other line cracks. These cracks might reduce the barrier or support the flow of fluid, leading to smaller CAs.

Similarly, for the double scan case (**Fig. 13(A**) and **Fig. 13(B)**), blue triangles are consistently below the green inverted triangles for both Cu and SS substrates. Also, in all the cases, the double scan CAs are always higher than the single scan as they offer a larger barrier for the liquid flow due to their surface morphology. One must remember that the droplet base area is much bigger than the groove spacing approximately by magnitude. For double scan, increasing spacing for Cu substrates results in a decrease of CAs till 45  $\mu$ m spacing and increases for 60  $\mu$ m spacing. But in SS substrate, it is a slight monotonous increase in CAs. This may be due to the Cu and SS surfaces' morphological or surface structural differences. **Fig. 13(C)** and **Fig. 13(D)** give the water droplets' anisotropy formed for Cu and SS surfaces under different writing conditions. In general, for the spacing greater than the laser's spot size (22  $\mu$ m), the anisotropy is more significant in the single scanned substrates due to the inhomogeneous surface created by the single scan. For the spacing less than the focal spot size, for 15  $\mu$ m, the anisotropy is larger in the double scanned substrates. However, one exception is 60  $\mu$ m of SS case, which has shown more anisotropy in the double scan.

# 6.3.2.4. Triple contact line theory and its approach to the hydrophilic surfaces

After the evolution for more than three months, the anisotropic CAs were presented for Cu and SS substrates in **Table 2**, derived from a large data set. Also, during the evolution process, we measured CAs periodically. In each measurement, we got the CAs along the direction of the grooves and CAs orthogonal to the grooves. Apart from the CAs, we also measured the droplet dimensions in orthogonal directions. Note that even when the droplet formation is homogeneously along the surface, the semi-third axis along the height is not equal to the semi-major and minor axis due to the gravity effect on the droplet. **Fig. 14** gives the schematic illustration of the measured ellipsoidal dimensions or parameters. The semi-major axis length along the groove is 'a', and the corresponding CA is ' $\theta_{X}$ ' is measured.

Similarly, the length of the semi-minor axis perpendicular to the groove is 'b,' and the corresponding CA is ' $\theta_y$ '. Also, we measure the height of the droplet 'h' and derive the

value of 'c' from droplet parameters. These parameters are shown in **Fig. 14**; our length measurements are calibrated with a reference of the substrate's length. The ellipsoidal cap volume 'Vc'' is given by equation (1) in terms of the droplet's physical parameters and anisotropic CAs [52]. The dimensionless effective volume function ' $f(\theta_x, \theta_y)$ ' is expressed by equation (2).

$$V_C = \frac{\pi a b h^2 (3c - h)}{3c^2} = \frac{\pi (2ch^3 - h^4)(3c - h)\cot\theta_x \cot\theta_y}{3(h - c)^2}$$
(1)  
$$f(\theta_x, \theta_y) = \frac{a b (h - c)^2}{c^2 (2ch - h^2)} = \cot\theta_x \cot\theta_y$$
(2)

The primary purpose of this dimensionless volume function,  $f(\theta_x, \theta_y) = \cot\theta_x \cot\theta_y$ , is to relate the ellipsoidal droplet's parameters with the CAs in orthogonal directions for CAs greater than 90°. These droplet parameters must be unique for given CAs determined by the droplet's pinning line boundary at the air, solid, and liquid interface. This function consists of the parameters a, b, c, and h (where h is the height of the droplet). These parameters are experimentally measurable for a given sessile droplet. We calculated the functional values and compared them with  $f(\theta_x, \theta_y)$ . We observed an excellent fit between the experimentally derived values of  $f(\theta_x, \theta_y)$  using droplet's physical dimensions and the theoretically estimate value of  $f(\theta_x, \theta_y) = \cot\theta_x \cot\theta_y$  [52]. This is experimental evidence supporting the TCL theory.

In contrast to the widely accepted Wenzel and Cassie models, TCL theory predicts that the CAs depend only on the droplet's pinning boundary and are irrelevant to the surface roughness of the interfacial area droplet. However, surface roughness plays a vital role in forming sessile droplets on the patterned substrates as it offers a barrier against the flow of the liquid. We create anisotropic surfaces by laser writing techniques, the surface offers two different barrier conditions against the liquid flow in the orthogonal directions to form ellipsoidal droplets.

For water droplets having CAs less than 90°, all the ellipse parameters 'a', 'b,' and 'c' cannot be obtained directly. Experimentally, the base of a droplet ' $2x_l$ ' along the x-axis,

 $2y_I$  along the y-axis, and the height of a droplet h along the z-axis are measurable parameters. Taking the XZ plane of the ellipse, one can arrive at the following equations.

$$c = \frac{x_1 h \operatorname{Tan} \theta_x - h^2}{x_1 \operatorname{Tan} \theta_x - 2 h} \tag{3}$$

$$a^2 = \frac{c^2 x_1 \cot \theta_x}{c - h} \tag{4}$$

Similarly, taking the YZ plane of the ellipse, one can arrive at the minor axis of the ellipse

$$b^2 = \frac{c^2 y_1 \cot \theta_y}{c - h} \tag{5}$$

For hydrophilic cases, the ellipse parameters 'a', 'b', and 'c' need to be estimated from the measurements of  $x_I$ ,  $y_I$ , h,  $\theta_x$ , and  $\theta_y$ . The ellipsoidal cap volume 'Vc' and dimensionless effective volume function ' $f(\theta_x, \theta_y)$ ' is expressed in equations (1) and (2) are valid for the hydrophilic case as well. Using the above equations, we tested this theory over a larger spectrum of contact angles (hydrophilic to superhydrophobic CAs). The theoretical values of the function ' $f(\theta_x, \theta_y)$ ' is treated as ' $Cot \theta_x$  Cot  $\theta_y$ '. That is for any ellipsoidal droplet characterized by its contact angles of  $\theta_x$  &  $\theta_y$  in orthogonal directions, will have a unique theoretical functional value of ' $f(\theta_x, \theta_y)$ '. If  $\theta_y$  &  $\theta_y$  are taken as continuous variables, the theoretical functional values are represented as a solid line in figure 7A, or it can take the shape of a surface in a three-dimensional plot, as shown in figure 7B. The experimentally measured values of this function ' $f(\theta_x, \theta_y)$ ' are obtained from the droplet physical dimensions as given in equation (2).

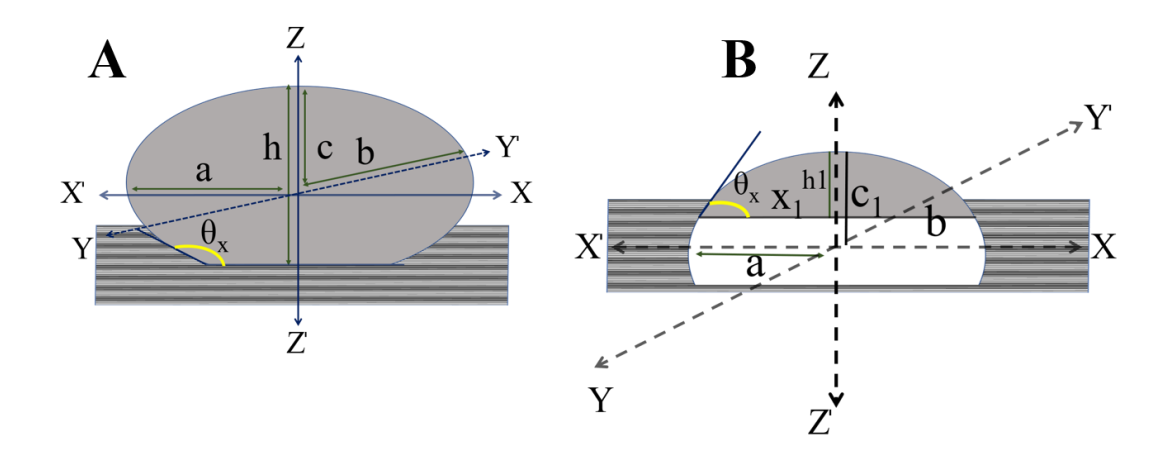


**Fig. 14:** Schematic of anisotropic (**A**) superhydrophobic and (**B**) hydrophilic water droplets on laser-irradiated substrates.  $\theta_X$  & major axis "2a", is measured along the grooves, and  $\theta_Y$  & minor axis "2b", are perpendicular to the grooves.

# 6.3.2.5. TCL analysis for droplets on the patterned Cu and SS surfaces

The CAs given in **Table 2** is the statistical average of several droplets formed on each substrate, both Cu and SS. Each droplet formed is taken as a data point for obtaining a, b, c, h, x and  $\theta_y$  parameters of an ellipsoidal droplet. A 2D plot of dimensionless effective volume function  $f(\theta_x, \theta_y)$  is shown in **Fig. 15(A)**, where dimensionless function  $f(\theta_x, \theta_y)$ is plotted on the y-axis, and the  $CA_x$  and  $CA_y$  are in the x-axis, for all the droplets formed on patterned Cu and SS substrates. The data points in this graph include the points obtained during the evolution of CAs on both surfaces. The red-colored stars and bluecolored squares represent the  $CA_x$  and  $CA_y$ , respectively. For a given set of the  $CA_x$  $\theta_{\nu}$ ), there is a unique value for the function  $f(\theta_{x}, \theta_{\nu})$ . Hence, a given droplet along the grooves and across the grooves will have the same y-axis value on these plots. In other words, each droplet has a unique value in the y-axis with the corresponding pair of  $\theta_x$  &  $\theta_{y}$  values. The solid line represents the theoretical value of TCL theory based on the ellipsoidal droplet. The actual functional value always lies between the star and square points along the y-axis. There is a unique value of  $f(\theta_x, \theta_y)$  for a given  $\theta_x$ ,  $\theta_y$  value, hence this 2D figure is a projection of the actual 3D plot in the diagonal plane. The 3D plot of these values is shown in **Fig. 15(B)**. In this, each water droplet condenses to a single circular point in this graph having a unique function value  $f(\theta_x, \theta_y)$  for a fixed  $\theta_x \& \theta_y$ 

value. All the points correlate to the functional value, color grid surface, with an R<sup>2</sup>-regression coefficient of 0.81.

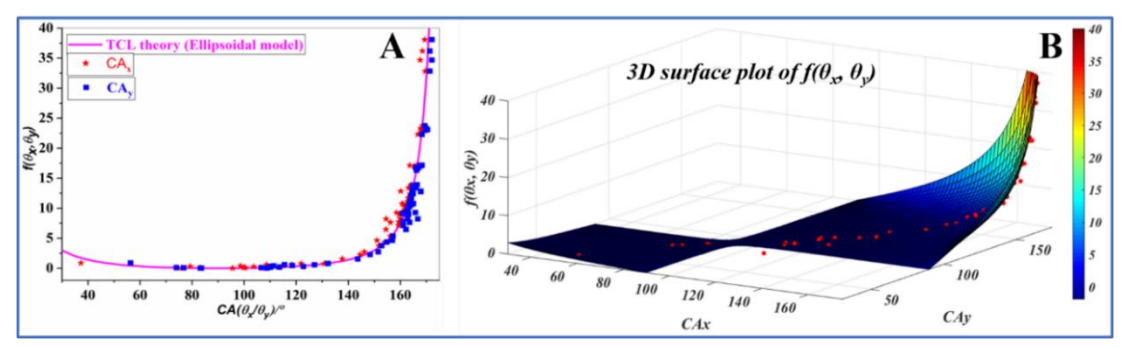


**Fig. 15**: Combined data from Cu and SS substrates are presented in these figures. (**A**) Two-dimensional plot of the  $f(\theta_x, \theta_y)$  vs. Cas. The red-colored stars and blue-colored squares represent the CAs along the grooves and perpendicular to the grooves. (**B**) Three-dimensional plot of the  $f(\theta_x, \theta_y)$  vs.  $\theta_x \& \theta_y$ . The red-colored symbols represent the experimental value of the  $f(\theta_x, \theta_y)$ .

#### **6.4. Conclusions**

We have engineered Cu and SS wetting properties using femtosecond laser direct writing. By varying the laser writing line spacing, we optimized the best conditions for the Cu surface to behave as superhydrophobic with CA as much as 172°. Droplets formed ellipsoidal shapes due to the anisotropic surface morphology of the surfaces. The evolution of the CAs due to the oxidation process on both these surfaces is presented. We experimentally measured the dimensions of these ellipsoidal droplets from hydrophilic to superhydrophobic cases. Expressions for the ellipsoidal droplet volume estimations were presented for the entire range of CAs. A dimensionless volume function,  $f(\theta_x, \theta_y)$ , uniquely depends on the droplet's dimensions is presented. The experimentally measured data and theoretically predicted values of this function show an excellent correlation over a broad range of CAs. This is a direct experimental validation of the Triple contact line (TCL) theory for the most generalized form of ellipsoidal droplets. We believe our work will help develop new kinds of functional surfaces with intrinsic anisotropy and the droplet's non-contact volume calibration for many quantitative measurements.

#### References

- [1] Feng L, Zhang Y, Xi J, Zhu Y, Wang N, Xia F and Jiang L 2008 Petal effect: A superhydrophobic state with high adhesive force *Langmuir* **24** 4114–9.
- [2] He A, Liu W, Xue W, Yang H and Cao Y 2018 Nanosecond laser ablated copper superhydrophobic surface with tunable ultrahigh adhesion and its renewability with low temperature annealing *Appl. Surf. Sci.* **434** 120–5.
- [3] Myint M T Z, Hornyak G L and Dutta J 2014 One pot synthesis of opposing "rose petal" and "lotus leaf" superhydrophobic materials with zinc oxide nanorods *J. Colloid Interface Sci.* **415** 32–8.
- [4] Long J, Fan P, Gong D, Jiang D, Zhang H, Li L and Zhong M 2015 Superhydrophobic surfaces fabricated by femtosecond laser with tunable water adhesion: From lotus leaf to rose petal *ACS Appl. Mater. Interfaces* **7** 9858–65.
- [5] Nine M J, Tung T T, Alotaibi F, Tran D N H and Losic D 2017 Facile Adhesion-Tuning of Superhydrophobic Surfaces between "Lotus" and "Petal" Effect and Their Influence on Icing and Deicing Properties *ACS Appl. Mater. Interfaces* **9** 8393–402.
- [6] Gocalinska A, Gradkowski K, Dimastrodonato V, Mereni L O, Juska G, Huyet G and Pelucchi E 2011 Wettability and "petal effect" of GaAs native oxides *J. Appl. Phys.* **110.**
- [7] Fürstner R, Barthlott W, Neinhuis C and Walzel P 2005 Wetting and self-cleaning properties of artificial superhydrophobic surfaces *Langmuir* **21** 956–61.
- [8] Chu K H, Xiao R and Wang E N 2010 Uni-directional liquid spreading on asymmetric nanostructured surfaces *Nat. Mater.* **9** 413–7.
- [9] Liang Y, Shu L, Natsu W and He F 2015 Anisotropic wetting characteristics versus roughness on machined surfaces of hydrophilic and hydrophobic materials *Appl. Surf. Sci.* **331** 41–9.
- [10] Kusumaatmaja H, Vrancken R J, Bastiaansen C W M and Yeomans J M 2008 Anisotropic drop morphologies on corrugated surfaces *Langmuir* **24** 7299–308.
- [11] David R and Neumann A W 2012 Shapes of drops in the Cassie state on grooved

- surfaces Colloids Surfaces A Physicochem. Eng. Asp. 399 41–5.
- [12] Zhao Y, Lu Q, Li M and Li X 2007 Anisotropic wetting characteristics on submicrometer-scale periodic grooved surface *Langmuir* **23** 6212–7.
- [13] Morita M, Koga T, Otsuka H and Takahara A 2005 Macroscopic-wetting anisotropy on the line-patterned surface of fluoroalkylsilane monolayers *Langmuir* **21** 911–8.
- [14] Xia D and Brueck S R J 2008 Strongly Anisotropic Wetting on Surfaces 2008 *Nano Lett.* **8** 2819–24.
- [15] Chung J Y, Youngblood J P and Stafford C M 2007 Anisotropic wetting on tunable micro-wrinkled surfaces *Soft Matter* **3** 1163–9.
- [16] Xia D, Johnson L M and Lõpez G P 2012 Anisotropic wetting surfaces with onedimesional and directional structures: Fabrication approaches, wetting properties and potential applications *Adv. Mater.* **24** 1287–302.
- [17] Zhang Y L, Xia H, Kim E and Sun H B 2012 Recent developments in superhydrophobic surfaces with unique structural and functional properties *Soft Matter* 8 11217–31.
- [18] Wang S, Yu N, Wang T, Ge P, Ye S, Xue P, Liu W, Shen H, Zhang J and Yang B 2016 Morphology-Patterned Anisotropic Wetting Surface for Fluid Control and Gas-Liquid Separation in Microfluidics *ACS Appl. Mater. Interfaces* **8** 13094–103.
- [19] Song M, Liu Z, Ma Y, Dong Z, Wang Y and Jiang L 2017 Reducing the contact time using macro anisotropic superhydrophobic surfaces-effect of parallel wire spacing on the drop impact *NPG Asia Mater.* **9** e415-9.
- [20] Vasileiou T, Schutzius T M and Poulikakos D 2017 Imparting Icephobicity with Substrate Flexibility *Langmuir* **33** 6708–18.
- [21] Kwon D, Wooh S, Yoon H and Char K 2018 Mechanoresponsive Tuning of Anisotropic Wetting on Hierarchically Structured Patterns *Langmuir* **34** 4732–8.
- [22] Faustini M, Cattoni A, Peron J, Boissière C, Ebrard P, Malchère A, Steyer P and Grosso D 2018 Dynamic Shaping of Femtoliter Dew Droplets *ACS Nano* **12** 3243–52.
- [23] Zhang X, Shi F, Niu J, Jiang Y and Wang Z 2008 Superhydrophobic surfaces:

- From structural control to functional application *J. Mater. Chem.* **18** 621–33.
- [24] Chen F, Zhang D, Yang Q, Yong J, Du G, Si J, Yun F and Hou X 2013 Bioinspired wetting surface via laser microfabrication *ACS Appl. Mater. Interfaces* **5** 6777–92.
- [25] Chen F, Zhang D, Yang Q, Wang X, Dai B, Li X, Hao X, Ding Y, Si J and Hou X 2011 Anisotropic wetting on microstrips surface fabricated by femtosecond laser *Langmuir* 27 359–65.
- [26] Dar M H, Kuladeep R, Saikiran V and Rao N D 2016 Femtosecond laser nanostructuring of titanium metal towards fabrication of low-reflective surfaces over broad wavelength range *Appl. Surf. Sci.* **371** 479–87.
- [27] Zhang D, Chen F, Fang G, Yang Q, Xie D, Qiao G, Li W, Si J and Hou X 2010 Wetting characteristics on hierarchical structures patterned by a femtosecond laser *J. Micromechanics Microengineering* **20.**
- [28] Kietzig A M, Hatzikiriakos S G and Englezos P 2009 Patterned superhydrophobic metallic surfaces *Langmuir* **25** 4821–7.
- [29] Moradi S, Kamal S, Englezos P and Hatzikiriakos S G 2013 Femtosecond laser irradiation of metallic surfaces: Effects of laser parameters on superhydrophobicity *Nanotechnology* **24.**
- [30] Martínez-Calderon M, Rodríguez A, Dias-Ponte A, Morant-Miñana M C, Gómez-Aranzadi M and Olaizola S M 2016 Femtosecond laser fabrication of highly hydrophobic stainless steel surface with hierarchical structures fabricated by combining ordered microstructures and LIPSS *Appl. Surf. Sci.* **374** 81–9.
- [31] Bizi-Bandoki P, Benayoun S, Valette S, Beaugiraud B and Audouard E 2011 Modifications of roughness and wettability properties of metals induced by femtosecond laser treatment *Appl. Surf. Sci.* **257** 5213–8.
- [32] Raimbault O, Benayoun S, Anselme K, Mauclair C, Bourgade T, Kietzig A M, Girard-Lauriault P L, Valette S and Donnet C 2016 The effects of femtosecond laser-textured Ti-6Al-4V on wettability and cell response *Mater. Sci. Eng. C* 69 311–20.
- [33] Wenzel R N 1936 Resistance of solid surfaces to wetting by water *Ind. Eng. Chem.* **28** 988–94.

- [34] Cassie A B D 1948 Contact angles *Discuss. Faraday Soc.* **3** 11–6.
- [35] Zheng Q-S, Yu Y and Zhao Z-H 2005 Effects of Hydraulic Pressure on the Stability and Transition of Wetting Modes of Superhydrophobic Surfaces *Langmuir* **21** 12207–12.
- [36] Erbil H Y 2014 The debate on the dependence of apparent contact angles on drop contact area or three-phase contact line: A review *Surf. Sci. Rep.* **69** 325–65.
- [37] Choi W, Tuteja A, Mabry J M, Cohen R E and McKinley G H 2009 A modified Cassie-Baxter relationship to explain contact angle hysteresis and anisotropy on non-wetting textured surfaces *J. Colloid Interface Sci.* **339** 208–16.
- [38] Gao L and McCarthy T J 2007 How Wenzel and Cassie Were Wrong *Langmuir* **23** 3762–5.
- [39] Liu J, Mei Y and Xia R 2011 A new wetting mechanism based upon triple contact line pinning *Langmuir* 27 196–200.
- [40] Yang J, Rose F R A J, Gadegaard N and Alexander M R 2009 Effect of sessile drop volume on the wetting anisotropy observed on grooved surfaces *Langmuir* **25** 2567–71.
- [41] Tie L, Guo Z and Liu W 2015 Anisotropic wetting properties on various shape of parallel grooved microstructure *J. Colloid Interface Sci.* **453** 142–50.
- [42] Wang Z L, Chen E H and Zhao Y P 2018 The effect of surface anisotropy on contact angles and the characterization of elliptical cap droplets *Sci. China Technol. Sci.* **61** 309–16.
- [43] Ta V D, Dunn A, Wasley T J, Li J, Kay R W, Stringer J, Smith P J, Esenturk E, Connaughton C and Shephard J D 2016 Laser textured superhydrophobic surfaces and their applications for homogeneous spot deposition *Appl. Surf. Sci.* **365** 153–9.
- [44] Boinovich L, Emelyanenko A M and Pashinin A S 2010 Analysis of long-term durability of superhydrophobic properties under continuous contact with water *ACS Appl. Mater. Interfaces* **2** 1754–8.
- [45] Stalder A F, Melchior T, Müller M, Sage D, Blu T and Unser M 2010 Low-bond axisymmetric drop shape analysis for surface tension and contact angle

- measurements of sessile drops *Colloids Surfaces A Physicochem. Eng. Asp.* **364** 72–81.
- [46] Gadelmawla E S, Koura M M, Maksoud T M A, Elewa I M and Soliman H H 2002 Roughness parameters *J. Mater. Process. Technol.* **123** 133–45.
- [47] Murakami D, Jinnai H and Takahara A 2014 Wetting transition from the cassie-baxter state to the wenzel state on textured polymer surfaces *Langmuir* **30** 2061–7.
- [48] Kietzig A-M, Negar Mirvakili M, Kamal S, Englezos P and Hatzikiriakos S G 2011 Laser-Patterned Super-Hydrophobic Pure Metallic Substrates: Cassie to Wenzel Wetting Transitions *J. Adhes. Sci. Technol.* **25** 2789–809.

# Chapter 7

# **Summary and future work**

This thesis aims to engineer material surfaces and study their property using different pulsed laser parameters and processing conditions. Dual-scaled laser-induced periodic surface structures are fabricated using the femtosecond laser irradiation wavelength over a broad range from 400-2200 nm on stainless steel surfaces. We have optimized the laser4 processing parameters for fabricating ladder-like structures where both low spatial frequency LIPSS and High spatial frequency LIPSS simultaneously formed in a clearer and regular fashion. Apart from that, for each wavelength, we have investigated the fluence range for ablation threshold, optimal fluences for favoring the ladder-like features, and fluence at which the LIPSS got destroyed. We have investigated the maximum limit of LIPSS periodicity for the incident wavelength range. This work has opened a new horizon for laser experimentalists and theorists to carry forward to the next level by thoroughly investigating existing theoretical models of LIPSS.

Controlled fabrication of cubic-shaped copper NPs on the surface of copper is shown for the first time in the literature. This can be achieved uniquely via femtosecond laser irradiation using a particular incident wavelength, scanning speed, and incident laser fluence. We showed surface topological structures could be controlled or varied using different wavelengths and irradiation energy. The ideal wavelength for the formation of LIPSS over a broad range of energies is 900 nm. At 960 nm of irradiation wavelength, we could not observe any LIPSS formation for any incident energy. Cubic-shaped nanoparticles with the maximum surface area with many edges can have potential applications, especially in catalytic reactions as electrodes. The formation of the cubic structures is because of the oxygen being trapped; it is favored only at 860 nm central wavelength of femtosecond pulses. This work can be extended to fabricate different sizes and shapes of the nanoparticles, investigate the mechanism behind the origin of a particular type of shape, and apply it in sensing and industrial applications.

We showed that nanosecond pulse laser surface irradiation enables the formation of composite micro-nano hierarchical surface structures, and the surface appears completely black after laser patterning. By laser irradiation, surface nanostructure formed on the surface will increase the area compared to the bare polished SS surface. This study shows that the nanosecond pulse laser irradiation can be used as a scientific tool to create peculiar types of features such as superfine rods and flowers structure with appropriate control of laser fluence. We could achieve the near-complete absorption of the surfaces 99.9 % over a broad wavelength region covering UV, Vis, and near IR. These surfaces are very efficient antireflection over a wide angle of incidence ±75 ° to normal. Also, the optimized surfaces are isotropic for both S and P polarizations, ideal for solar illumination optical systems. We achieved less than 0.14% surface reflectivity in the visible range (250-850 nm) and less than 0.5 % in the infrared region (from 900-1800 nm). These robust pulsed textured metal surfaces show extremely low reflection and find application as super absorbers of light in many optical devices, space applications, lowlight imaging, etc. There's a lot of scope in this work. Using more advanced spectroscopic analysis would be an excellent deal to investigate flower-like features formed by nanosecond laser irradiation. Anisotropic reflectivity can be developed by modifying the surface morphology. Surface morphology can be engineered to absorb electromagnetic waves over a particular wavelength band.

We have engineered Cu and SS wetting properties using femtosecond laser direct writing. By varying the laser writing line spacing, we optimized the best conditions for the Cu surface to behave as superhydrophobic with CA as much as 172°. Droplets formed ellipsoidal shapes due to the anisotropic surface morphology of the surfaces. The evolution of the CAs due to the oxidation process on both these surfaces is presented. We experimentally measured the dimensions of these ellipsoidal droplets from hydrophilic to superhydrophobic cases. Expressions for the ellipsoidal droplet volume estimations were presented for the entire range of CAs. A dimensionless volume function,  $f(\theta_x, \theta_y)$ , uniquely depends on the droplet's dimensions is presented. The experimentally measured data and theoretically predicted values of this function show an excellent correlation over a broad range of CAs. This is a direct experimental validation of the Triple contact line

(TCL) theory for the most generalized form of ellipsoidal droplets. We believe our work will help develop new kinds of functional surfaces with intrinsic anisotropy and the droplet's non-contact volume calibration for many quantitative measurements. The feasibility of this work in the future could be to investigate the miniature lens droplet. It can lead to breakthroughs in optical fields as the high contact angle droplets can substantially bend the beam. This work can also be extended to investigate the droplet's evaporation rate on different surfaces.

# List of Publications

# **Journal publications**

- 1. "Controlled periodicities of ladder-like surface structures via femtosecond laser irradiation of wavelengths from 400 nm to 2200 nm," Md Abu Taher, Nitin Chaudhary, Thirunaukkarasu K,Vinod K Rajput, Sri Ram Gopal Naraharisetty Surfaces and Interfaces, 28 (2022) 101622.
- **2.** "The validity of Triple Contact Line theory from hydrophilic to superhydrophobic surfaces," Md Abu Taher, Vinod Kumar Rajput, Navanith Krishnan P K and Sri Ram Gopal Naraharisetty. *J. Phys. D: Appl. Phys*, 55(2022) 055305.
- 3. "Broadband absorption of nanostructured stainless-steel surface fabricated by nanosecond laser irradiation," Md Abu Taher, Sajin Ponnan, Hitheswar Prasad, Desai Narayana Rao, Sri Ram G Naraharisetty, Nanotechnology, 31(2020) 175301.
- 4. "Ellipsoidal droplet formation on anisotropic superhydrophobic copper surface," Md Abu Taher, Hitheswar Prasad, PK Navanith Krishnan, Narayana Rao Desai, and Sri Ram G Naraharisetty, **Surface Topography: Metrology and Properties**, 7(2019) 035001.
- 5. "A third-order nonlinear optical single crystal of 3,4-dimethoxy-substituted chalcone derivative with high laser damage threshold value: a potential material for optical power limiting," Vinay Parol, AN Prabhu, Md Abu Taher, Sri Ram G Naraharisetty, NK Lokanath, and V Upadhyaya, **Journal of Materials Science:** Materials in Electronics, 31(2020) 9133-9150.
- 6. "A long-chain based bromo and methyl-substituted chalcone derivatives; experimental and theoretical approach on nonlinear optical single crystals," Vinay Parol, V Upadhyaya, AN Prabhu, NK Lokanath, Md Abu Taher, and Sri Ram G Naraharisetty, Materials **Research Express**, 7(2020) 055101.
- 7. "Mechanically and thermally stable thin sheets of broadband antireflective surfaces fabricated by femtosecond laser," Thirunaukkarasu K, Md Abu Taher, Nitin Chaudhary, Vinod K Rajput, Jai Prakash Gautam, Sri Ram Gopal Naraharisetty, **Optics and Laser Technology** (Manuscript ID: JOLT-D-21-02479-R1, accepted).
- 8. "Wavelength dependent cubic nanoparticles formation on copper surfaces by femtosecond laser irradiation", Md Abu Taher, D Narayana Rao, and Sri Ram G Naraharisetty, **Asian Journal of Physics**. (Under review).

- 9. "Compact optical scheme for generation of ultrafast mid-IR laser pulses," Vinod K Rakput, Prasenjit Jana, Sajin Ponnan, Md Abu Taher, and Sri Ram Gopal Naraharisetty, **Pramana**. (Under review).
- 10. "Material dependent upper limit of spatial periodicity of laser induced periodic surface structures", Md Abu Taher, Sri Ram G Naraharisetty. (Manuscript under preparation).
- 11. "Interferometric based ultrafast laser pattering to fabricate ultra-black surfaces on the thin sheets of stainless steel," Thirunaukkarasu K, Nitin Chaudhary, Md Abu Taher, Vinod K Rajput, Sri Ram Gopal Naraharisetty (Manuscript under preparation)

# **Conference proceedings**

- 1. "Super Black Stainless Steel Surfaces Fabricated by Nanosecond Laser Irradiation", Md Abu Taher, Sri Ram G Naraharisetty, and D Narayana Rao, Conference on Lasers and Electro-Optics (CLEO), **IEEE Xplore** (2020).
- "Laser-induced periodic surface structures on stainless steel surfaces with effects of irradiated wavelengths", Md Abu Taher, D Narayana Rao, and Sri Ram G Naraharisetty, 2021 Advanced Solid-State Lasers 2021.

# **Oral Presentations**

- 1. "Simultaneous dual-scale subwavelength gratings formation over a broad wavelength range," Md Abu Taher, D Narayana Rao, Sri Ram G Naraharisetty, Frontiers in Optics and Laser Science, 2021 (Online), Washington, DC, United States.
- 2. "Laser-induced periodic surface structures on stainless steel surfaces with effects of irradiated wavelengths", Md Abu Taher, D Narayana Rao, Sri Ram G Naraharisetty, OSA Laser Congress, 2021 (Online), at Toronto, Ontario, Canada.
- 3. "Anisotropic non-wetting metallic surfaces engineered via femtosecond laser micromachining," Md Abu Taher, Desai Narayana Rao, Sri Ram G Naraharisetty, National Laser Symposium (NLS-29), on 12-15th February 2021, at Shri Vaishnav Vidyapeeth Vishwavidyalaya, Indore, India.
- 4. "Super Black Stainless-Steel Surface Fabricated by Nanosecond Laser Irradiation," Md Abu Taher, D Narayana Rao, Sri Ram G Naraharisetty, Conference on Lasers and Electro-Optics (CLEO), 2020 (Online), at San Jose Convention Center, San Jose, California, USA.
- 5. "Ellipsoidal droplet on the anisotropic non-wetting copper surface," (Student Conference on Optics and Photonics) SCOP 2019, Md Abu Taher, D Narayana Rao, Sri Ram G Naraharisetty at Physical Research Laboratory, Ahmedabad, India.

# **Poster Presentations**

- 1. "Broadband super black stainless-steel surface fabricated by nanosecond laser irradiation," Md Abu Taher, Desai Narayana Rao, Sri Ram G Naraharisetty, National Laser Symposium (NLS-26), on 8-11th January 2020, at Vellore Institute of Technology (VIT), Chennai, India. BEST Poster award.
- "Ellipsoidal droplet on the anisotropic non-wetting copper surface," Md Abu Taher, Hitheswar Prasad, Navanith Krishnan PK, Narayana Rao Desai, Sri Ram G Naraharisetty, Student Conference on Optics and Photonics (SCOP), on 24-26<sup>th</sup> September 2019, at Physical Research Laboratory, Ahmedabad, India.
- 3. "Anisotropic superhydrophobicity on patterned copper surfaces," Md Abu Taher, Hitheswar Prasad, Navanith Krishnan PK, Narayana Rao Desai, Sri Ram G Naraharisetty, National Laser Symposium (NLS-27), on 3<sup>rd</sup> -6th December 2018, at Raja Ramanna Centre for Advanced Technology, Indore, India.
- 4. "Anti-reflection properties of metallic surface fabricated by pulsed laser irradiation," Md Abu Taher, Hitheswar Prasad, D Narayana Rao, Sri Ram G Naraharisetty, National Laser Symposium (NLS-26), on 20-23th December 2017, at Bhabha Atomic Research Center (BARC), Mumbai, India.
- 5. "Broadband antireflective surface is a reality with small scale structure," Md Abu Taher, Hitheswar Prasad, D. Narayana Rao, Sri Ram G Naraharisetty, National Conference on Physics at small scale and advanced materials, on 7-8<sup>th</sup> September 2017, at University of Hyderabad, Hyderabad, India.
- 6. Participated in workshop on "Advances in Optics and Photonics" and worked as an instructor on hands-on experience related to optics and photonics experiments, on 17<sup>th</sup>-23<sup>rd</sup> March 2019, at the School of Physics, UoH.
- 7. Attended FIP (Frontiers in Physics)-2016 at School of Physics, UoH, Hyderabad.

Ultrafast laser surface processing and its applications in the fabrication of dual-scaled grating structures, perfect absorbing, and non-wetting surfaces

by Md Abu Taher

**Submission date:** 15-Dec-2021 12:42PM (UTC+0530)

**Submission ID:** 1730970774

**File name:** Md Abu Taher.pdf (6.59M)

Word count: 25343 Character count: 132741

Librarian

Indira Gandhi Memorial Library
UNIVERSITY OF HYDERABAD
Central University P.O.

Ultrafast laser surface processing and its applications in the fabrication of dual-scaled grating structures, perfect absorbing, and non-wetting surfaces

**ORIGINALITY REPORT** 

64%

43%

62%

2%

SIMILARITY INDEX

INTERNET SOURCES

PUBLICATIONS

STUDENT PAPERS

**PRIMARY SOURCES** 

1

iopscience.iop.org

Internet Source

Publication

This is from Student publication

26%

Md Abu Taher, Nitin Chaudhary, K
Thirunaukkarasu, Vinod K Rajput, Sri Ram Good
Naraharisetty. "Controlled periodicities of
ladder-like structures via femtosecond laser
of wavelength from 400 nm to 2200 nm", MS
Surfaces and Interfaces, 2021

2

Md Abu Taher, Vinod Kumar Rajput, navanith Krishnan P K, Sri Ram Gopal Naraharisetty. "The validity of Triple Contact Line theory from hydrophilic to superhydrophobic surfaces", Journal of Physics D: Applied Physics, 2021

\_

, apricatio

Publication

Md Abu Taher, Vinod K Rajput, Navanith Krishnan P K, Sri Ram G Naraharisetty. "The validity of triple contact line theory from

4%

Ifem numbers 1,2,3,4,526 are from the Students Self publications

School of Physics,

# hydrophilic to superhydrophobic surfaces", Journal of Physics D: Applied Physics, 2021

Publication

5	Md Abu Taher, Hitheswar Prasad, P K Navanith Krishnan, Narayana Rao Desai, Sri Ram G Naraharisetty. "Ellipsoidal droplet formation on anisotropic superhydrophobic copper surface", Surface Topography: Metrology and Properties, 2019	2%
	Publication Dr. N. Assir	star professor, star professor, special physics, line of Hyderabad
6	Md Abu Taher, Sajin Ponnan, Hiteswar Prasad, Desai Narayana Rao, Sri Ram G Naraharisetty.  "Broadband absorption of nanostructured stainless steel surface fabricated by nanosecond laser irradiation",  Nanotechnology, 2020  Publication  Md Abu Taher, Sajin Ponnan, Hiteswar Prasad, desaid and desai	SRI RAM GOPAL stant Professor, hool of Physics, hool of Hyderabad derabad-500 046.
7	Submitted to University of Hyderabad, Hyderabad Student Paper	<1%
8	Submitted to University of Durham Student Paper	<1%
9	www.science.gov Internet Source  Hyderabad-500 046.	<1%
10	Submitted to Universiti Teknologi MARA Student Paper	<1%

www.ncbi.nlm.nih.gov

11	Internet Source	<1%
12	livrepository.liverpool.ac.uk Internet Source	<1%
13	Submitted to Colorado Technical University Online Student Paper	<1%
14	hdl.handle.net Internet Source	<1%
15	Kostić, S., Z.Ž. Lazarević, V. Radojević, A. Milutinović, M. Romčević, N.Ž. Romčević, and A. Valčić. "Study of structural and optical properties of YAG and Nd:YAG single crystals", Materials Research Bulletin, 2015.	<1%
16	Submitted to Universiti Teknologi Petronas Student Paper	<1%
17	Submitted to KTH - The Royal Institute of Technology  Student Paper	<1%
18	Submitted to Imperial College of Science, Technology and Medicine Student Paper	<1%
19	Submitted to Higher Education Commission Pakistan Student Paper	<1%

20	escholarship.org Internet Source	<1%
21	www.annualreviews.org Internet Source	<1%
22	Submitted to Austin Peay State Uniersity Student Paper	<1%

Exclude quotes On

Exclude matches

< 14 words

Exclude bibliography On



Dr. N. Sri Ram Gopal Assistant Professor School of Physics University of Hyderabad Central University P.O Hyderabad 500 046

Tel: +91-40-2313 4310 Fax: +91-40-2301 0227

e-mail:

srgopal234@gmail.com Mobile: 9492142693

> 15/12/2021, Hyderabad.

# To whom it may concern

This is to certify that the thesis entitled "Ultrafast laser surface processing and its applications in the fabrication of dual-scaled grating structures, perfect absorbing, and non-wetting surfaces" is submitted by Mr. Md Abu Taher (Registration ID: 15PHPH18) is based on his research work under my guidance. The thesis has been screened by Turnitin software at the library of the University of Hyderabad. The software shows the similarity index of 64%, out of which 62% comes from the following published first author papers of Mr. Md Abu Taher.

- (1) Surface Topography: Metrology and Properties, 7, 035001 (2019).
- (2) Nanotechnology, 31, 175301 (2020).
- (3) J. Phys. D: Appl. Phys. 55, 055305(2022)
- (4) Surfaces and Interfaces 28, 101622, 2022.

A thorough look at the report shows that the major part of the remaining 2% might have come from other articles and the use of some standard technical terms. Therefore, this thesis is free from plagiarism.

Yours sincerely

Dr. N Sri Ram Gopal

Dr. N. SRI RAM GOPAL Assistant Professor, School of Physics, University of Hyderabad Hyderabad-500 046.